EXTENDING ULTRASHORT-LASER-PULSE MEASUREMENT TECHNIQUES TO NEW DIMENSIONS, TIME SCALES, AND FREQUENCIES

A Dissertation
Presented to
The Academic Faculty

by

Selçuk Aktürk

In Partial Fulfillment
of the Requirements for the Degree
Doctor of Philosophy

School of Physics
Georgia Institute of Technology
March 2005

EXTENDING ULTRASHORT-LASER-PULSE MEASUREMENT TECHNIQUES TO NEW DIMENSIONS, TIME SCALES, AND FREQUENCIES

Approved by:

Dr. Rick Trebino, Advisor
School of Physics
Georgia Institute of Technology

Dr. Philip First
School of Physics
Georgia Institute of Technology

Dr. Ali Adibi
School of Electrical and Computer Engineering
Georgia Institute of Technology

Dr. John Buck
School of Electrical and Computer Engineering
Georgia Institute of Technology

Dr. Chandra Raman
School of Physics
Georgia Institute of Technology

Date Approved: 29 March 2005

Dedicated to my mother Hanife and my father Ali

ACKNOWLEDGEMENTS

I would like to express my countless thanks to all people who helped me in many ways throughout my graduate school years. First of all, I would like to thank to Rick for his constant motivation since the beginning, his great support and for always sharing his knowledge and experience, which made this thesis possible. Thanks to Mark for teaching me how to be an experimentalist and for sharing countless hours inside and outside of the lab. Thanks to Patrick for giving me the flag that I carried forward. Thanks to Erik for being the one that I ask first. Thanks to Xun, Aparna, Pablo, Xuan, Qiang, Dongjoo, Ziyang, Neeraj and all other members of the group for being such nice co-workers and friends all the time. Thanks to Bugra and Seyhmus for their company through many years. Thanks to Steve and Lee for invaluable friendship. And finally, special thanks to my family: my sisters Fatma, Ayse and Havva, my brother Ismail, my father Ali and my mother Hanife for their endless love.

TABLE OF CONTENTS

LIST OF TABLES

LIST OF FIGURES

SUMMARY

In the last decade, there has been tremendous progress in the field of ultrashort-pulse measurement. However, this effort has focused mostly on the temporal behavior of 100-fs, 800-nm ultrashort pulse, ignoring other pulse lengths, wavelengths, and the very common space-time couplings or so called spatio-temporal distortions. In this thesis work, I do an extensive study of spatio-temporal distortions and their measurement using Frequency Resolved Optical Gating (FROG) and its relatives. I clarify some ambiguities in the descriptions of these effects in the existing theory and establish a more general description of such distortions in ultrashort pulses. I also extend these measurement techniques to different wavelengths and pulse lengths. Specifically, I develop measurement devices for few-cycle NIR pulses, weak and narrowband fiber laser pulses, long (several-ps) NIR pulses, and visible pulses from NOPAs.

CHAPTER I

BACKGROUND AND INTRODUCTION

The field of ultrashort laser pulse measurement is based on a dilemma: "In order to measure an event in time, you need a shorter one. Then how can one measure the shortest event ever generated?"

Ultrashort laser pulses are the shortest events ever generated by human beings, wherein lies the challenge. They cannot be "photographed" by electronic detectors, which are several orders of magnitude slower. Since there is no shorter event available to measure ultrashort pulses, the shortest possible event that can be used is the pulse itself. This approach, combined with nonlinear optics yielded a measurement scheme called "intensity autocorrelation" [95, 51], and historically it is the first ever attempt to picture an ultrashort pulse. Ironically, this first attempt produced only a blurred image of an ultrashort pulse: autocorrelators yield only a rough estimate of pulse temporal width with no pulse shape or phase information. They have many non-trivial ambiguities and they are very sensitive to noise. Despite these facts, for about two decades, autocorrelators remained the best devices available to use for ultrashort laser scientists. Fortunately, the early 1990s witnessed tremendous improvements in the field of ultrashort pulse measurements and various schemes that fully characterize temporal behavior of ultrashort pulses had been presented. Without question, the most significant one of these schemes is Frequency-Resolved Optical Gating (FROG) [18, 21, 42, 87, 17, 91].

FROG was the first device ever developed to extract the pulse phase information, along with the pulse intensity information. This allowed one to obtain the full electric field of the pulse in the time and frequency domains. This ability of extracting phase helped ultrashort pulse researchers tremendously. In the pulse generation field, for example, for the first time, the researchers observed experimentally that second and higher order spectral phase causes the pulses to spread in time, yielding lower peak powers. By tracking down the elements of

the experimental apparatus, they were able to eliminate the higher order phase, and obtain much shorter pulses [45].

The next significant improvement in the pulse measurement field, which made the lives of ultrashort pulse researchers even easier, was the simplification of FROG. O'Shea et al. [65] showed that the setup of FROG can be greatly simplified using some clever ideas. These ideas simplified FROG setup to such an extend that the resulting device requires almost no alignment and yet gives the same information. This relative of FROG is named GRENOUILLE, standing for Grating Eliminated No-Nonsense Observation of Ultrafast Incident Laser Light E-fields. GRENOUILLE eliminated all of the alignment knobs of FROG and became the simplest ultrashort pulse measurement device.

Over a decade, FROG and GRENOUILLE (and alternative pulse measurement devices) have been used for many different applications. Various schemes have been proposed and tested. However, the applicable range of use of these devices have been very restricted. Although the pulse intensity and phase are (in principle) fully measured, this is done under certain approximations, which can (and do) easily fail to be true in most ultrafast laser laboratories.

First of all, these pulse measurement techniques focus on the temporal or spectral evolution of the pulse electric field, ignoring the spatial coordinates. This is based on assumption that the pulse temporal/spectral field evolves independent of spatial coordinates. Any kind of coupling between spatial coordinates and time/frequency is specifically suppressed. Unfortunately, couplings between space and time and/or frequency are very common in ultrashort laser pulses. In fact, generation and manipulation of these pulses requires introduction of massive amounts of such couplings, to be -in principle- removed afterwards. Their broadband nature makes ultrashort pulses particularly vulnerable to these effects. When they occur, the results of experiments conducted with ultrashort pulses can be limited ar even incorrect. These space and time/frequency couplings constitute the first subject matter of this thesis. I do an extensive study of these couplings or so-called "spatio-temporal distortions". I clarify some previously saddle definitions and propose a much more general model for ultrashort pulses. Furthermore, I demonstrate measurement and diagnostic

techniques for these distortions.

The pulse measurement devices can also work only in certain pulse width ranges. These devices focus on the most common scenario: measuring pulses that are about $100 - fs$ long. The devices are operable at around these pulse widths. Convenient pulse measurement techniques are still not available for extremely short and extremely long pulses. Such measurements are usually not done because of presence of particular, non-trivial challenges. Extreme group velocity dispersion and need for very high spectral resolution are just to name a few. The next part of this thesis is dedicated to extending ultrashort pulse measurement techniques to these new time scales. I propose and demonstrate solutions to several unsolved problems in extending pulse measurement to new time scales.

Another restriction that is present in pulse measurement techniques is the applicable laser wavelength. Most pulse measurement devices are developed for measuring pulses emitted by Ti:Saphire lasers, which emit pulses with their spectra centered at around 800 nm. This is done so, again, since this is the most common case; Ti:Sapphire lasers are the workhorses for ultrafast optics. Not surprisingly, many applications require sources at other wavelengths, too. For this reason, ultrashort pulse generation scientists are always in search for novel laser sources. Several schemes are already available today for ultrashort pulse generation at various wavelengths. This is achieved in mainly two different ways: By using and amplified Ti:Sapphire system to pump an optical parametric amplifier/oscillator (OPA/OPO) [13, 68], or by using a different laser media in a complete laser to lase at desired wavelength [60, 77]. Using an OPA/OPO also provides a great tunability, preserving ultrashort pulse lengths. Lasers with novel lasing media, on the other hand have much simpler setups. As expected, these sources at novel wavelengths require novel pulse measurement devices (or extension of currently available techniques). All optical systems have frequency dependence, so a measurement device built to work at one wavelength will not work at another. Often times, because of this dependence, extending the measurement techniques to new wavelengths can be challenging (or even impossible). In the last few chapters of this thesis, I present several methods for extending pulse measurement techniques to new frequencies.

Throughout this document, as ultrashort pulse measurement tools, I will focus on FROG and its relatives (especially GRENOUILLE). Other techniques are mentioned whenever required or comparisons needed. Because of its historical significance and since FROG is based on it, I will start with a brief discussion of intensity autocorrelation. It will be followed by a summary of FROG and GRENOUILLE.

1.1 Autocorrelation

Historically, the intensity autocorrelation (we will abbreviate this as autocorrelation, whenever there is no possible confusion with field autocorrelation) is the first attempt ever to measure an ultrashort pulse's electric field [95, 51]. Figure 1 shows a basic setup of an autocorrelator. The pulse to be measured is split into two equal parts with a beam-splitter. One arms goes through a variable delay (translation stage). The two pulses are then recombined in a nonlinear crystal. Most often, for sensitivity reasons, the crystal is chosen to be appropriate for second-harmonic generation (SHG) [13]. In the nonlinear crystal, the input pulse and its replica contribute to the nonlinear polarization. As a result of these two pulse fields, a nonlinear signal is generated, apart from the nonlinear fields generated by each of the two input fields. The key point here is that, the nonlinear signal, which is generated by mixing of the two fundamental fields, will exist only when two pulses overlap in time. Moreover, the intensity of the signal also depends on the temporal overlap of them. By scanning the delay and recording the signal intensity at the slow detector, one obtains a function (of delay) that is the intensity autocorrelation. It is very intuitive that autocorrelation yields some measure of the input pulse width.

Now the question is: "How much information can we retrieve from an autocorrelation?". The nonlinear signal intensity, as read by the detector will be given by [87]:

$$A^{(2)}(\tau) = \int_{-\infty}^{\infty} I(t)I(t-\tau)\,dt \tag{1}$$

where $I(t)$ is the pulse intensity. The width of the autocorrelation is related to the input pulse width. For pulses that do not have too much temporal structure, a pulse shape can be assumed, and for that particular shape, the pulse width can be related to the autocorrelation width [22, 74].

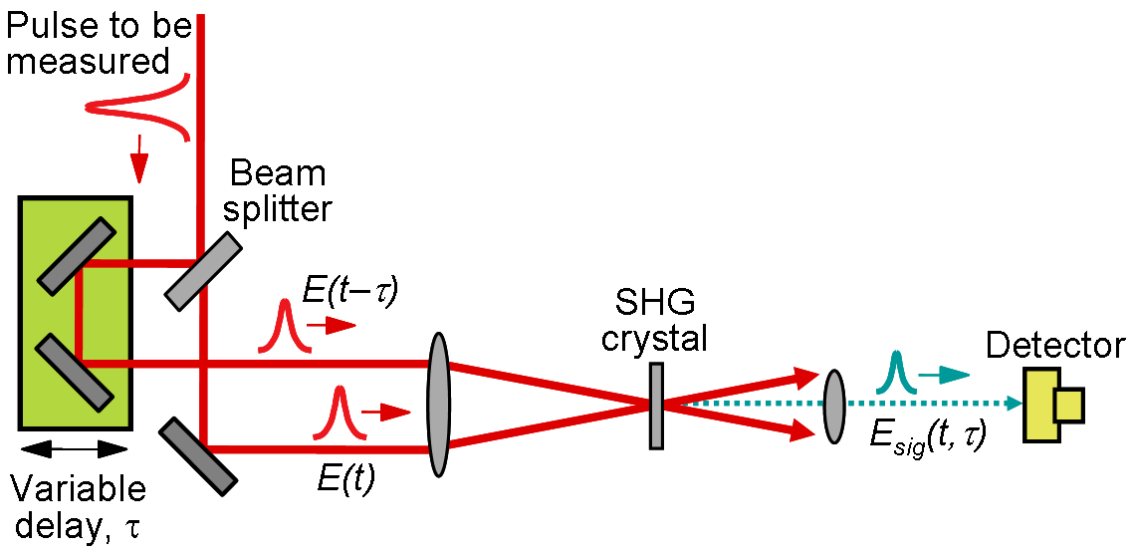

Figure 1: A classical Autocorrelator.

Applying autocorrelation theorem to equation 1, we can see that Fourier transform of the autocorrelation yields the magnitude square of the Fourier transform of the intensity. This automatically shows that in an autocorrelation measurement, pulse phase information is lost! Moreover, $A^{(2)}(\tau)$ is always symmetric with respect to delay. Pulses with quite different temporal intensity profiles can have the same exact autocorrelation [87]. More ambiguities arise when the input pulse has a complicated intensity profile. As a result, autocorrelators are far from uniquely determining a pulse's intensity and phase.

Attempts have been made to use autocorrelation together with a spectrum, to retrieve the pulse phase. Unfortunately, these methods also have some nontrivial ambiguities. Worse, these two measurements provide 2N data points in an attempt to retrieve 2N variables (N intensity and N phase), with no additional constraint. This makes the method severely vulnerable to noise.

Nevertheless, autocorrelators give a rough estimate of the pulse width and it may be satisfactory for quick evaluations. If the application requires only an approximate pulse width value, then an autocorrelator is sufficient. However, with the broad range of applications of ultrashort pulses, spanning multiple fields including Chemistry and Biology, to be able to make real use of ultrashort laser pulses, the pulse phase information cannot be disregarded.

1.2 FROG

Simply imaging the nonlinear signal to the entrance slit of a spectrometer turns an autocorrelator into a FROG [42, 18, 87, 86]. Instead of recording the signal intensity for each delay, one has to record spectrum of the nonlinear signal for each delay. Therefore, the output of FROG is a two-dimensional image (referred to as FROG trace), which has delay on one axis and wavelength on the other (see Figure 2).

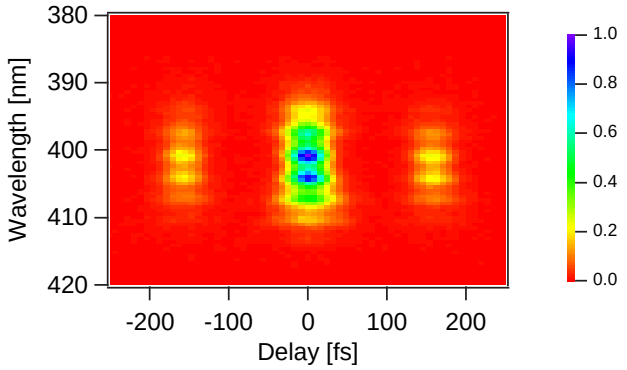

Figure 2: An experimental FROG trace

As opposed to an autocorrelator, in a FROG setup, the slow detector is placed at the output of the spectrometer. Therefore, the detector does not read the square of the signal field, but it records the square of the Fourier transform of signal electric field. Hence, the mathematical expression for FROG traces is:

$$I_{\mathrm{FROG}}(\omega,\tau) = \left| \int_{-\infty}^{\infty} E_{sig}(t,\tau)\exp(-i\omega t)\mathrm{d}t \right|^2 \tag{2}$$

where $E_{sig}(t,\tau)$ is the signal electric field, the explicit expression of which depends on the nonlinearity used. For second harmonic generation (SHG), for example:

$$E_{sig}(t,\tau) = E(t)E(t-\tau) \tag{3}$$

By a quick observation of FROG trace expression, as in equation 2, one can see that the pulse phase information is not lost! It is rather "signatured" in the FROG trace. This is the most important distinction of FROG from an autocorrelator.

Remember that autocorrelation was a one-dimensional plot, providing 2N data points (with an additional spectrum measurement) in an attempt to retrieve N intensity and N phase points. As we have seen in section 1.1, this is not only ambiguous, but also very sensitive to noise. On the other hand, a FROG trace has $N \times N$ data points, essentially over-determining the pulse electric field [101, 94].

As equation 2 clearly shows the dependence of the trace on pulse phase, pulse phase information is not lost in a FROG measurement . However, it cannot be directly solved for, either. This means that, we cannot use an analytical expression to directly extract the phase from the FROG trace. Instead, an iterative algorithm needs to be used. Fortunately, the two constraints, the nonlinearity and FROG trace data, are sufficient to uniquely determine the pulse intensity and phase.

The conventional FROG algorithm is called "generalized projections" [19]. This algorithm starts with an initial guess. Given the nonlinearity used in the experiment, it generates the nonlinear signal for the initial guess (a function of time and delay). Then, the Fourier transform of this signal field is taken (a function of frequency and delay). At this point, the data constraint is used: The magnitude of the Fourier transform is replaced with the magnitude from the experimental trace. Then the resultant field is inverse Fourier transformed, to complete one loop of the algorithm. After several iterations, the field converges to the real answer. With the retrieved field variables, usually another trace is reconstructed (to be referred in this document as "retrieved trace"). The difference between the original and retrieved traces gives what is called "FROG error", a criteria of the quality of the measurement. FROG algorithm is shown to converge even for very complicated pulse shapes [34, 35]. With the recent improvements on the algorithm, the retrieval can update approximately 20 traces per second (for not too complicated pulses), which essentially operates real time [41], yielding an "ultrafast oscilloscope".

1.3 Single-shot FROG

In order to acquire a FROG trace, we need to get signal spectrum for each delay. Also, in order to observe the nonlinear signal generated by the pulse and its replica, they need

to overlap both in time and in space, and they should stay overlapped during the scan of the delay. Moreover, the overlap should happen in a relatively tight focus, to increase conversion efficiency. These are the most important factors that makes the setup of FROG difficult to align. Furthermore, the multi-shot behavior of the setup also requires long term stable lasers. If the pulses change shot to shot, then the multi-shot FROG trace will be an averaged data. This may not be desirable at all times.

Even when the pulse output is stable, not all of the ultrashort lasers have a high repetition rate. Many ultra-high-power ultrafast laser systems has to operate at very low repetition rates. Acquiring a FROG trace for such a laser will require an inconveniently and unpractically long time.

These issues requires a solution that allows us to measure single pulses. One approach to the solution to this problem is "single-shot autocorrelation" [87], which can also be applied to FROG to develop a "single-shot FROG" [43, 20]. Single-shot FROG (or autocorrelation) utilizes the fact that crossing two beams at an angle in space automatically maps delay onto transverse position. This is illustrated in Figure 3. Due to crossing at an angle, the two pulses arrives at different times with respect to each other, along the transverse dimension.

This geometry brings several simplifications to FROG's setup. First of all, scanning the delay (with a translation stage) is no longer necessary. Secondly, single-shot FROG requires focusing to a line (with cylindrical optics) rather than to a spot, the line focus being in the transverse delay direction. Aligning two beams at a line focus is much easier than doing so at a point focus. Data acquisition is also much easier in single-shot FROG. One can directly map the nonlinear signal to the entrance slit of an imaging spectrometer, in such a way that delay is in the direction of the slit. Then, at the output slot of the spectrometer, a CCD can be used to directly capture the FROG trace.

In short, this single-shot geometry of FROG has many advantages over the traditional multi-shot geometry. It allows measuring single pulse (as long as the pulse energy is enough). It is also experimentally much simpler. The compromise in single-shot FROG is the sensitivity. Since the beams are crossed to a line, rather than a point, the intensity at focus is lower. Therefore, the nonlinear conversion efficiency is also lower, reducing the sensitivity

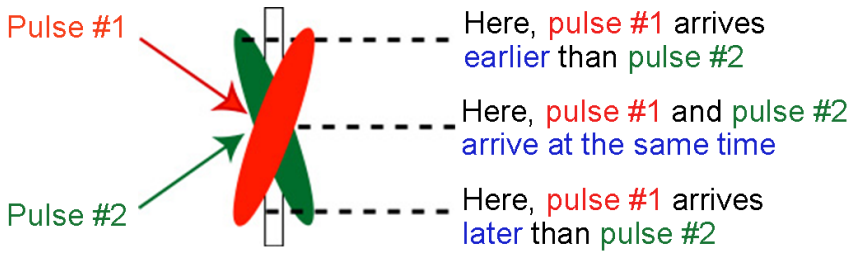

Figure 3: Crossing two beams at an angle maps delay onto position.

(weakest measurable pulse energy) of the device.

Single-shot FROG also requires a fairly clean spatial profile laser beam. Since the delay is mapped to transverse position, if there is any transverse intensity variation, this will cause and additional weighting on the second harmonic signal, biasing the experiment (note that this is not a problem in multi-shot FROG). This, usually is not a big issue, however, since most ultrafast sources emit light close to TEM_{00} spatial mode. The Gaussian spatial profile of these lasers may also cause extra weighting, and this can be avoided by expanding the beam and making the measurement over the flat region of the beam. Alternatively, if desired, this effect can also be taken into account in the post processing. Finally, spatial filtering techniques [12] can also be used if the spatial mode of the beam is not sufficiently uniform.

1.4 GRENOUILLE

Single-shot FROG is a very robust and reliable measurement technique, and compared to multi-shot FROG, its setup is simple. However, it still requires considerable alignment effort, and the apparatus takes up a relatively large space. However, O'Shea et.al. showed that it is possible to build a single-shot SHG FROG device for measuring ultrashort laser pulses that consists entirely of only four or five optical elements, and it is so simple that, once set up, it never requires realignment. This variation of FROG is called GRENOUILLE (GRating-Eliminated No-nonsense Observation of Ultrafast Laser-Light E-Fields) [65], and it is the simplest ultrashort pulse, intensity and phase measurement device to date.

GRENOUILLE involves two innovations. First, a Fresnel biprism replaces the beam

splitter and delay line in a FROG. Second, a thick crystal replaces the thin crystal and spectrometer in a FROG, yielding a very simple device. Specifically, when a Fresnel biprism (a prism with an apex angle close to 180 degrees) is illuminated with a wide beam, it spatially splits the beam into two beamlets and crosses these beamlets at an angle as in conventional single-shot FROG beam geometry, in which the relative beam delay is mapped onto horizontal position at the crystal (See Figure 4). But, better than conventional single-shot geometries, the beams here are automatically aligned in space and in time by the Fresnel biprism, a significant simplification. Then, as in standard single-shot geometries, the signal at the output face of the crystal is imaged onto a CCD camera, where the signal is detected vs. position (i.e., delay) in the horizontal direction.

FROG also involves spectrally resolving the pulse after it has been time-gated by itself. GRENOUILLE (See Figure 4) combines both of these operations in a single thick SHG crystal. As usual, the SHG crystal performs the self-gating process: the two pulses cross in the crystal with variable delay. But, in addition, the thick crystal has a very small phase-matching bandwidth, so the phase-matched wavelength produced by it varies with angle. Thus, when the beam is tightly focused cylindrically, the beam will be incident on the crystal with range of angles. Due to narrow phase-matching bandwidth of the crystal, only a very narrowband portion of the pulse will phasematch at a particular angle. However, overall, the entire pulse spectrum will be phase matched, in such a manner that the second harmonic frequency is mapped to angle. And this was precisely the purpose of using a spectrometer in FROG, i.e. the thick crystal also acts as a spectrometer.

The first cylindrical lens must focus the beam into the thick crystal tightly enough to yield a range of crystal incidence (and hence exit) angles that is large enough to include the entire spectrum of the pulse. After the crystal, a cylindrical lens then maps the crystal exit angle onto position at the camera, with wavelength a near-linear function of (vertical) position. The resulting signal at the camera is a single-shot SHG FROG trace with delay running horizontally and wavelength running vertically.

The standard FROG retrieval algorithm can be run on the output of GRENOUILLE without need of an alteration. The whole setup of GRENOUILLE is very compact and very

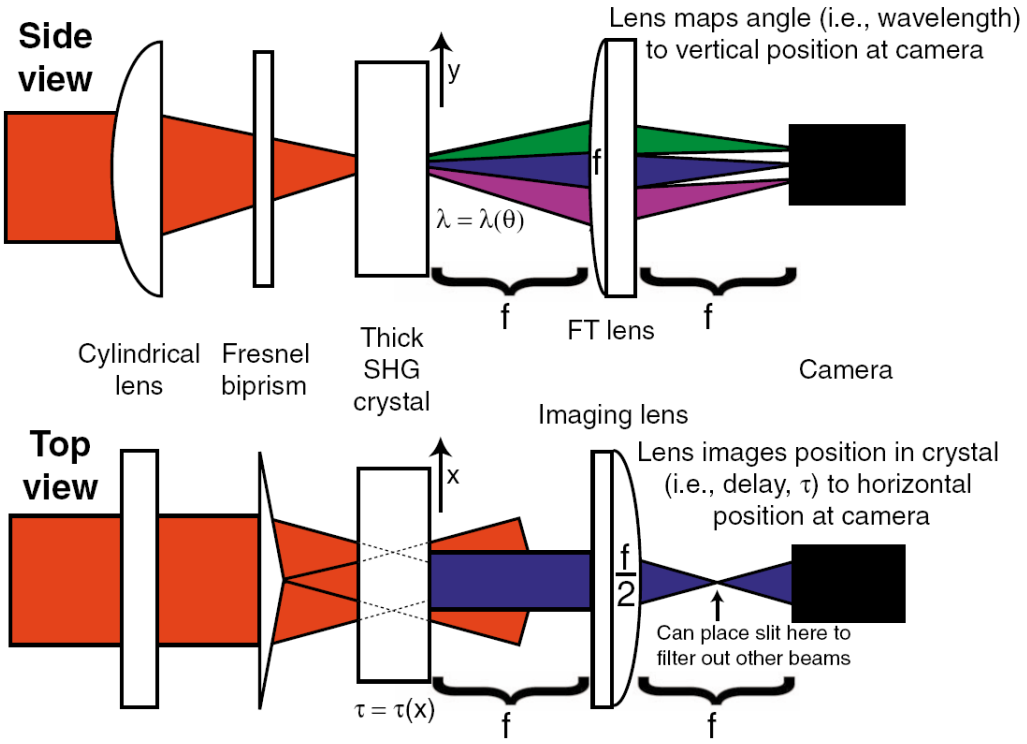

Figure 4: Top and side view of GRENOUILLE.

easy to align. And it can be used to measure intensity and phase of even fairly complicated pulses.

Although its setup is very simple, the design of GRENOUILLE requires significant effort and theoretical/experimental study [63]. One of the key issues in GRENOUILLE is the crystal thickness. In almost all pulse measurement devices that includes nonlinear optics, the phasematching bandwidth of the nonlinear crystal used must be larger than the pulse bandwidth, in order to avoid weighting on the signal due to conversion efficiency. Ordinarily, achieving sufficient phase-matching bandwidth is equivalent to minimizing the group-velocity mismatch, GVM: the fundamental and the second harmonic pulses must overlap in the entire SHG crystal length, L. This condition can be written as: $\mathrm{GVM} \times \mathrm{L} \ll \tau_\mathrm{p}$, where τ_p is the pulse length, $\mathrm{GVM} \equiv \frac{1}{\mathrm{v_g}(\lambda_0/2)} - \frac{1}{\mathrm{v_g}(\lambda_0)}$, $\mathrm{v_g}(\lambda)$ is the group velocity at wavelength λ, and λ_0 is the fundamental wavelength. For GRENOUILLE, however, the opposite condition is necessary; the group velocity mismatch times the crystal length must be much larger than pulse length (equivalent to the condition that phase matching

bandwidth of the crystal is much smaller than the pulse bandwidth):

$$\mathrm{GVM} \times \mathrm{L} \gg \tau_{\mathrm{p}} \tag{4}$$

which ensures that the fundamental and the second harmonic cease to overlap well before exiting the crystal, for it to act as a frequency filter.

On the other hand, as every pulse measurement technique requires, the crystal must still not be too thick, or group-velocity dispersion (GVD) will cause the pulse to spread in time and become distorted:

$$\mathrm{GVD} \times \mathrm{L} \ll \tau_{\mathrm{c}} \tag{5}$$

where $\mathrm{GVD} \equiv \frac{1}{\mathrm{v_g}(\lambda_0 - \delta\lambda/2)} - \frac{1}{\mathrm{v_g}(\lambda_0 + \delta\lambda/2)}$, $\delta\lambda$ is the pulse bandwidth, and τ_c is the pulse coherence time ($\sim$ the reciprocal bandwidth, $1/\Delta\nu$), a measure of the smallest temporal feature of the pulse. Since $GVD < GVM$, this condition is ordinarily already satisfied in conventional FROG by the usual GVM condition. However, in GRENOUILLE, the GVD condition is opposite and must be considered separately. Combining these two constraints, we have:

$$\mathrm{GVD} \times (\tau_{\mathrm{p}}/\tau_{\mathrm{c}}) \ll \tau_{\mathrm{p}}/\mathrm{L} \ll \mathrm{GVM} \tag{6}$$

Therefore, there exists a crystal length L that satisfies these conditions simultaneously if:

$$\mathrm{GVM}/\mathrm{GVD} \gg \mathrm{TBP} \tag{7}$$

where we have taken advantage of the fact that τ_p/τ_c is the time-bandwidth product (TBP) of the pulse. Equation (7) is the fundamental equation of GRENOUILLE and it will be used as a starting point whenever the device is going to be extended to a different pulse regime.

Equation 7 also dictates that, a GRENOUILLE device can only be designed to operate in a range of pulse widths (or bandwidth). Therefore, it is of great practical use to display the range in which a certain GRENOUILLE design can be used. This can be done easily since GVD and GVM can be computed given the Sellmeier formula for a crystal. After doing so, we can incorporate equations 6 and 7 in one plot over a desired range of pulse center wavelengths. Figure 5 shows such a plot: The graph shows upper bandwidth limit

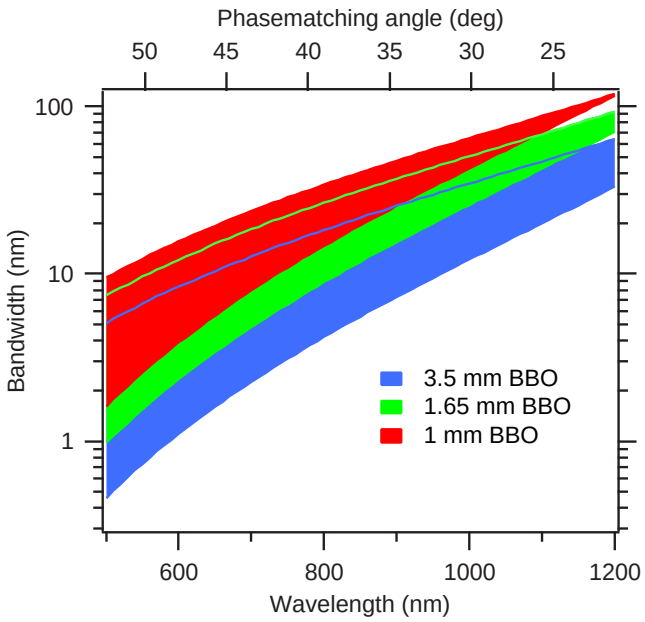

Figure 5: Applicable range of GRENOUILLE with different crystal lengths.

(set by GVD) and lower bandwidth limit (set by GVM) of a GRENOUILLE device, with different crystals thicknesses. GRENOUILLE can operate in the shaded regions, only. If the input pulse has more bandwidth than the upper line, than the input pulse will be distorted by GVD in the crystal. If the input pulse has its bandwidth less than the lower line, the spectral resolution of the crystal will not be sufficient to resolve the pulse spectrum. Similar plots can also be made in pulse width, instead of bandwidth [63].

CHAPTER II

PARAMETERIZATION AND MEASUREMENT OF SPATIAL CHIRP IN ULTRASHORT PULSES

This chapter originally appeared as two papers:

Xun Gu, Selcuk Akturk and Rick Trebino, "Spatial chirp in ultrafast optics", Optics Communications 242, 599-604 (2004) [33]

and

Selcuk Akturk, Mark Kimmel, Patrick O'Shea, Rick Trebino, "Measuring spatial chirp in ultrashort pulses using single-shot Frequency Resolved Optical Gating", Optics Express 11, 68-78 (2003) [5]

2.1 Spatio-temporal distortions

The space and time dependencies of an ultrashort pulse's electric field are often assumed to be separable into independent functions. This assumption fails when coupling occurs between the pulse electric field's space and time dependencies, and this is referred to as a spatio-temporal distortion. Such distortions are common in ultrafast optics because the generation, amplification, and manipulation of ultrashort pulses all involve the deliberate introduction and (it is hoped) subsequent removal of massive spatio-temporal distortions [22]. While it is generally desired that the resulting pulse be free of such distortions, improper alignment is common, and as a result, ultrashort pulses are often contaminated with spatio-temporal distortions. Indeed, the broadband nature of ultrashort pulses makes them particularly vulnerable to these distortions. When such pulses are utilized in applications, these distortions often erode temporal resolution, reduce intensity, and cause a wide range of other problems.

The most common such distortion is angular dispersion, which is usually deliberately caused by the use of a dispersive element such as a prism or grating. Angular dispersion is

useful because it yields negative group-velocity dispersion (GVD) [57, 31, 27], as opposed to positive GVD introduced by normal dispersive materials. The propagation of ultrashort pulses through glasses (lenses etc.) is usually unavoidable and this causes the pulse's frequency components to spread in time (referred to as "chirping"), stretching the pulse length. Due to negative GVD provided by angular dispersion, inverted prism and/or grating pairs cancel GVD introduced by materials and act as pulse compressors. Same geometry can also be used as a pulse stretcher, when stretching is needed instead of compression, as in the case of chirped pulse amplification [45].

In a prism/grating pair, after the second prism or grating, angular dispersion is usually zero, but another spatio-temporal distortion remains -spatial chirp- in which the pulse center frequency varies transversely across the beam. Propagation through another inverted pair of prisms or gratings, placed as mirror image of the first, removes the spatial chirp too, and in theory, both the resulting angular dispersion and spatial chirp are then zero. Unfortunately, these devices (and most other devices involving such elements) have strict alignment requirements, and, as a result, some residual angular dispersion and/or spatial chirp often remain in the output pulse. Worse, even when it is small, residual angular dispersion causes the spatial chirp to increase by mere propagation.

2.2 Spatial chirp in ultrafast optics

A beam with "spatial chirp" has its different frequency components separated in space transverse to the propagation direction. It is a very common and often undesirable spatio-temporal distortion in ultrafast optics and can be introduced by many routine operations in ultrafast laser labs. For example, a beam passing through an element with angular dispersion, such as a prism or a grating, experiences angular dispersion, causing different frequency components to propagate at different k-vectors. Immediately after propagation, the frequency components naturally separate in space, resulting in spatial chirp. A second prism or grating, aligned anti-parallel to generate negative group-delay dispersion [57], removes the angular dispersion, but significant spatial chirp remains (See Figure 6). Although using the prism/grating pair in a double-pass arrangement can

eliminate spatial chirp in the output beam, small and almost inevitable misalignments often allow some residual spatial chirp to remain in the beam. Other common practices in a lab, such as propagating beam through a tilted substrate (See Figure 6), also introduce spatial chirp.

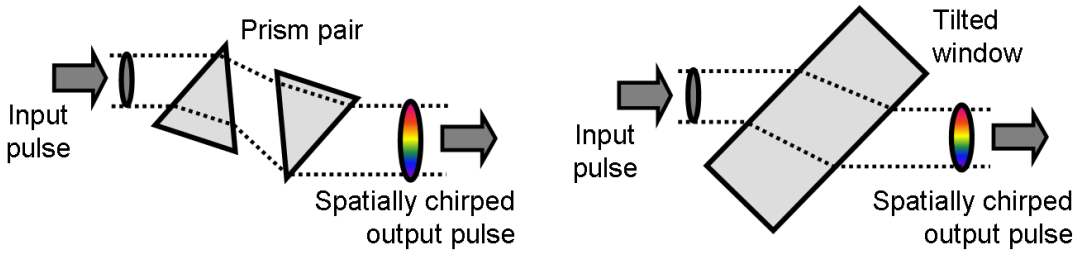

Figure 6: Generation of spatial chirp in a prism pair (left), tilted substrate (right)

On other occasions, researchers deliberately separate different frequency components spatially, such as in Fourier-synthesis pulse shaping [39, 98]. In this technique, a lens (or curved mirror) is placed one focal length away from a grating (or prism) in a telecentric configuration, mapping frequency to position, that is, introducing spatial chirp, at its focal plane (See Figure 7). At this point, a "phase modulator" (can be a deformable mirror, acusto-optic modulator, liquid crystal modulator etc.) sets a desired delay between the frequency components, essentially "shaping" the spectral phase of the pulse, which in turn will result in the desired temporal pulse shape. Obviously, the accuracy of pulse shaping depends on the degree of spatial chirp at the focal plane, on which extensive studies have been carried out [98, 97, 96]. Other applications of spatial chirp include the suppression of longitudinal mode competition [15, 58] in the laser design.

The twenty-first century has seen intensified interest in the spatio-temporal analysis of ultrashort-pulse beams. Numerous methods have been proposed to measure spatio-temporal characteristics of an ultrafast laser beam [75, 25, 24, 30, 84, 5, 4, 70]. To study these spatio-temporal effects, clear and unambiguous definitions of the various coupling parameters are undoubtedly required. Particularly, discussions on spatial chirp, one of the most common spatio-temporal coupling effects, have in the past been mostly confined to specific devices

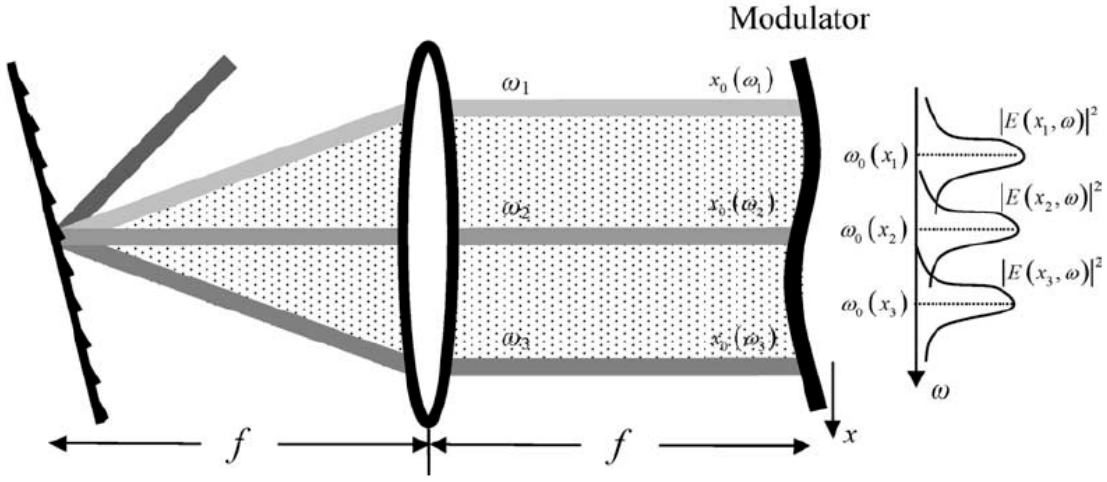

Figure 7: f-f Fourier-synthesis pulse shaper

[97, 96, 58, 53, 54, 85, 26, 62], and its definition has been somewhat arbitrary and vague in the literature. In this chapter, we attempt to clarify the meaning of this term. Specifically, we show that there are two different definitions of spatial chirp, which we refer to as "spatial dispersion" and "frequency gradient." Which definition to use depends on the situation. For Gaussian beams and pulses, we find the relationship between these two parameters to be analogous to that between the parameters describing temporal chirp in the time and frequency domains.

We begin with the case where no spatial chirp is present, and the amplitude of the electric field at position x and frequency ω (defined as frequency offset from the center frequency of the beam) can be written in the form:

$$E(x,\omega) = E_x(x)\, E_\omega(\omega) \tag{8}$$

where the spatial amplitude $E_x(x)$ and the spectral amplitude $E_\omega(\omega)$ are completely separate functions.

An equivalent representation of a general spatio-temporal ultrashort-pulse beam is the space-time Wigner function [67], which is defined as:

$$W^{\mathrm{ST}}(x,\xi,t,\omega) = \frac{1}{(2\pi)^2}\int\int E\left(x+\frac{x'}{2},\omega+\frac{\omega'}{2}\right)E^*\left(x-\frac{x'}{2},\omega-\frac{\omega'}{2}\right)\mathrm{e}^{[-\mathrm{i}(\xi x'+\omega' t)]}\mathrm{d}x'\mathrm{d}\omega' \tag{9}$$

The space-time Wigner function is a four-dimensional real-valued distribution function, which carries the same information about the ultrashort-pulse beam as the complex spatio-temporal (or spectral) field expression. The various two-dimensional marginals of the space-time Wigner function are the expressions of pulse-beam intensity in these domains. The space-time Wigner function is quite a powerful tool in the study of ultrafast beams, as an individual optical element can be described by a 4×4 matrix (to the first order in variations), and Wigner functions after these elements can be easily transformed with these matrices. This is especially powerful when propagation through many elements is to be modelled. However, in our analysis, we choose not to use them, because this work only involves studying the beam intensity in space and frequency. For that purpose, the simpler spatio-spectral field expression is a more appropriate tool.

In the presence of spatial chirp (here we assume that it exists in one transverse spatial dimension x only, generalization to include y direction is trivial), $E(x, \omega)$ becomes an inseparable two-variable function, where the spatial and spectral dependences are coupled. We can easily measure the spatio-spectral intensity profile of the spatially chirped beam by sending the beam into an imaging spectrometer with a two-dimensional detector (e.g. a CCD camera) on its output image plane, as depicted in Figure 8. Fields sampled at different points along the entrance slit of the spectrometer are spectrally resolved onto different rows of the camera image, resulting in a trace of intensity in the ω domain. With linear spatial chirp, the center frequency will vary across the slit, as a result the spatio-spectral intensity profile will appear tilted. Figure 9 shows a typical intensity plot of an experimental beam with spatial chirp.

Obviously, the degree of spatial chirp can be characterized by measuring the tilt of the $x-\omega$ trace. However, there is a subtlety in this measurement, namely, that there are two intuitive, but different, ways of measuring the tilt of the trace in the $x-\omega$ plane. The first involves measuring the center frequency, ω_0 , of each spatial slice, which yields a function $\omega_0(x)$. The slope of the $\omega_0(x)$ function, $\upsilon \equiv \frac{\mathrm{d}\omega_0}{\mathrm{d}x}$ is a natural measure of spatial chirp, which we will call the frequency gradient. The other means of parameterization involves measuring the beam center position, x_0, of each frequency component, which yields the

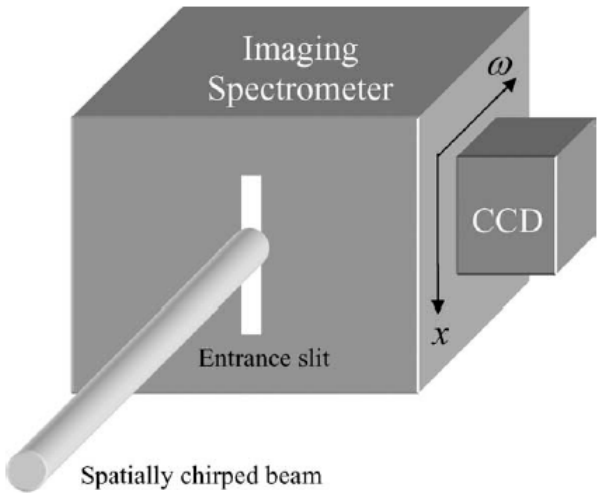

Figure 8: Measuring spatial chirp using an imaging spectrometer.

function, $x_0(\omega)$. Its slope $\zeta \equiv \frac{\mathrm{d}x_0}{\mathrm{d}\omega}$ is also a valid measure of spatial chirp, which we will call the spatial dispersion. Both parameters characterize the spatial chirp, and very importantly, they are not trivial reciprocals of one another.

In Figure 9, the blue line indicates the $\omega_0(x)$ function, which determines frequency gradient, and the black line the $x_0(\omega)$ function, which determines spatial dispersion. As clearly seen from the figure, the blue and black lines do not overlap, indicating that frequency gradient and spatial dispersion are not reciprocals of each other. In the absence of spatial chirp, both parameters are zero.

A few researchers have been aware of this subtlety of spatial chirp parameterization. Ohmae et al. have noted the difference between the $\omega_0(x)$ and $x_0(\omega)$ curves in their analysis of a Martinez-type multi-pass pulse stretcher, and their particular ray-tracing calculation yields the $x_0(\omega)$ result [62]. However, there has been no previous work published on the general relationship between the two spatial chirp parameters, which is necessary background for the increasingly important research on spatio-temporal distortions. We will devote the rest of the paper to this issue and will draw an analogy between spatial chirp and temporal chirp at the end, which we believe will shed new light on their physical implications.

First, we would like to point out that in most cases spatial chirp is introduced through angular dispersion; therefore, spatial dispersion is often the more fundamental of the two

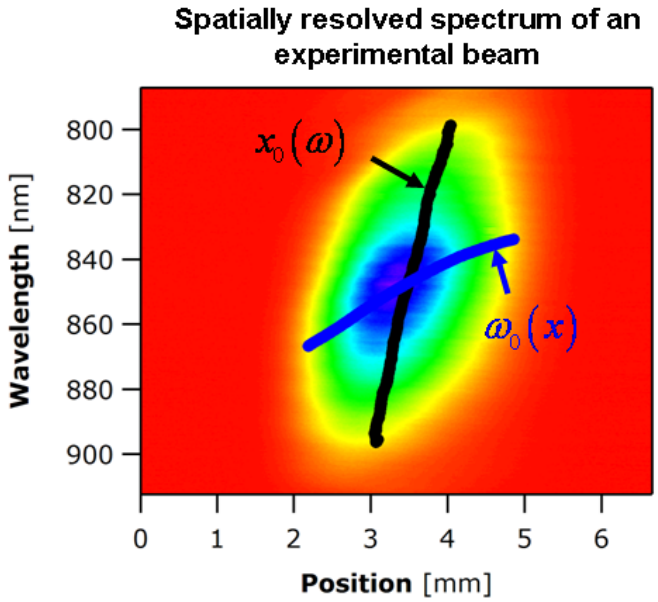

Figure 9: Experimentally measured spatio-spectral intensity profile of a spatially chirped beam.

definitions. When a beam with angular dispersion $\beta = \frac{\mathrm{d}\theta_0}{\mathrm{d}\omega}$ propagates through a distance L, the induced change in spatial dispersion is:

$$\Delta\zeta = L\beta \tag{10}$$

which is completely determined by the optical system only. Frequency gradient, on the other hand, is affected indirectly. As can be seen later, the change of the frequency gradient depends not only on the optical system, but on the parameters of the input beam and pulse as well. It is in this sense that spatial dispersion is a more fundamental parameter of spatial chirp in its generation, manipulation and removal, although frequency gradient is often more useful in the intended application of spatial chirp. In short, both quantities are important.

The relationship between frequency gradient and spatial dispersion is in general complicated, in that it depends on the spatial mode profiles of all the constituent frequency components, and the shape of spectrum. A common assumption is to assign all the frequency components the same spatial mode profile, which we will write as $E_x(x)$. We will also write the complex spectral amplitude of the beam as $E_\omega(\omega)$. Then the field expression

at position x and frequency ω in the beam can be written in terms of spatial dispersion ζ as:

$$E(x,\omega) = E_\omega(\omega)\, E_x(x - \zeta\omega) \tag{11}$$

We will focus on the simplest possible case, which is a Gaussian spectrum and a Gaussian spatial profile for all the frequency components. Namely,

$$E_\omega(\omega) = \exp\left[-\left(\frac{\omega}{\Delta\omega}\right)^2\right], \quad E_x(x) = \exp\left[-\left(\frac{x}{\Delta x}\right)^2\right] \tag{12}$$

where $\Delta\omega$ is the frequency bandwidth of the beam (1/e amplitude half width) and Δx is the beam width of a particular frequency component.

The spatio-spectral field amplitude for a pulse with spatial dispersion is then

$$E(x,\omega) = E_0 \exp\left[-\left(\frac{\omega}{\Delta\omega}\right)^2\right] \exp\left[-\left(\frac{x-\zeta\omega}{\Delta x}\right)^2\right] \tag{13}$$

We may reorganize the two exponential functions, and write the field in terms of frequency gradient υ . The expression becomes

$$E(x,\omega) = E_0 \exp\left[-\left(\frac{x}{\Delta x'}\right)^2\right] \exp\left[-\left(\frac{\omega-\upsilon x}{\Delta\omega'}\right)^2\right] \tag{14}$$

where

$$\upsilon = \frac{\zeta}{\zeta^2 + \left(\frac{\Delta x}{\Delta\omega}\right)^2} \tag{15}$$

is the frequency gradient;

$$\Delta\omega' = \left[\frac{1}{(\Delta\omega)^2} + \frac{\zeta^2}{(\Delta x)^2}\right]^{-\frac{1}{2}} \tag{16}$$

is the locally reduced frequency bandwidth due to spatial chirp, available at any particular locations in the beam;

$$\Delta x' = \left[\frac{1}{(\Delta x)^2} - \left(\frac{\upsilon}{\Delta\omega}\right)^2\right]^{-\frac{1}{2}} \tag{17}$$

is the increased overall beam width due to spatial chirp.

Equation 15 describes the relationship between the frequency gradient υ and the spatial dispersion ζ . Note that they are not reciprocals of each other. In fact, they are asymptotically reciprocals only when spatial dispersion $\zeta \equiv \frac{\mathrm{d}x_0}{\mathrm{d}\omega}$ is much larger than $\frac{\Delta x}{\Delta\omega}$. If spatial dispersion ζ is very small, on the other extreme, the two parameters are

actually proportional. For a given beam width Δx and frequency bandwidth $\Delta\omega$, frequency gradient υ reaches its maximum achievable value $\frac{1}{2}\left(\frac{\Delta\omega}{\Delta x}\right)$ when $\zeta \equiv \frac{\mathrm{d}x_0}{\mathrm{d}\omega} = \frac{\Delta x}{\Delta\omega}$. Figure 10 shows the relationship of frequency gradient and spatial chirp with $\Delta x = 1.0$mm and $\Delta\omega = 0.094$rad/fs, the conditions for the experimental trace in Figure 9.

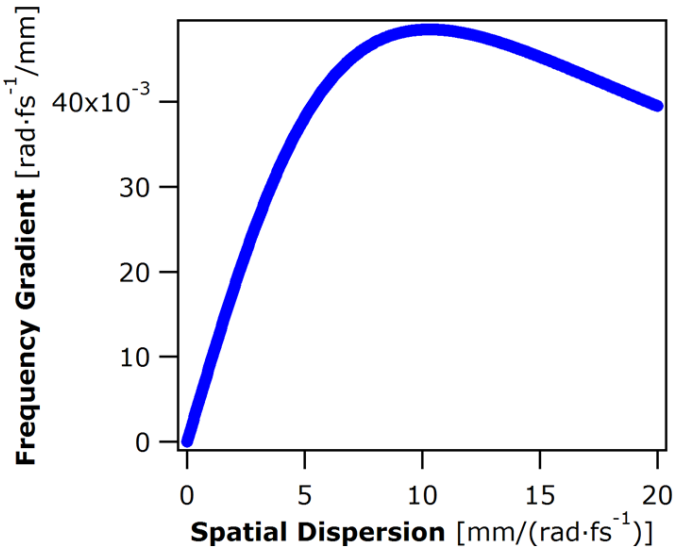

Figure 10: Theoretical plot of frequency gradient vs. spatial dispersion.

The distinction between the two definitions of spatial chirp is quite analogous to that between the definitions of temporal chirp in time and frequency domains. We can describe a linearly chirped Gaussian pulse either in the time domain,

$$E(t) = |E(t)| \exp\left[-\mathrm{i}\phi(t)\right] = E_0 \exp\left[-\left(\frac{t}{\Delta t}\right)^2\right] \exp\left(-\frac{\mathrm{i}}{2}\phi_2 t^2\right) \tag{18}$$

or equivalently in the frequency domain,

$$\tilde{E}(\omega) = \left|\tilde{E}(\omega)\right| \exp\left[-\mathrm{i}\varphi(\omega)\right] = \tilde{E}_0 \exp\left[-\left(\frac{\omega}{\Delta\omega}\right)^2\right] \exp\left(-\frac{\mathrm{i}}{2}\varphi_2\omega^2\right) \tag{19}$$

The two expressions are a Fourier transform pair.

The physical significance of temporal chirp parameters ϕ_2 and φ_2 can be viewed as such: In the time domain, $-\phi_2$ is the derivative of instantaneous (angular) frequency $\omega_0 \equiv -\frac{\mathrm{d}\phi(t)}{\mathrm{d}t} = -\phi_2 t$ with respect to t. On the other hand, in the frequency domain, φ_2 (often called group-delay dispersion) is the derivative of group delay $t_0 \equiv \frac{\mathrm{d}\varphi(\omega)}{\mathrm{d}\omega} = \varphi_2\omega$ with

respect to ω. Parameters $\phi_2 = -\frac{\mathrm{d}\omega_0}{\mathrm{d}t}$ and $\varphi_2 = \frac{\mathrm{d}t_0}{\mathrm{d}\omega}$ are two different, but equivalent, parameters describing temporal (spectral) chirp in the time/frequency domains, just as parameters $\zeta = \frac{\mathrm{d}x_0}{\mathrm{d}\omega}$ and $\upsilon = \frac{\mathrm{d}\omega_0}{\mathrm{d}x}$ are the parameters describing spatio-temporal chirp in the frequency/space domains. Indeed, the relationship between ϕ_2 and φ_2 is:

$$\varphi_2 = \frac{-\phi_2}{\frac{1}{4}\phi_2^2 + \frac{1}{(\Delta t)^2}} \tag{20}$$

which follows from the Fourier transform and is remarkably similar to the relationship between ζ and υ (Eq. 16) for the case of spatial chirp.

The experimental process that introduces temporal chirp determines whether ϕ_2 or φ_2 is the fundamental parameter. For example, propagation through a linear dispersive material will add phase term to the electric field in frequency domain, leaving the spectrum unchanged. The field in the time domain, found by inverse Fourier transform, will then show pulses that are temporally longer (or shorter). On the other hand, self-phase modulation adds a ϕ_2 phase term in the time domain, leaving the temporal intensity unchanged. Fourier transforming to the frequency domain will then yield a broader spectrum.

Likewise, the various occurrences of spatial chirp require a consideration of one spatial-chirp parameter or the other. For example, in pulse shaping, frequency gradient determines the mapping of spatial modulation to spectral modulation. However, other optical devices, including pulse stretchers and compressors, are best modelled using spatial dispersion. From our definition, we can see that the two parameters are related in a complicated way, involving both the beam width and the frequency bandwidth. Indeed, there is a maximum frequency-gradient value one can achieve with given pulse and beam parameters. Knowing the relationship between these two parameters should help achieve better control of experimental conditions involving spatial chirp.

To conclude this section, we have proposed and compared two definitions of spatial chirp, namely, spatial dispersion and frequency gradient. We derived the relationship between the two parameters, and we find it analogous to that between the two quadratic-phase parameters characterizing temporal chirp in the time/frequency domains.

2.3 Measuring spatial chirp in ultrashort pulses using single-shot Frequency Resolved Optical Gating

2.3.1 Introduction

Because their generation involves considerable spatio-temporal manipulations, ultrashort laser pulses commonly suffer from spatio-temporal distortions. Probably the most common such distortion is spatial chirp, in which the average wavelength of the pulse varies spatially across the beam. Devices such as pulse compressors (see Figure 11), which are standard in essentially all ultrafast lasers and apparatuses, deliberately introduce massive amounts of spatial chirp, only to-in principle-remove it afterward. After two prisms, the beam lacks angular dispersion, but has considerable linear spatial chirp. While the next two prisms of a pulse compressor (or the beam reflected back on with a mirror), in principle, remove this effect, in practice they typically do not completely do so unless aligned perfectly. One cause of this distortion is that the first and last prism separations may not be equal. Using only two prisms and a mirror or mirrors to reflect the beam back on itself guarantees that the relevant prism separations are equal, but there are other causes of spatial chirp in pulse compressors even in such a simple two-prism arrangement: the beam may be diverging or converging while inside the device, or the prisms may be arranged at slightly different angles. As a result, the beam emerging from a pulse compressor is frequently contaminated with spatial chirp.

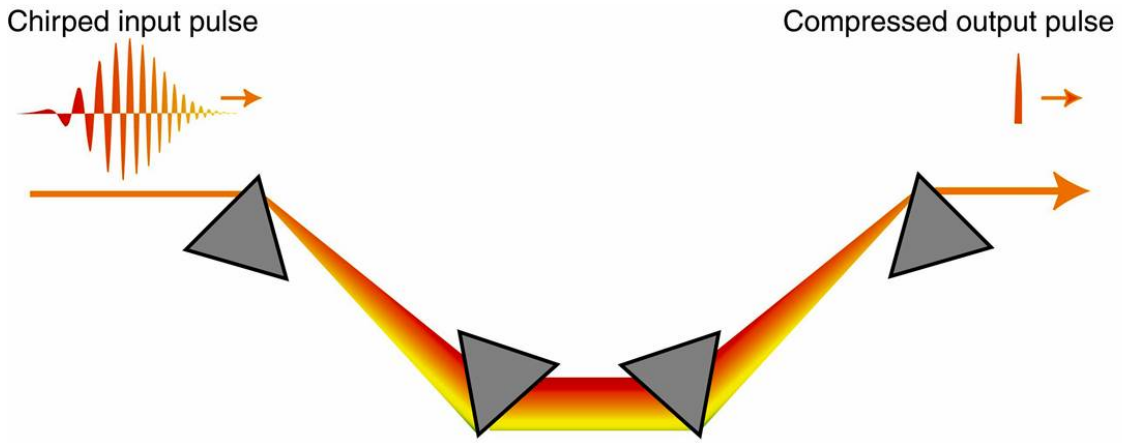

Figure 11: A four-prisms pulse compressor.

Worse, spatial chirp has many additional causes, including even optics that would seem beyond suspicion. For example, a window with a slight wedge, as is required for laser output couplers (to avoid feedback from the back surface), causes angular dispersion, which also imparts spatial chirp in the beam, and the further that the beam propagates from the optic the more spatial chirp. This is especially problematic in the most broadband (that is, the shortest) pulses. Even a simple tilted plane-parallel window yields unavoidable spatial chirp (Figure 6). Thus, simply placing a (usually 45-degree) pick-off mirror in the beam causes spatial chirp in the transmitted beam.

If a pulse has spatial chirp, experiments performed with it will yield inappropriate results. For example, each individual ray along the beam will contain only a fraction of the full pulse spectrum, and hence won't be as short as would be possible if the pulse possessed the full spectrum of the beam. Also, spectroscopic experiments performed with spatially chirped pulses will involve both exciting and probing with spatially varying wavelength, which could easily confuse their interpretation. Even worse are the potential effects of spatial chirp on a laser-induced-grating experiment. If the grating is induced with a spatially chirped pulse and its spatially reflected replica (i.e., a pulse that has experienced, for example, one more or one less reflection), it will be a stationary grating (as expected) in the beam center, but a moving grating at the edges due to the different center wavelengths of the two beams creating the grating in these regions. The moving grating will wash out due to its motion, in addition to excited-state decay. Such a grating will appear shorter-lived than might otherwise be imagined.

Despite its commonness and ubiquity, there has not been much diagnostics proposed for spatial chirp. A spatially resolved spectral measurement, in principle, suffices, but aberrations in spectrometers can mimic this effect, so such measurements are not routinely made. Researchers have also used spatially resolved spectral interferometry [69] and spatially resolved SPIDER (Spectral Phase Interferometry for Direct Electric Field Reconstruction) [40, 25], but these interferometric methods are difficult to align. SPIDER is also experimentally very complex and has within its apparatus a pulse stretcher, which significantly disperses the beam and requires very careful alignment or it will introduce spatial chirp

itself. Also, spectral interferometry requires high stability of the absolute phase of the pulse to be measured. While the latter two methods have measured the full intensity and phase vs. one spatial co-ordinate (not just the spatial chirp), it is important to develop a device for measuring spatial chirp in ultrashort laser pulses that is simple, easy to use, reliable, artifact-free, and accurate.

In this note, we report such a device. Remarkably, it is a familiar one: any single-shot second-harmonic-generation frequency-resolved-optical-gating (SHG FROG [43]) device, including the extremely simple FROG device we recently reported for measuring an ultrashort pulse's intensity and phase vs. time, GRENOUILLE [65]. We will show that, without a single modification, single-shot FROG and GRENOUILLE yield the pulse spatial chirp, in addition to the intensity and phase vs. time. Specifically, the ordinarily symmetrical (unsheared) SHG FROG trace develops a shear in the presence of spatial chirp, which is proportional to the spatial chirp.

Even better, the inversion formula is very simple. First note that a single-shot SHG FROG maps delay onto position and hence yields a plot of intensity vs. frequency and position, and a spatio-spectral diagnostic for spatial chirp involves a similar plot. As a result, the FROG-trace shear is naturally related to the spatial chirp. This technique also works for higher (odd) orders of spatial chirp. And we show that the effects of spatial chirp may be removed from the FROG trace, and the pulse intensity and phase can be determined in the usual manner. The retrieved intensity and phase may then be modified taking into account the spatial chirp, and a spatio-temporal measurement of the pulse obtained for a spatially chirped pulse.

2.3.2 Theory of spatial chirp in single-shot FROG measurements, such as GRENOUILLE

Figure 12 shows the effect of spatial chirp on single-shot FROG trace. Two spatially chirped pulses are crossed at an angle in the SHG crystal. This yields variable delay mapped onto transverse axis. The crystal yields the autocorrelation signal of the pulse for the purpose of measuring its intensity and phase vs. time. However, spatial chirp causes a variation of the autocorrelation signal wavelength vs. distance (i.e., vs. delay). This yields a shear in

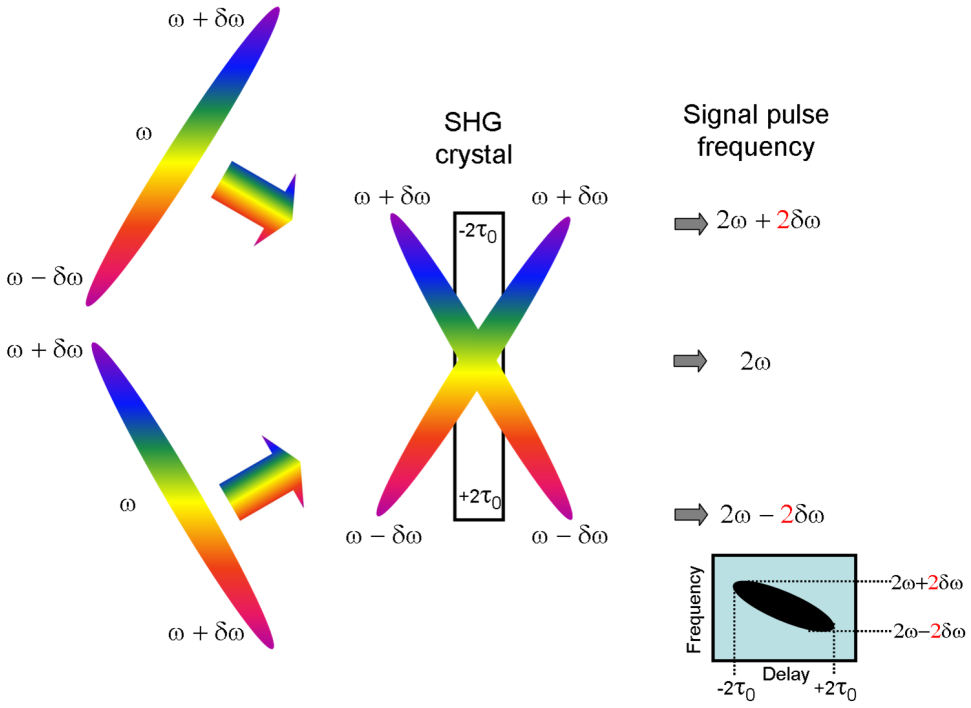

Figure 12: Spatial chirp in single-shot SHG FROG.

the SHG FROG trace proportional to the magnitude of the spatial chirp.

To see this mathematically, we begin with the usual expression for an SHG FROG trace, including the carrier frequencies of the two pulses [42]:

$$I_{FROG}^{SHG}(\omega,\tau) = \left| \int_{-\infty}^{\infty} \{E(t)\exp[i\omega_0 t]\} \quad \{E(t-\tau)\exp[i\omega_0 (t-\tau)]\} \quad \exp[-i\omega t] \;\; dt \right|^2 \tag{21}$$

which can be simplified to yield:

$$I_{FROG}^{SHG}(\omega,\tau) = \left| \int_{-\infty}^{\infty} E(t)\; E(t-\tau)\; \exp[-i(\omega - 2\omega_0)\, t]\; dt \right|^2 \tag{22}$$

In single-shot FROG techniques, two replicas of the pulse are crossed at a large angle, and delay is mapped onto position, $\tau = \alpha x$, where $\alpha = 2\sin(\theta/2)/c$. This yields: $I_{FROG}^{SHG}(\omega, \alpha x)$.

Now if we allow the pulses to have spatial chirp (or, in particular, frequency gradient: $\upsilon \equiv \frac{\mathrm{d}\omega_0}{\mathrm{d}x}$) in a single-shot SHG FROG set up, we must replace ω_0 with a spatially dependent frequency: $\omega(x) = \omega_0 + \upsilon x$. Then the SHG FROG trace becomes:

$$\left| \int_{-\infty}^{\infty} E(t)\exp[i(\omega_0 + \upsilon x)t]\; E(t-\tau)\exp[i(\omega_0 + \upsilon x)(t-\tau)]\; \exp[-i\omega t]\; dt \right|^2 \tag{23}$$

Simplifying this expression, we obtain:

$$I_{FROG}^{SHG}(\omega, \alpha x) = \left| \int_{-\infty}^{\infty} E(t)\ E(t-\tau)\ \exp[-i(\omega - 2\omega_0 - 2\upsilon x)t]\ dt \right|^2 \tag{24}$$

which can be written in terms of $I_{FROG}^{SHG}(\omega, \alpha x)$:

$$I_{FROG}^{SHG}(\omega - 2\upsilon x, \tau) \tag{25}$$

Since, in single-shot FROG techniques, delay is mapped onto position, $\tau = \alpha x$, the single-shot SHG FROG trace of a pulse with spatial chirp will be:

$$I_{FROG}^{SHG\ sp\ ch}(\omega, \tau) \rightarrow I_{FROG}^{SHG}(\omega - 2\upsilon x, \alpha x) \tag{26}$$

This expression shows that the SHG FROG trace, which is normally symmetrical with respect to delay, $I_{FROG}^{SHG}(\omega, -\alpha x) = I_{FROG}^{SHG}(\omega, \alpha x)$, develops shear in the presence of spatial chirp and no longer exhibits such symmetry. Because no other effect is known to cause such an asymmetry, this is a simple and clear indicator of spatial chirp.

GRENOUILLE [65] is a type of single-shot FROG measurement, but it (like single-shot FROG methods that involve mirrors inserted halfway into the beam) involves spatially splitting the beam in two, rather than splitting the beam with a beam splitter. In other words, the left side of the beam gates the right side of the beam, rather than the entire beam gating itself. The effect of spatial chirp on a GRENOUILLE trace is shown in Figure 13). A spatially chirped pulse enters the Fresnel biprism from the left. The Fresnel biprism splits the pulse into two, which then cross in the SHG crystal. While the crystal yields the autocorrelation signal of the pulse for the purpose of measuring its intensity and phase vs. time, spatial chirp causes a variation of the autocorrelation signal wavelength vs. distance. This yields a shear in the GRENOUILLE trace proportional to the magnitude of the spatial chirp. Note that the slopes in both single-shot SHG FROG and GRENOUILLE are exactly the same. Therefore, the mathematical analysis that we did for single-shot FROG also works for GRENOUILLE.

Since GRENOUILLE uses a Fresnel biprism, it also introduces spatial chirp. However, not only it is very small compared to other sources (since the apex angle is very close to 180^0), but also it has no effect on the measurements since it is symmetric with respect to

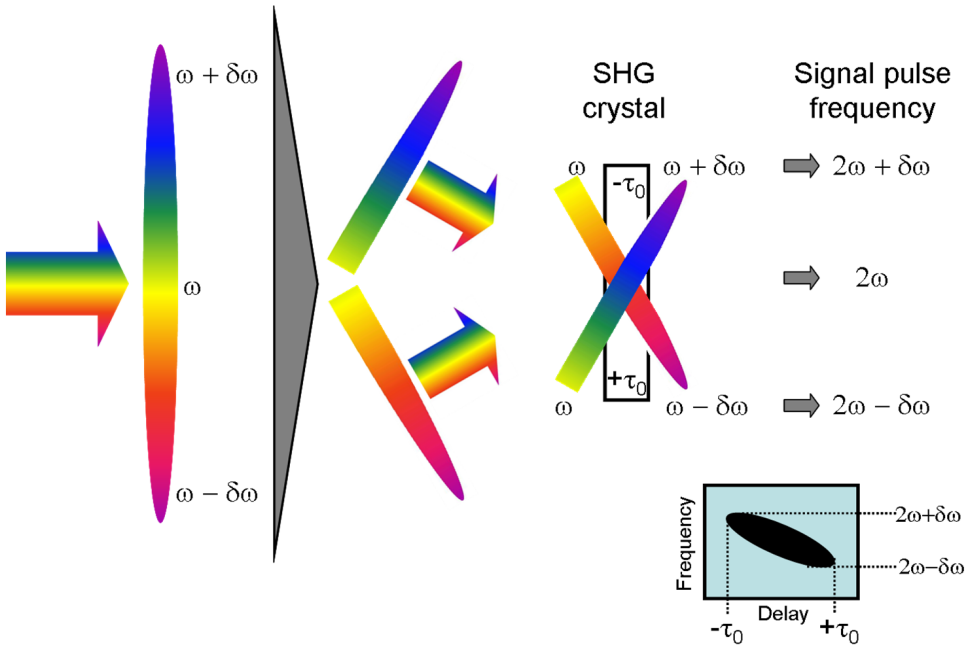

Figure 13: Spatial chirp and GRENOUILLE.

propagation direction. Note that this derivation also holds for all odd (i.e., higher) orders of spatial chirp. On the other hand, even orders of spatial chirp will produce symmetrical distortions in the trace and would be confused for pulse distortions in time and hence require another (yet-to-be-invented) technique for their identification.

2.3.3 Trace Shears in Single-Shot SHG FROG, GRENOUILLE, and Spatio-Spectral Plots

Measuring the spectrum vs. one spatial co-ordinate for a pulse yields a spatio-spectral plot. If the pulse has spatial chirp (e.g. frequency gradient), $\omega(x) = \omega_0 + \upsilon x$, this plot will be sheared with slope υ. This is the most obvious way to measure the spatial chirp. Now, we can also compute the slope of the SHG FROG (or GRENOUILLE) trace vs. position. (We usually describe FROG and GRENOUILLE measurements in terms of the delay, but single-shot measurements map delay onto position, and position is the more natural unit for discussions of spatial chirp.) Simple examination of the expression for the sheared SHG FROG trace of a pulse with spatial chirp (26 shows that its frequency vs. position shear is $\omega_{ave}(x) = 2\upsilon x$. However, the position 'x' here is not beam transverse coordinate as in the case of spatio-spectral plots, but is instead the crystal transverse coordinate. They

are simply related by a factor of $\cos(\theta/2)$, where θ is the beam crossing angle. So, the SHG FROG trace slope is $2\upsilon/\cos(\theta/2)$. Since the cosine factor is approximately unity, the frequency gradient-induced slope of the FROG trace is approximately twice the frequency gradient and twice that of the spatio-spectral trace when plotted vs. frequency. When plotted vs. wavelength, recall that the SHG FROG trace occurs at the second harmonic. Converting from frequency to wavelength, a factor of 2 must be included, reducing the slope of the FROG trace by a factor of 4 and yielding a new ratio of 1/2, rather than 2, for traces plotted vs. wavelength.

2.3.4 Experiment

To introduce variable amounts of spatial chirp into a pulse, we modified the usual prism pulse compressor, placing mirrors between last two prisms, deflecting the pulse to two additional mirrors mounted on translation stage (see Figure 14). By translating the latter two mirrors, we were able to align and (deliberately) misalign the compressor, obtaining positive, zero, or negative spatial chirp. Also, we aligned the compressor so that the angular dispersion was close to zero in all of our measurements, although we do not believe that the presence of angular dispersion would alter our results.

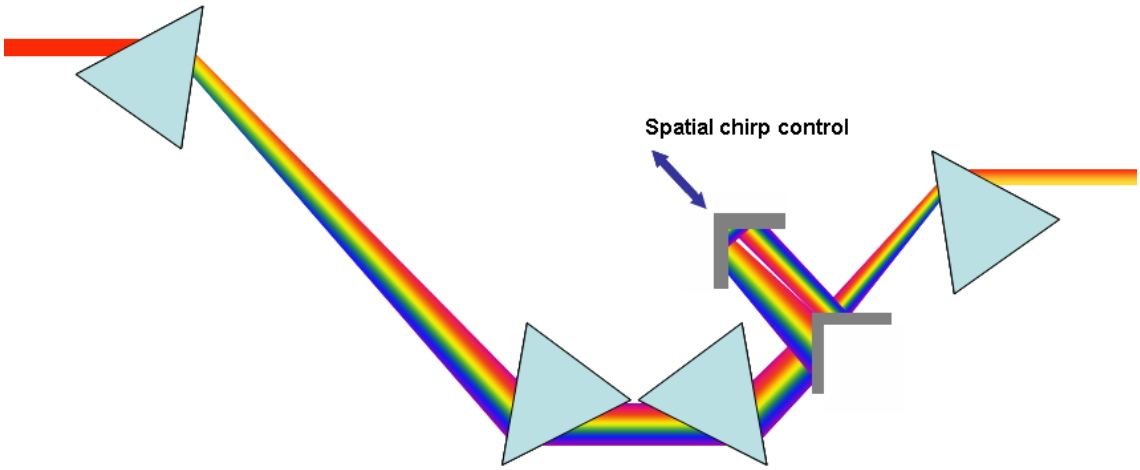

Figure 14: Modified prism pulse compressor can be used to introduce the desired amount of spatial chirp.

Using this setup, we performed pulse measurements for various amounts of spatial chirp

using GRENOUILLE. We determined the spatial-chirp parameter, υ, from the measured GRENOUILLE trace from the linear slope of the trace (wavelength vs. delay) using the approach described in the previous section. We also made independent measurements of the spatial chirp parameter, υ, from a spatially resolved spectral measurement using a carefully aligned imaging spectrometer.

Figure 15 shows GRENOUILLE traces and spatio-spectral plots of pulses with different amounts of spatial chirp for some of the experiments we have performed. As seen in the figures, when the spatial chirp is increased, the shear of the GRENOUILLE traces increase along with the shears of the spectra. These figures nicely illustrate the effect of spatial chirp on experimental GRENOUILLE traces. The GRENOUILLE traces also get wider in the delay axis as our setup to introduce spatial chirp also introduces GVD.

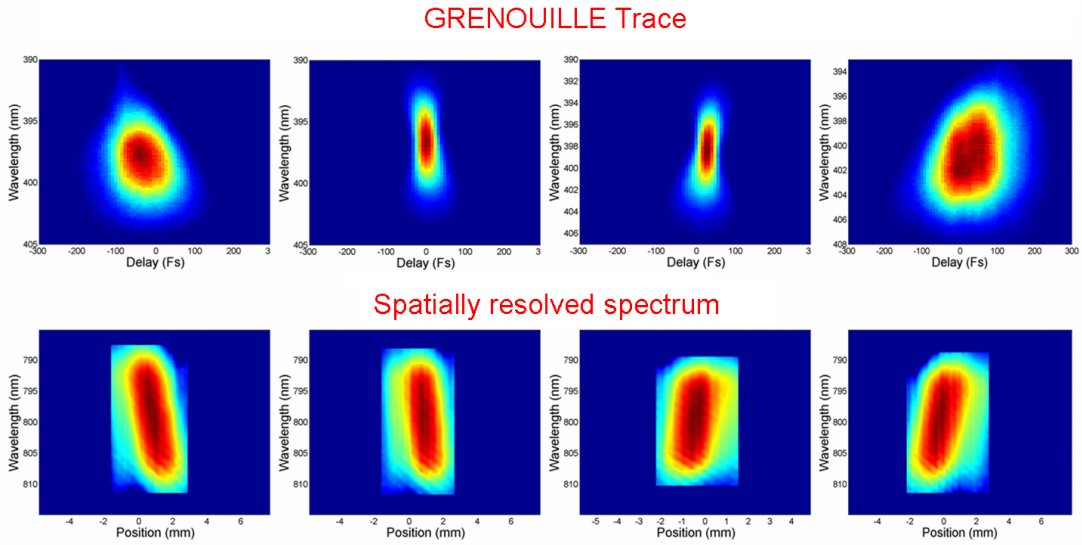

Figure 15: Experimental GRENOUILLE traces and spatio-spectral plots.

For a quantitative analysis, we calculated the slopes of both the GRENOUILLE traces and spatio-spectral plots. As shown in Figure 16, the slopes obtained from GRENOUILLE traces correlate very nicely with the slopes of spatio-spectral plots. The dependance also seems linear, but exact behavior is to be discussed at the end of this chapter. As a result, these measurements experimentally confirm that GRENOUILLE can reveal and measure

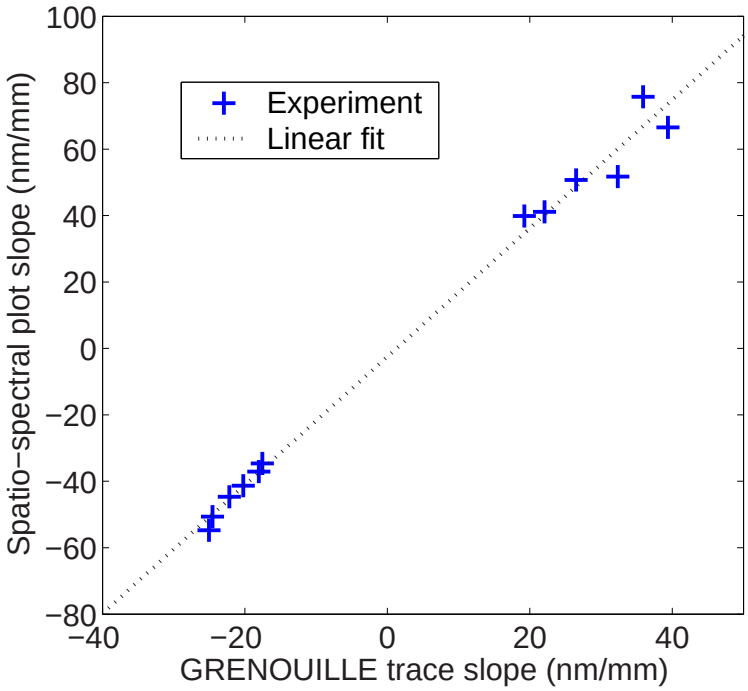

Figure 16: Slopes of GRENOUILLE traces and corresponding spectrum vs. position slopes for various amounts of spatial chirp.

spatial chirp. And it does so without doing a single alteration in its setup. This provides a practical and reliable alignment of pulse compressors used in ultrafast laser laboratories. Recall that the same device also measures the pulse intensity and phase!

Retrieving the pulse intensity and phase from a spatially chirped beam requires some attention. Theoretically, single-shot FROG traces (including GRENOUILLE traces) are always symmetric with respect to delay. Therefore, directly running the algorithm on a sheared (due to spatial chirp) trace will result in a high FROG error. Therefore, what can be done, instead is to remove the shear from the trace first, and then run the algorithm on it. The retrieved field, then, will be a good approximation to the field in the absence of spatial chirp.

However, in the presence of spatial chirp, due to lateral translation of frequency components, the effective pulse bandwidth is reduced, lengthening the pulse. What GRENOUILLE measures is this lengthened pulse, and even though the the trace shear reveals spatial chirp, by removing the shear and running the FROG algorithm, we will find the field of the pulse of the same length and temporal shape as it would be measured at

any particular point in the beam, but it is not the pulse if all the frequency components in the beam were synthesized.

2.4 Rigorous theory of GRENOUILLE measurements of spatial chirp

While the analysis of spatial chirp diagnostic with GRENOUILLE, described in the previous section, holds very nicely for qualitative arguments, certain difficulties arise for more quantitative analysis. As we show in section 2.2, there are two different forms of spatial chirp, and such an intuitive description and simple distortion retrieval are only valid for pulses having the form of spatial chirp that we call frequency gradient, in which the pulse center frequency (ω_0) depends on transverse position (x). It is more common, however, for pulses to be contaminated with a different type of spatial chirp, which we call "spatial dispersion," in which the beam center position (x_0) depends on frequency (ω). In fact, a pulse compressor (as we used in our experiments) introduces spatial dispersion as a free parameter, and frequency gradient will depend on the pulse parameters. The resulting distortion to the single-shot FROG or GRENOUILLE trace in the presence of spatial dispersion is more complicated, which prevents one from retrieving spatio-temporal distortions in a simple manner (in contrast to traces contaminated with frequency gradient).

In addition, in the mathematical analysis of the earlier sections, we did not study the effect of phase in detail. However, in presence of spatial chirp, the phase will also be a function of position, potentially affecting the measurement. This situation is most dramatic in the presence of third order spectral phase. If a pulse has both spatial chirp and third order spectral phase, not only the center frequency varies linearly with position, there is also a quadratic change in pulse arrival time (linear spectral phase term), and also a linear change in the temporal chirp (quadratic spectral phase term) with position. This is easily seen from the distorted field in frequency domain. A pulse with third order phase and spatial chirp can be written as:

$$E(x,\omega) = E_0 \exp\left(-\frac{1}{4}\omega^2\tau_0^2\right) \exp\left(-i\varphi_3\omega^3\right) \exp\left[-\frac{(x-\zeta\omega)^2}{w^2}\right] \tag{27}$$

Since, due to spatial chirp, the center frequency varies along x direction, it will be

informative to reorganize equation 27 as:

$$E(x,\omega) \propto \left(-\frac{1}{4}\omega_x^2\tau^2\right)\exp\left(-i\varphi_3\omega_x^3\right)\exp\left[-i\varphi_3\left(3vx\omega_x^2+3v^2x^2\omega_x+v^3x^3\right)\right] \tag{28}$$

where $\omega_x = \omega - vx$ is the position dependent center frequency.

It is well know that, linear phase term in frequency domain corresponds to simply a shift in the arrival time. Since the ω_x term in equation 28 is quadratically proportional to x, the pulse will have a parabolic arrival time (parabolic pulse-front) in the x position. Furthermore, the quadratic phase term has a linear x dependance, which corresponds to a linear variation of temporal chirp across x, in the time domain. Because of these new distortions in the pulse, the analysis shown in Figure 13 ceases to be adequate. The shear becomes a more complicated function of the pulse parameters.

A rigorous mathematical treatment of this will make use of a more general GRENOUILLE trace expression [32]. As it is not possible to derive analytical expressions for pulses with a complicated structure (like third and higher order phase in time domain), the best approach is to use computer simulations. Figure 17 shows experimental and simulated results of GRENOUILLE trace of a pulse with spatial dispersion and third order phase. It can be seen in both traces that the center of mass of the traces are not simple lines.

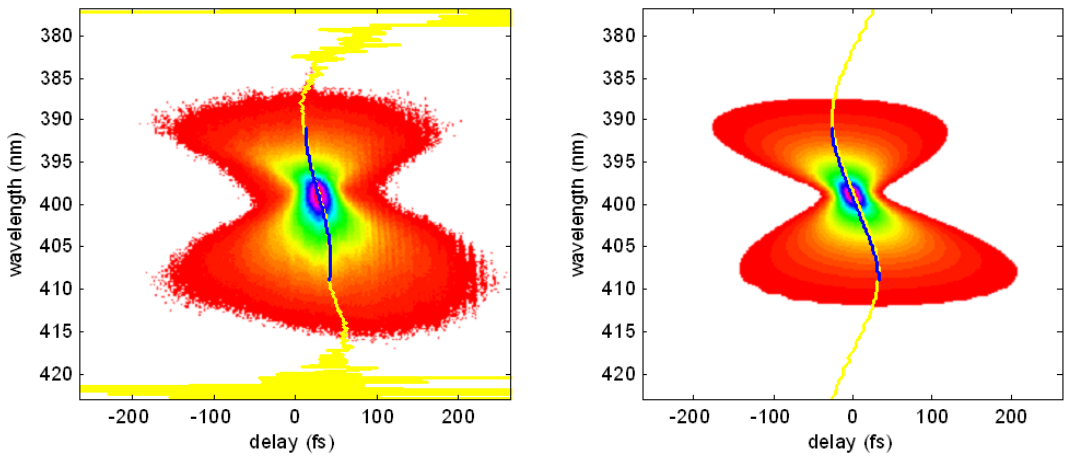

Figure 17: Simulated (left) and experimental (rigt) GRENOUILLE traces for a pulse that has spatial chirp and third order phase.

The qualitative match of the experiment and simulation as shown in Figure 17 encourages that it should be possible not only to reveal, but also measure spatial chirp from a distorted GRENOUILLE trace. Wang et.al. show that this is possible by changing the core of GRENOUILLE retrieval algorithm [93]. In their work, they establish a rigorous GRENOUILLE model in the presence of spatio-temporal distortions. Using this model, the GRENOUILLE trace of an arbitrary input spatio-temporal field can be calculated. They then demonstrate a new FROG retrieval algorithm capable of accurately retrieving both the pulse temporal characteristics and spatio-temporal distortion parameters from the distorted GRENOUILLE trace. Such an algorithm involves a major modification of the current commercial FROG pulse-retrieval programs. The details of the extension of the FROG retrieval algorithm to spatio-temporal distortions requires an extensive analysis and it is beyond the scope of this thesis (see [93] for details) .

CHAPTER III

MEASURING PULSE-FRONT TILT IN ULTRASHORT LASER PULSES

This chapter originally appeared as a paper by the author:

Selcuk Akturk, Mark Kimmel, Patrick O'Shea, Rick Trebino, "Measuring pulse-front tilt in ultrashort pulses using GRENOUILLE", Optics Express 11, 491-501 (2003) [4]

3.1 Introduction

Because their generation involves considerable spatio-temporal manipulations, ultrashort laser pulses commonly suffer from spatio-temporal distortions. The most common such distortions encountered in ultrafast laser laboratories are angular dispersion, spatial chirp and pulse-front tilt. Spatial chirp is the tendency of pulses to have the redder colors on one side of the beam and the bluer colors on the other, and it results from prism pairs and tilted windows, as shown in the previous chapter. Pulse-front tilt involves the pulse group fronts (intensity contours -instantaneous position of the peak of the pulse-) tilting with respect to the perpendicular to the propagation direction. In a very general sense, it results from the group velocity being different than phase velocity.

We have recently shown that single-shot second-harmonic-generation frequency-resolved optical gating (SHG FROG) and its experimentally very simple version, GRENOUILLE, easily measure the pulse spatial chirp [5], which is revealed as a shear (tilt) in the otherwise symmetrical measured FROG trace (see chapter 2 for details). As with spatial chirp, the main source of pulse-front tilt is devices such as pulse compressors or stretchers, which are standard in essentially all ultrafast lasers and apparatuses. Propagation through a dispersive device causes different frequency components of the beam to propagate at different angles, that is, angular dispersion, which also causes pulse-front tilt [11] (see Figure 18). Therefore, devices like pulse compressors, which, if not aligned correctly, introduce angular

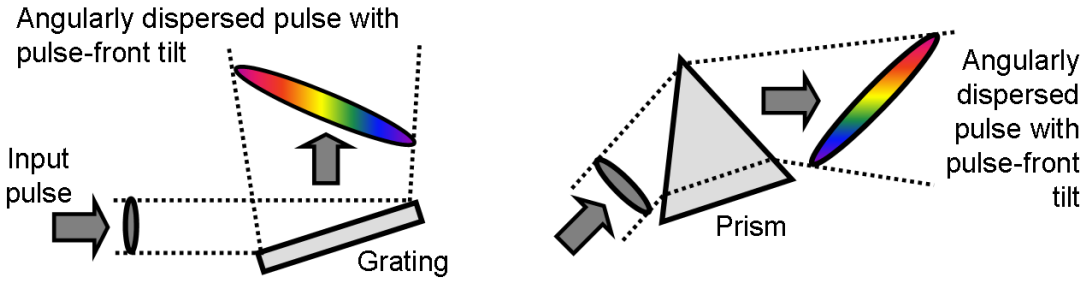

Figure 18: Elements that introduce angular dispersion also introduce pulse-front tilt.

dispersion, also introduce significant pulse-front tilt. In principle, a second prism with its inner surface perfectly parallel to that of the first prism completely removes the angular dispersion and pulse-front tilt introduced by the first. However, even minor non-parallelism or beam divergence leaves residual angular dispersion and pulse-front tilt. Devices like pulse compressors use four identical prisms and often yield pulse-front tilt at the output unless aligned perfectly. In two-prism configurations, which use only two prisms and a mirror or mirrors to reflect the beam back on itself, the beam may be diverging or converging while inside the device, causing slight shifts in angle of incidence, and hence pulse-front tilt. There are other possible sources of pulse-front tilt, like slightly wedged optical components. As a result, beams used in ultrafast laser laboratories are frequently contaminated with pulse-front tilt (and angular dispersion).

Indeed, since ultrashort pulses can be very broadband, pulse-front tilt can be significant and problematic. Probably the most significant problem is that pulses with pulse-front tilt are temporally broader than pulses without pulse-front tilt, and the assumption that temporal and spatial evolutions are independent ceases to be valid. Other problems arising due to pulse-front tilt include pulse frequency shifts and spatial profile variations [54].

Although pulse-front tilt occurs most of the times in a residual manner and needs to be avoided, there are a few cases where tilted pulse-fronts can actually be useful. One case is "travelling wave excitation (TWE)" [10, 44, 82]. Normally, in ultrashort lasers, amplified spontaneous emission (ASE) limits strongly the overall conversion efficiency. TWE uses tilt of a pulse-front of the pump with respect to the propagation direction of the signal pulse, in

an ultrashort laser cavity. In this configuration, the gain medium is inverted in synchronism with the propagating signal light, leaving practically no time for ASE.

Another exploitation of pulse-front tilt is demonstrated in achievement of group velocity matching of three-wave mixing (optical parametric amplification, for example) in a birefringent crystal [79]. In this case, the phase velocity of the interacting waves are matched using the birefringence of the crystal, and non-collinearly propagating the interacting waves. Group velocities are then matched using pulse-front tilt; Tilting the pulse-fronts of the interacting waves in a way that they have the same group velocity projection along a common axis. This match makes possible more-efficient mixing of short light pulses, and it permits efficient mixing of chirped or broadband light.

Whether it is desired or not, pulse-front tilt has to be measured, so that it is controlled when to be exploited, and it is eliminated when it is unwanted. However, despite its ubiquity and potential for mischief in ultrafast experiments, pulse-front tilt is not commonly measured, and only a few diagnostics have been proposed for it. The best existing method, "Spectrally resolved interference (SRI)" [88], is an interferometric method utilizing the spatial fringes formed when two beams cross at an angle. In this method, angular dispersion is actually measured and pulse-front tilt due to angular dispersion can easily be calculated [11]. In the setup of the SRI, the pulse (which has angular dispersion) and its replica is combined and sent to a spectrometer. Normally, when two monochromatic light waves cross at an angle, fringes are generated in transverse position and the fringe separation is inversely proportional to the crossing angle. When it has angular dispersion, a broadband light will have different propagation angles for different wavelengths. Therefore, at the output of the spectrometer, the fringe separation will vary with the wavelength. The setup can be adjusted such that at a particular wavelength, the propagation angles are the same and the fringe separation is infinity. Then, by tilting one of the input beams and measuring the shift of the wavelength for parallel fringes, angular dispersion can be measured. This method provides high precision measurement, but, like other interferometric measurements, it requires good temporal coherence and involves considerable labor for its alignment.

A simpler measurement of angular dispersion (and pulse-front tilt due to it) using an

imaging spectrometer is also demonstrated [47]. In this method, the pulse with angular dispersion is focused to the entrance slit of an imaging spectrometer, such that different propagation angles are mapped to position along the entrance slit. Therefore, at the output, a CCD will detect a tilted spectrum, which indicates and measures angular dispersion. Although this method yields a quick analysis, it fails dramatically if the pulse also has spatial chirp, which is very likely due to angular dispersion.

Researchers have also used spatially resolved spectral interferometry [69] and spatially resolved SPIDER [40, 25], but these interferometric methods are also difficult to align and to keep aligned. SPIDER is also experimentally very complex and has within its apparatus a pulse stretcher, which significantly angularly disperses the beam and requires very careful alignment or it will itself introduce spatio-temporal distortions, including pulse-front tilt. In order to measure spatio-temporal characteristics, a Michelson interferometer also needs to be added to the setup (to generate spatial shear), which makes it even more complicated. In addition, spectral interferometry requires high stability of the absolute phase of the pulse to be measured.

Adjustment of pulse-front tilt with a modified single-shot autocorrelator has also been suggested [75, 70] and is available commercially as a "tilted-front-pulse autocorrelator". This device is often used in practice for revealing pulse-front tilt and adjusting the elements that cause it. However, it not only suffers from ambiguities in temporal intensity (and it does not measure the phase [87]), but also it only indicates the presence of pulse-front tilt qualitatively; it does not provide quantitative measurement of it or yield its sign.

In this note, we report a device for measuring pulse-front tilt that is simple, easy to use, reliable, artifact-free, and accurate. As in a previous publication [5], where we showed that GRENOUILLE [65] measures spatial chirp as well as the intensity and phase-without a single modification-here we show that GRENOUILLE also measures pulse-front tilt, and again it also does so without a single modification in its setup. Indeed, GRENOUILLE can measure both of these distortions both accurately and simultaneously-and in addition to the pulse intensity and phase.

This works because GRENOUILLE is a very symmetrical device, in which the pulses

necessarily cross in space and time, typically at the center of the crystal, which can be made to coincide with the center of the CCD camera. Therefore, pulses without pulse-front tilt will generate their maximum-intensity second-harmonic signal at the center of the crystal (at zero relative delay). This also centers the trace on the camera. The effect of pulse-front tilt is then to move the traces off to one side or the other of the crystal. And the shift from the center of the crystal is proportional to pulse-front tilt angle. Since no other effect is known to cause such a shift, GRENOUILLE traces unambiguously reveal and measure pulse-front tilt and its relative, angular dispersion [11]. This means that GRENOUILLE, despite its ultrasimple apparatus, easily reveals a wide range of ultrashort-pulse characteristics: intensity and phase vs. time, spectrum and spectral phase, spatial chirp, and pulse-front tilt. And the apparatus can be easily bypassed, allowing the camera used for these measurements to easily reveal the beam spatial profile, too.

3.2 Theory of pulse-front tilt in GRENOUILLE measurements

We begin by showing that, although standard arrangements of single-shot SHG FROG measures spatial chirp, it does not measure pulse-front tilt. The usual expression for SHG FROG traces is similar to that for GRENOUILLE [87], so, to see the effect of pulse-front tilt on FROG traces, we start with the better known analytical expression for the SHG FROG trace:

$$I_{FROG}^{SHG}(\omega,\tau) = \left| \int_{-\infty}^{\infty} \{E(t)\exp[i\omega_0 t]\} \quad \{E(t-\tau)\exp[i\omega_0 (t-\tau)]\} \quad \exp[-i\omega t] \;\; dt \right|^2 \quad (29)$$

In single-shot FROG, the effect of pulse-front tilt is to add a position-dependent time $t(x) = px$, where p is pulse-front tilt parameter, which can be expressed as $p = \delta t/\delta x$. Then the SHG FROG trace becomes:

$$\begin{aligned} & I_{FROG}^{SHG\,pft}(\omega,\tau) \quad = \\ & \left| \int_{-\infty}^{\infty} E(t+px)\exp[i\omega_0 t] \; E(t+px-\tau)\exp[i\omega_0 (t-\tau)] \; \exp[-i\omega t] \; dt \right|^2 \end{aligned} \quad (30)$$

where we have omitted the complex exponentials that will vanish when the magnitude is squared later. By changing variables, $t' = t + px$, we can simplify 30:

$$\begin{aligned} &\left| \int_{-\infty}^{\infty} E(t') \exp[i\omega_0 t'] \; E(t' - \tau) \exp[i\omega_0 (t' - px - \tau)] \; \exp[-i\omega (t' - px)] \; dt' \right|^2 \\ &= \left| \int_{-\infty}^{\infty} E(t') \exp[i\omega_0 t'] \; E(t' - \tau) \exp[i\omega_0 t'] \; \exp[-i\omega t'] \; dt' \right|^2 \\ &= I_{SHGFROG}(\omega, \tau) \end{aligned} \tag{31}$$

This indicates that, for single-shot SHG FROG, pulses with tilted fronts yield the same expression as pulses without pulse-front tilt, and hence the single-shot SHG FROG trace does not depend on, that is, does not measure, the pulse-front tilt. Figure 19 shows this pictorially: Pulses without pulse-front tilt (shown in green) yield traces centered on the crystal, where zero relative delay occurs. Pulses with pulse-front tilt (shown in red), also yield traces centered at the same point. Therefore, single-shot SHG FROG does not distinguish pulse-front tilt (Magnitude of tilt exaggerated for clarity.). This is also true of other FROG beam geometries. Pulse-front tilt does, however, change the delay calibration, so this must be taken into account (using a reference double-pulse with known pulse separation as a calibration, as is commonly done).

However, GRENOUILLE is slightly different. Unlike SHG FROG, which usually uses a partial reflector to split the beam in two, GRENOUILLE splits the same pulse from the center (one side of the beam gates the other). As a result, in GRENOUILLE, pulse-front tilt introduces an extra average delay, $+\tau_0$, in one pulse and an average advance $+\tau_0$ in the other. Then the expression for GRENOUILLE traces, in the presence of pulse-front tilt becomes:

$$\left| \int_{-\infty}^{\infty} E(t + \tau_0 + px) \exp[i\omega_0 t] \; E(t - \tau_0 + px - \tau) \exp[i\omega_0 (t - \tau)] \; \exp[-i\omega t] \; dt \right|^2 \tag{32}$$

Letting $t' = t + \tau_0 + px$:

$$\left| \int_{-\infty}^{\infty} E(t') \exp[i\omega_0 t'] \; E(t' - 2\tau_0 - \tau) \exp[i\omega_0 (t' - \tau_0 - px - \tau)] \; \exp[-i\omega (t' - \tau_0 - px)] \; dt' \right|^2 \tag{33}$$

Cancelling out the vanishing complex exponentials:

$$\begin{aligned} &\left| \int_{-\infty}^{\infty} E(t') \exp[i\omega_0 t'] \; E(t' - 2\tau_0 - \tau) \exp[i\omega_0 t'] \; \exp[-i\omega t'] \; dt' \right|^2 \\ &= I_{SHGFROG}(\omega, \tau + 2\tau_0) \end{aligned} \tag{34}$$

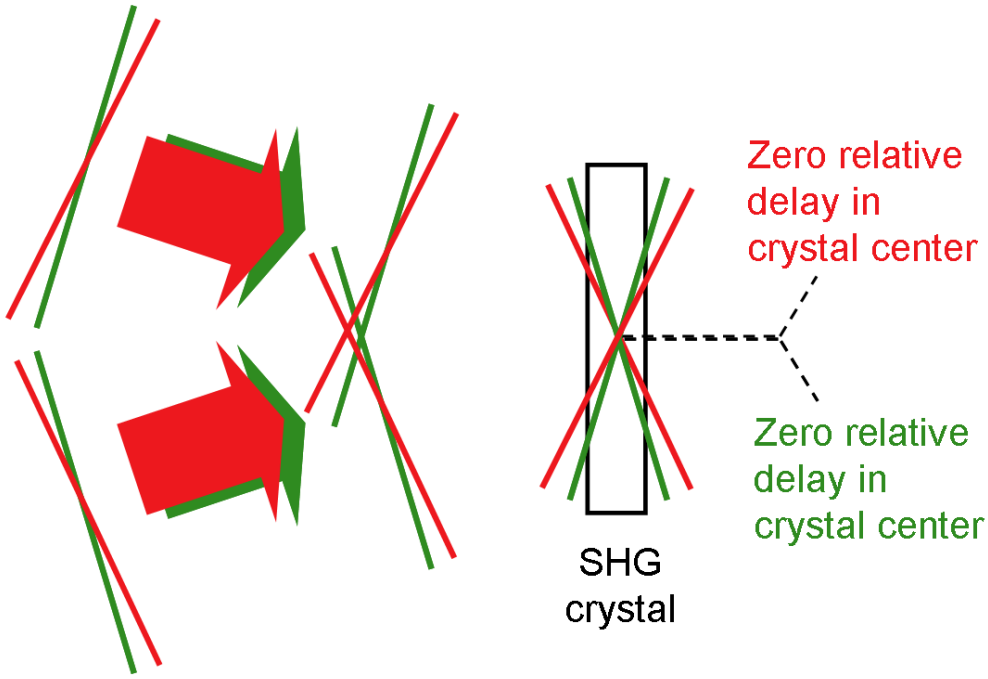

Figure 19: Effect of pulse-front tilt in single-shot SHG FROG.

This last expression clearly indicates that pulses with tilted fronts yield GRENOUILLE traces that are shifted (on the delay axis), compared to pulses without pulse-front tilt (Figure 20). Pulses without pulse-front tilt yield traces centered at the crystal, where zero relative delay occurs. However pulses with pulse-front tilt , cause the zero relative delay to be off to the side of the crystal.

It is possible to align the device so that the second-harmonic signal produced by pulses without pulse-front tilt is centered on the CCD camera. Therefore, any shift of the trace from the center can be attributed to pulse-front tilt, since no other effect causes such an asymmetry in GRENOUILLE traces. Note also that this result is independent of the pulse intensity and phase; the method is general.

The most straightforward way to align GRENOUILLE for pulse-front tilt measurement is as follows: An arbitrary femtosecond pulse is first measured with GRENOUILLE. Then the same pulse is measured with either the pulse or the GRENOUILLE flipped in a direction perpendicular to plane of pulse-front tilt (since the device is so compact, it is actually easier to flip it, rather than the pulse). The midpoint between the trace centers of the two

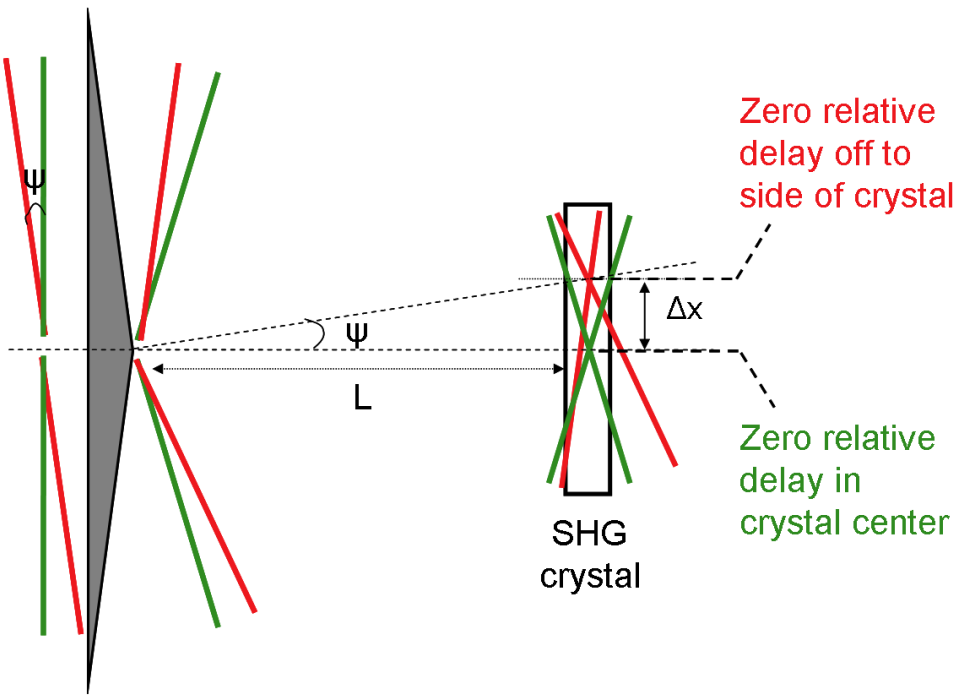

Figure 20: Measuring pulse-front tilt with GRENOUILLE

measurements yields the absolute center of the CCD and hence the crystal. Note that this evaluation does not require a pulse-front tilt free pulse.

There is also a very small amount of pulse-front tilt imposed in each beam by the biprism, but it is of opposite sign for the two beams and does not introduce any trace displacement and hence does not bias the measurement. It does affect the delay calibration, but this is taken into account by the standard delay calibration methods [100] and hence does not affect the measurement.

3.3 Numerical evaluation of the pulse-front tilt and extraction of the intensity and phase from a shifted trace

The shift of the trace from the center of the crystal reveals pulse-front tilt in the beam. It is also possible to extract the numerical value of pulse-front tilt from the amount of shift (Figure 20). The tilt angle of the beam is can be written as [11, 53]:

$$\tan\psi = c\frac{\partial t}{\partial x} = cp \tag{35}$$

From the Figure, it is easy to note that another expression for this angle is:

$$\tan\psi = \frac{\Delta x}{L} \tag{36}$$

where L is the separation between Fresnel biprism and second harmonic crystal, and x is the shift of the trace center. Equating Eqs. 35 and 36 we obtain:

$$p = \frac{\partial t}{\partial x} = \frac{\Delta x}{Lc} \tag{37}$$

This equation shows that the numerical value of pulse-front tilt is directly proportional to the amount of shift and the distance between the crystal and Fresnel biprism.

Finding the amount of shift and using Eq. 37 yields the pulse-front tilt, p. The shift can be found in several ways, but, for traces with Gaussian intensity profile, the peak of the trace can be found by a Gaussian fit at the central spectrum. Then the amount of shift is found simply by extracting the central delay from this value (note that, for GRENOUILLE, delay and position are proportional [87]). The pulse-front tilt can then be removed from the trace by simply translating to the center, which yields true GRENOUILLE trace for E(t):

$$I_{FROG}^{SHG}(\omega,\tau) = I_{FROG}^{SHGpft}(\omega,\tau - 2\tau_0) \tag{38}$$

The resulting trace is now the best estimate for the actual trace-and hence the pulse-in the absence of pulse-front tilt. The SHG FROG algorithm can then be run on the now symmetrical (centered) trace, yielding the pulse intensity and phase in the absence of pulse-front tilt. The pulse-front tilt can then be added back into the retrieved pulse, reproducing the pulse with the appropriate amount of pulse-front tilt. Note that a pulse with pulse-front tilt will typically be longer due to the concomitant angular dispersion and its spectral lateral walk-off [54]. The spectral lateral walk-off reduces the effective available bandwidth at a given point, thus increasing the pulse width.

The pulse can then be reconstructed using the retrieved intensity and phase and including the measured pulse-front tilt. Specifically, if the FROG algorithm returns an intensity, I(t), and phase, $\phi(t)$, then the pulse-front-tilted pulse field will be given by:

$$E(x,t) = \sqrt{I(t+px)}\exp[i(t+px)\omega_0 - i\phi(t+px)] \tag{39}$$

3.4 Experiment

Probably the easiest way to introduce variable amounts of pulse-front tilt into an ultrashort pulse is to use a single prism (or grating) at different angles of incidence. We have performed one set of experiments using this method. However, this method only achieves large values of pulse-front tilt and in only one direction, so we have performed another set of experiments by using a "modified pulse compressor," which is a standard pulse compressor with one of the prisms placed on a rotation stage. As mentioned earlier, any amount of non-parallelism (or, in our case, deviation from the angle of minimum deviation) causes pulse-front tilt. Therefore, with this setup, we can deliberately misalign and align the pulse compressor to get zero, positive, or negative pulse-front tilt.

While there is little or no subtlety in our techniques for generating or measuring pulse-front tilt, there is a major subtlety in understanding it in real laser beams. For Gaussian beams, pulse-front tilt changes as the pulse propagates (i.e., diverges or converges) [54, 89]. The change in the tilt depends on the beam parameters (spot size, the distance between the dispersive element and the beam waist, and the distance between the dispersive element and the observation point). And, depending on these parameters, this change can be very significant (See Figure 21. A 69^0 apex-angle fused-silica prism is used for calculation.). It can usually be neglected only for very well collimated beams.

The subtlety originates from two approaches of defining angular dispersion [89]. It can be defined as the angle between propagation direction of two different frequency components. Or alternatively, it can be defined as the angle between phase fronts of different frequency components. While these two quantities are same for plane waves, they differ for waves with non-planar phase front, as in the case of Gaussian laser beams (which has circular phase fronts). This difference is illustrated in Figure 22. Since pulse-front tilt is proportional to the second definition of angular dispersion, we will focus on that. The relation between the two angles in Figure 22 can be easily found to be (for small angles):

$$\Delta\Theta' = \Theta\Delta\left(1 - \frac{s}{R}\right) = \Theta\Delta\frac{d\left(d + \alpha^2 s\right) + z_R^2}{\left(d + \alpha^2 s\right)^2 + z_R^2} \tag{40}$$

where d is the distance between beam waist and prism; s is the distance between prism and

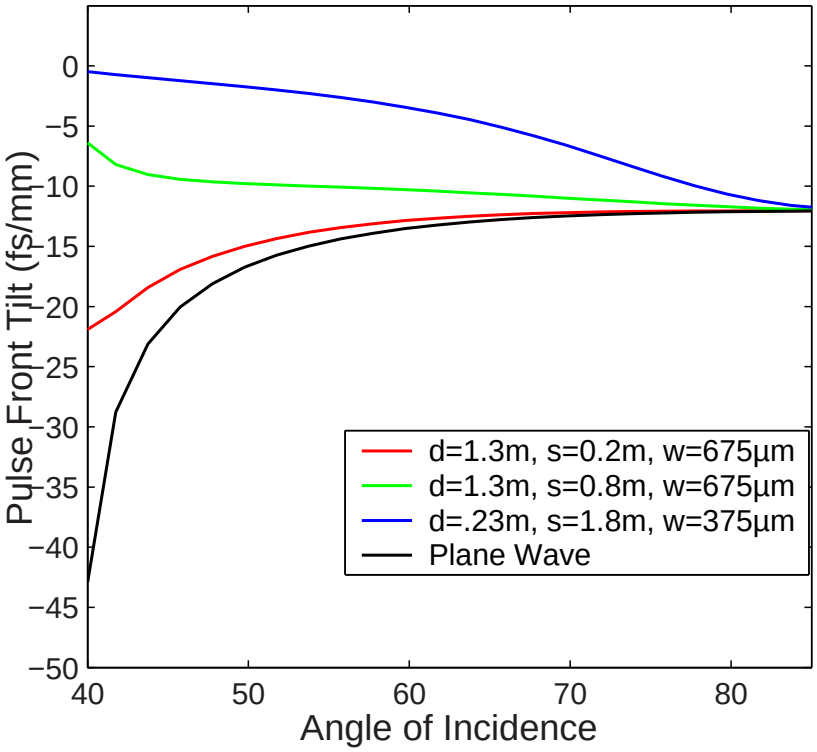

Figure 21: Theoretical dependence of the pulse-front tilt on angle of incidence for plane waves (blue curve) and Gaussian beams (other colored curves).

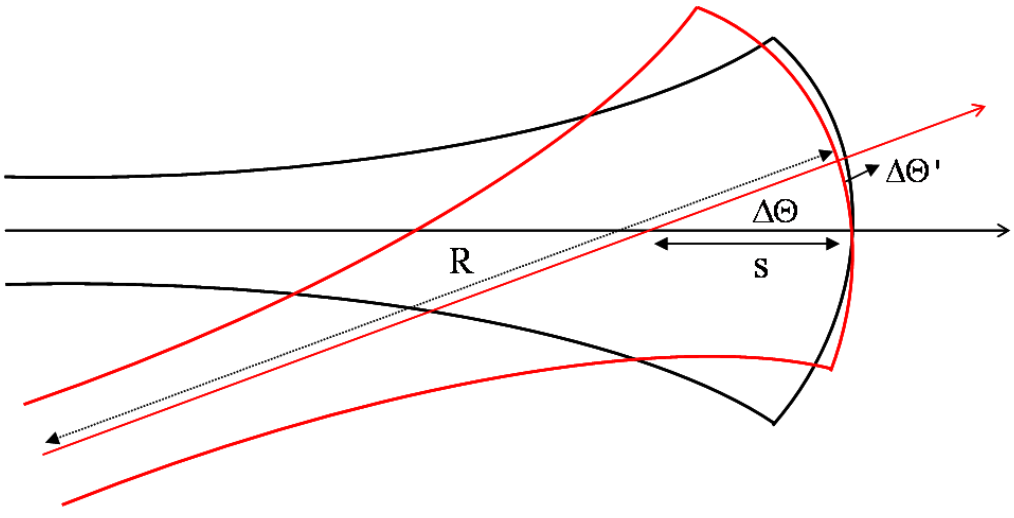

Figure 22: The subtlety in the definition of angular dispersion as explained in [89].

observation point; w is the beam width and z_R is the Rayleigh range.

In our experiments, due to small beam size and long propagation distances, the divergence of the beam could not be neglected. Therefore, for all of the theoretical plots in this work, it was necessary to take into account the Gaussian behavior of the beam and its effects on the pulse-front tilt, as shown in equation 40. We used 4×4 ray-pulse matrix approach developed by [46] to find the theoretical results. For the sake of brevity, we omit our detailed calculations of the pulse-front tilt in our experiments, which included the change in pulse-front tilt with propagation, and which essentially mirrors that found in [89, 55, 46].

In our measurements, we used a GRENOUILLE device supplied by Swamp Optics, which incorporated a 168^0-apex-angle Fresnel biprism, various lenses, and $3 - mm$ thick BBO crystal. The calibration was as follows; for a 256×240 array, delay axis was $7.12 fs/pix$, and wavelength axis was $0.139 nm/pix$.

Figure 23 shows measured GRENOUILLE traces for pulses with various amounts of pulse-front tilt, generated using our modified pulse-compressor (with a high resolution rotation stage under one of the four prisms). Note the significant variation of the displacement of the trace along the delay axis as the pulse-front tilt varies, as predicted by our theory. Note also the traces also possess shear, due to spatial chirp (part of spatial chirp is of course due to angular dispersion), but as we have shown in our previous note [5] and this one, effects of pulse-front tilt and spatial chirp on GRENOUILLE traces affect the GRENOUILLE trace in independent ways and so are easily both measured simultaneously. Therefore, existence of spatial chirp in the trace does not affect pulse-front tilt measurements.

Figure 24 shows a comparison of the measured pulse-front tilt using GRENOUILLE the theoretical pulse-front tilt for a pulse emerging from our modified pulse compressor, plotted as a function of the prism angle of incidence. There is very good agreement between the two curves. Note also that, GRENOUILLE easily measures even small amounts of pulse-front tilt, such as occurs when the prism angle is at angle of minimum deviation, and zero pulse-front tilt is obtained, which corresponds to the case of the pulse-compressor being considered to be "aligned."

Figure 25, on the other hand, shows an analogous plot that we obtained by using a

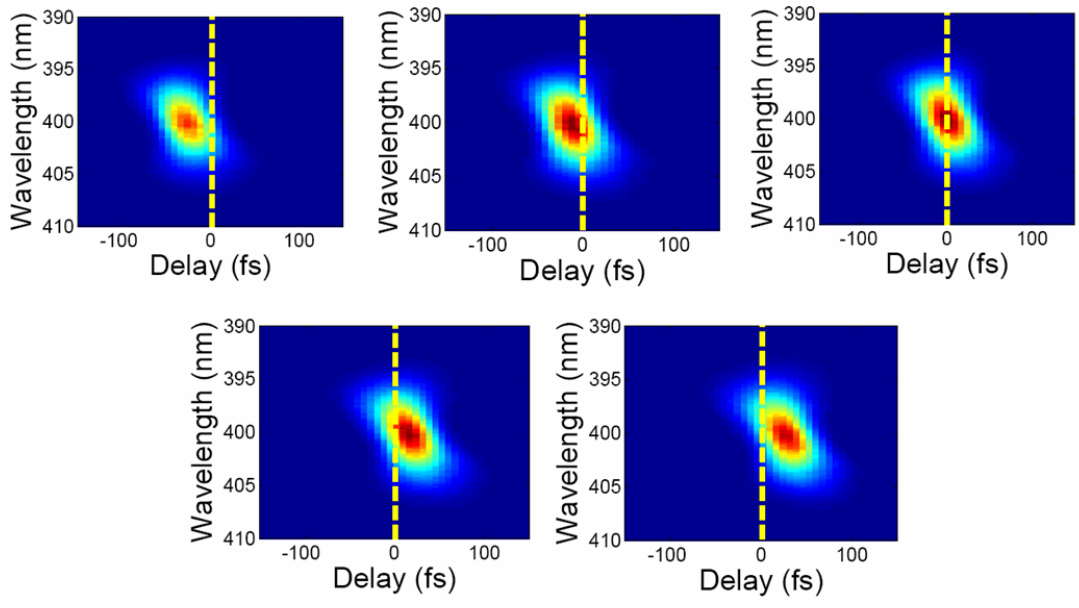

Figure 23: Measured GRENOUILLE traces for pulses with very negative, slightly negative, zero, and slightly positive, and very positive pulse-front tilt.

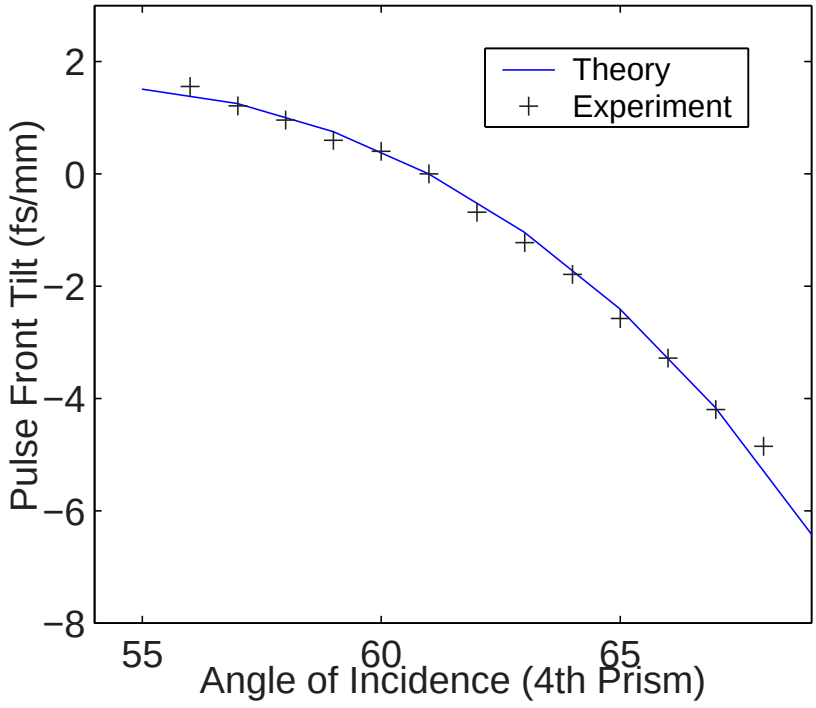

Figure 24: Theoretically predicted pulse-front tilt and the experimentally measured pulse-front tilt using GRENOUILLE.

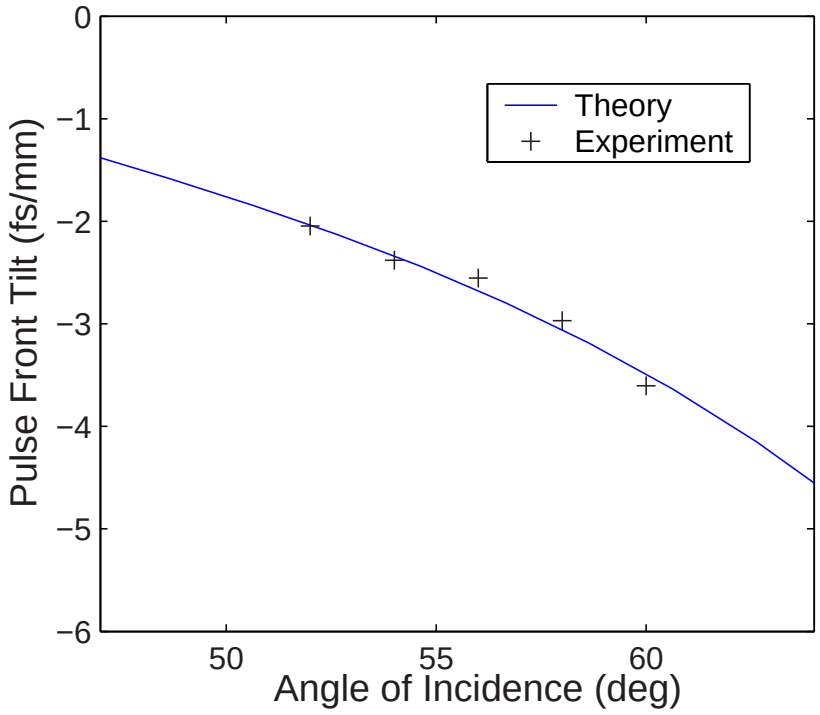

Figure 25: Measured and theoretically predicted pulse-front tilt generated with a single fused silica prism.

single 69^0 apex angle, fused-silica prism (Pulse-front tilt is always negative in this case). We again, have good agreement between the GRENOUILLE measurements and the theory. GRENOUILLE can measure pulse-front tilt with high sensitivity. Using a Gaussian fitting to the intensity profile of the trace to find the center, we obtained a sensitivity in the measurement of pulse-front tilt of $0.05 fs/mm$, which corresponds to a sensitivity in the measurement of angular dispersion of $0.12 \mu rad/nm$. This sensitivity is even better than that reported using spectrally resolved interference (SRI) [88] (the sensitivity was reported to be $0.2 \mu rad/nm$ in that note). However, SRI, in principle, measures arbitrary orders of pulse-front tilt, whereas GRENOUILLE can measure only the first order.

The fact that GRENOUILLE can measure pulse-front tilt with high sensitivity provides us the opportunity to align pulse compressors with a high sensitivity as well. We were able to align our prism pulse compressor with a sensitivity (in one prism angle of incidence) of 0.025 degrees. With such accuracy, this device should provide practical and reliable alignment of pulse compressors used in ultrafast laser laboratories.

3.5 Retrieval of pulse in the presence of pulse-front tilt

We also performed a preliminary test of our approach for determining the full spatio-temporal intensity and phase vs. time and position for a pulse with linear pulse-front tilt. Figure 26 shows the measured and retrieved GRENOUILLE traces for a pulse with pulse-front tilt, after the shift of the trace is taken out. The input pulse width was 123.5 fs FWHM. After the traces centered at zero delay (to remove pulse-front tilt) the pulse length is retrieved to be 125.1 fs FWHM. Notice the broadening of the pulse due to the narrower spectrum. The FROG error is 0.0038 (for a 128x128 array) for this measurement.

In conclusion, we have demonstrated that the experimentally simple version of single-shot SHG FROG, GRENOUILLE, measures, not only the pulse temporal intensity and phase and spatial chirp, but also the pulse-front tilt. The trace shift from the center of symmetry is directly proportional to pulse-front tilt. The GRENOUILLE trace determines the full spatio-temporal characteristics of a pulse with pulse-front tilt.

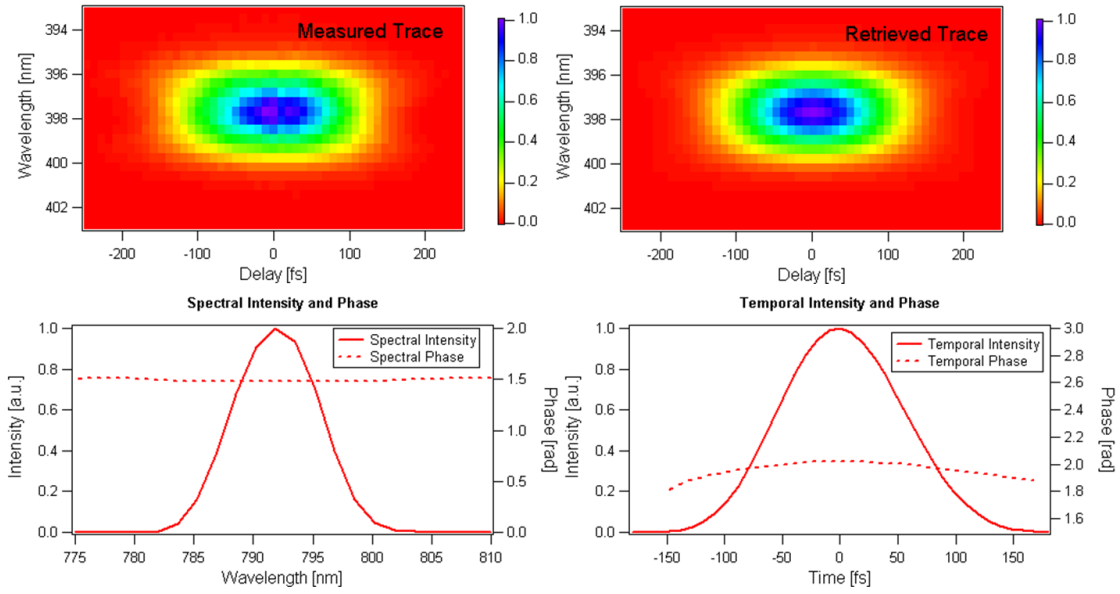

Figure 26: Measurement of the intensity and phase of a pulse with pulse-front tilt.

CHAPTER IV

PULSE-FRONT TILT CAUSED BY SPATIAL AND TEMPORAL CHIRP

This chapter originally appeared as a paper by the author:

Selcuk Akturk, Xun Gu, Erik Zeek and Rick Trebino, "Pulse-front tilt caused by spatial and temporal chirp", Optics Express 12, 4399-4410 (2003) [2]

4.1 Introduction

As explained in the previous chapters, space-time coupling or so called spatio-temporal distortions are very common in ultrafast optics because the generation, amplification, and manipulation of ultrashort pulses all involve the deliberate introduction and (only in principle) subsequent removal of them.

Angular dispersion is probably the most common space-time coupling effect because of frequent usage of dispersive elements like prisms and/or gratings. One important use of angular dispersion is spectral resolving as implemented in spectrometers. However, in ultrafast optics, angular dispersion is especially useful because it yields negative group-velocity dispersion [27, 31, 57], inherently opposite of normal material dispersion. Therefore, inverted prism and/or grating pairs act as pulse compressors/stretchers. Pulse compressors (Figure 11) are usually designed in such a way that at the output, all of the angular dispersion (and other spatio-temporal distortions) are compensated. Unfortunately, this requires very strict alignment. As a result, some residual angular dispersion remain usually in the output pulse, which translates to spatial chirp as worked out in detail in chapter 2.

Apart form spatial chirp, angular dispersion also yields another spatio-temporal distortion: pulse-front tilt (see Figure 27 left). In fact, it is generally thought that angular dispersion and pulse-front tilt are equivalent phenomena i.e. the presence/absence of one requires the presence/absence of the other. This was proved using geometrical ray-tracing

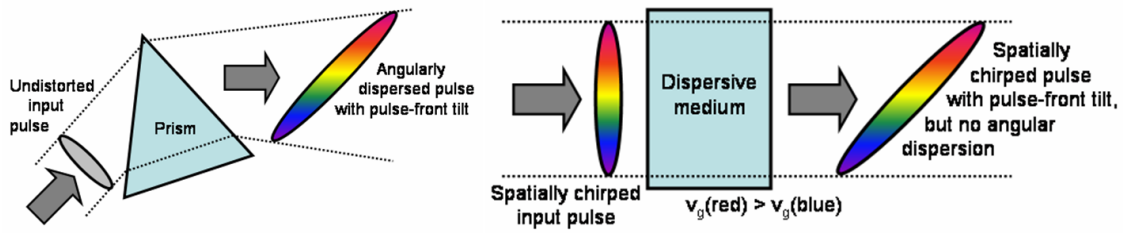

Figure 27: Two sources of pulse-front tilt. Left: The well-known angular dispersion. Right: The combination of spatial and temporal chirp.

by Bor et.al. [11] and Hebling [36], in which plane waves are always considered. Another more general proof using Fourier transform was given by Dorrer et.al. [25]. Specifically, a beam with pulse-front tilt can be written as:

$$E\left(x,z,t\right)=E_{xz}\left(x,z\right)E_{t}\left(t-px\right) \tag{41}$$

where p is the pulse-front tilt. We have suppressed the y-dependence and assumed that, apart from pulse-front tilt, $E\left(x,z,t\right)$ has no coupling of its coordinates, so it can be separated into $E_{xz}\left(x,z\right)$ and $E\left(t\right)$. (This is a more rigorous expression than that given in Ref. [25].) Simply Fourier-transforming from the $x-t$ domain to the $k-\omega$ domain and using two applications of the Shift Theorem, we have:

$$\hat{\tilde{E}}\left(k_{x},k_{z},\omega\right)=\hat{\tilde{E}}_{k_{x}k_{z}}\left(k_{x}-p\omega,k_{z}\right)\hat{\tilde{E}}_{\omega}\left(\omega\right) \tag{42}$$

which is a beam with angular dispersion. Specifically, $\mathrm{d}k_x/\mathrm{d}\omega = p$, or the angular dispersion is $\mathrm{d}\theta_0/\mathrm{d}\omega = p/k_0$, where θ_0 is the propagation angle, and k_0 is the nominal wave-number in vacuum.

While the above proof seems quite fundamental, we show in this work that angular dispersion and pulse-front tilt are not equivalent, and we provide an additional (and rather common!) source of pulse-front tilt, in which no angular dispersion occurs. We point out that the "proof" of angular dispersion/pulse-front tilt (AD/PFT) equivalence only holds for fields of the above form, and our counter-example incorporates a beam with spatial chirp, which cannot be written in the above form.

Specifically, to see how PFT can easily occur in the absence of AD, consider an initially transform-limited, but spatially chirped, finite-size beam-with no angular dispersion-passing

through a dispersive medium (see Figure 27, right). Due to the group-velocity dispersion in the medium, the redder side of the beam emerges from the medium earlier than the bluer side, resulting in PFT in the output beam. Because no angular dispersion exists, this obviously violates the well-known AD/PFT equivalence.

In the recent years, there have been several works that considered PFT and AD. Geometrical-optical modeling of AD in ultrashort pulses was performed using plane waves in [48]. Bor and Racz [10] showed that position-dependent delays of the pulse front occur at the output of a two-prism pulse compressor, but they did not note the violation of the AD/PFT equivalence. The most comprehensive work on spatio-temporal distortions with dispersive elements is that of Martinez [54], who considered PFT in an angularly dispersed beam with finite beam size. Martinez derived the modified expression of PFT in this case, but did not appear to realize that his finite-beam correction is indeed due to the combined effect of temporal chirp and spatial chirp (SC), both results of beam propagation with AD.

4.2 Angular dispersion and pulse-front tilt in the presence of spatial chirp

The linear optical elements that we need to consider (prisms, gratings etc.) here do not alter the spectral intensities of frequency components. They rather spatially manipulate each frequency. Therefore, it is best to model both of the effects in Figure 27 using an expression in the $x-\omega$ domain. For the electric field of a pulse with linear SC and AD, we can write:

$$E(x,\omega) = E(\omega)\exp\left[-\mathrm{i}\frac{k(x-\zeta\omega)^2}{2q}\right]\exp\left(-\mathrm{i}k_0\beta\omega x\right) \tag{43}$$

where k_0 is the nominal wave-number, ω is the offset from the center angular frequency, and q is the complex q parameter of a Gaussian beam:

$$q(z) = (z+d) + \mathrm{i}\frac{\pi w^2}{\lambda} = (z+d) + \mathrm{i}\frac{k_0 w^2}{2} \tag{44}$$

where d is the position of the beam waist and w is the spot size. The SC and AD are parameterized by $\zeta \equiv \frac{\mathrm{d}x_0}{\mathrm{d}\omega}$, and $\beta \equiv \frac{\mathrm{d}\theta_0}{\mathrm{d}\omega}$ respectively, where x_0 is the beam center position of the ω-component of the beam and θ_0 is the propagation angle of this component.

Throughout this work, we concentrate on spatio-temporal distortions in the x-direction only and therefore neglect the beam's y-dependence. Generalization to both x and y dependencies is straightforward.

We assume a Gaussian spectrum with linear chirp:

$$E(\omega) = E_0 \exp\left(-\frac{\omega^2\tau_0^2}{4}\right)\exp\left(-\mathrm{i}\frac{\varphi^{(2)}}{2}\omega^2\right) \tag{45}$$

where $\varphi^{(2)}$ is the second order spectral phase, often referred as "group delay dispersion", and τ_0^2 is the transform limited $HW1/e$ pulse width.

For a well collimated beam, we can write:

$$q(z) \approx q_0(d) = \mathrm{i}\frac{kw^2}{2} \tag{46}$$

Using these expressions, Eq. 43 becomes:

$$E(x,\omega) = E_0 \exp\left(-\frac{\omega^2\tau_0^2}{4}\right)\exp\left[-\frac{(x-\zeta\omega)^2}{w^2}\right]\exp\left(-\mathrm{i}\frac{\varphi^{(2)}}{2}\omega^2\right)\exp\left(-\mathrm{i}k_0\beta\omega x\right) \tag{47}$$

Here, we would like to point out, as shown in chapter 2, there are two related, but different, definitions of spatial chirp. We can either define spatial chirp as the spatial dispersion $\zeta \equiv \frac{\mathrm{d}x_0}{\mathrm{d}\omega}$, where x_0 is the beam center position of the ω-component, or equivalently define it as the frequency gradient $\upsilon \equiv \frac{\mathrm{d}\omega_0}{\mathrm{d}x}$, where ω_0 is the mean frequency at position x. These quantities are not reciprocals of each other, and the relationship between and for Gaussian pulses and beams is:

$$\upsilon = \frac{\zeta}{\zeta^2 + \frac{w^2\tau_0^2}{4}} \tag{48}$$

Using the frequency gradient υ , Eq. 47 may be rewritten as

$$E(x,\omega) = E_0 \exp\left[-\left(\frac{x}{w'}\right)^2\right]\exp\left[-\frac{(\tau')^2}{4}(\omega-\upsilon x)^2\right]\exp\left(-\mathrm{i}\frac{\varphi^{(2)}}{2}\omega^2\right)\exp\left(-\mathrm{i}k_0\beta\omega x\right) \tag{49}$$

where $w' = \left(\frac{1}{w^2} - \frac{\upsilon^2\tau_0^2}{4}\right)^{-\frac{1}{2}}$ is the overall beam width, increased from ω due to spatial chirp, $\tau' = \left(\tau_0^2 + \frac{4\zeta^2}{w^2}\right)^{\frac{1}{2}}$ is the local transform-limited pulse width, increased from τ_0 due to the reduced locally available bandwidth.

After some reorganizing,

$$\begin{aligned} E(x,\omega) = E_0 \exp\left[-\left(\tfrac{x}{w'}\right)^2\right] \exp\left[-\mathrm{i}\left(k_0\beta + \tfrac{\varphi^{(2)}}{2}\upsilon\right)\upsilon x^2\right] \\ \times \exp\left[-\tfrac{(\tau')^2}{4}(\omega - \upsilon x)^2\right] \exp\left[-\mathrm{i}\tfrac{\varphi^{(2)}}{2}(\omega - \upsilon x)^2\right] \\ \times \exp\left[-\mathrm{i}\left(k_0\beta + \varphi^{(2)}\upsilon\right) x(\omega - \upsilon x)\right] \end{aligned} \tag{50}$$

Various terms in equation 50 can be understood in terms of physical quantities. The first exponential is the usual Gaussian beam transverse (x) profile, with the spot size increased. The second exponential is a spatial phase term. The third exponential yields the position dependent spectrum. The Fourth exponential is the phase term proportional to ω^2, which is the chirp term. And finally the last expression is a phase term which is linear not only in frequency ω, but also in position x. The linear phase in w domain is nothing but a shift in time. The additional linear dependence to position dictates that the time of arrival depends on the position!. This is very important observation in the explanation of failure of the AD/PFT equivalence. This is explained below in more detail and more qualitatively.

The frequency dependence in Eq. 50 is familiar, namely a linearly chirped pulse, and can be easily inversely Fourier-transformed into the time domain:

$$E_0(x,t) = f(x) \exp\left[-\frac{(t-t_0)^2}{\tau^2}\right] \exp\left\{\mathrm{i}\left[\phi^{(1)}(t-t_0) + \frac{\phi^{(2)}}{2}(t-t_0)^2\right]\right\} \tag{51}$$

where:

$$f(x) = \frac{1}{\pi}\left[(\tau')^2 + \mathrm{i}2\varphi_2\right]^{-1/2} E_0 \exp\left[-\left(\frac{x}{w'}\right)^2\right] \exp\left(\mathrm{i}\frac{\varphi^{(2)}}{2}\upsilon^2 x^2\right) \tag{52}$$

$$t_0 = \left(k_0\beta + \varphi^{(2)}\upsilon\right) x \tag{53}$$

$$\tau = \left[(\tau')^2 + \frac{4\left(\varphi^{(2)}\right)^2}{(\tau')^2}\right]^{1/2} = \left[\tau_0^2 + \frac{4\zeta^2}{w^2} + \frac{4\left(\varphi^{(2)}\right)^2}{\tau_0^2 + \frac{4\zeta^2}{w^2}}\right]^{1/2} \tag{54}$$

$$\phi^{(1)} = \upsilon x \tag{55}$$

$$\phi^{(2)} = \frac{\varphi^{(2)}}{\frac{(\tau')^2}{4} + \left(\varphi^{(2)}\right)^2} = \frac{\varphi^{(2)}}{\frac{1}{4}\left(\tau_0^2 + \frac{4\zeta^2}{\sigma^2}\right)^2 + \left(\varphi^{(2)}\right)^2} \tag{56}$$

Even though it seems a bit complicated, equation 52 is easy to interpret. $f(x)$ gives the spatial evolution, which is not too much different than the regular Gaussian beams, with addition of a spatial phase term. Equation 54 gives the temporal pulse width, which is spread from the Fourier transform limited value, τ_0 due to two sources: spatial chirp and group delay dispersion. Equation 56 is the temporal chirp, which describes instantaneous frequency vs. time. And most important to our considerations, t_0 in equation 53 is the coupling between spatial coordinate x and time.

We identify t_0 as the pulse-front (maximum intensity contour) arrival time, and the PFT may be characterized by the derivative of t_0 with respect to x,

$$p \equiv \frac{\mathrm{d}t_0}{\mathrm{d}x} \tag{57}$$

The PFT angle -the angle between the pulse front and the propagation direction z- is then given by

$$\tan\psi = pc \tag{58}$$

From Eq. 53, it is easy to see that, for an ultrashort-pulse beam with Gaussian spectrum and Gaussian spatial profile, the PFT is

$$p = p_{\mathrm{AD}} + p_{\mathrm{SC+TC}} \tag{59}$$

where

$$p_{\mathrm{AD}} = k_0\beta \tag{60}$$

$$p_{\mathrm{SC+TC}} = \varphi^{(2)}\upsilon \tag{61}$$

This is the key result of this paper. PFT, in general, consists of two terms. The first term p_{AD} is the well known angular-dispersion term, as derived by Bor et al. [11] and Hebling [36]. The second term is a PFT effect caused by the combination of SC, which is characterized by the frequency gradient υ and temporal chirp, which is characterized by group-delay dispersion $\varphi^{(2)}$. This new PFT effect is clearly the cause of the PFT in the scenario shown in Figure 27 (right), in which no AD exists.

This additional source of PFT is not in violation of the proof in Section 1 that purports to show the equivalence of AD and PFT. Equations 41 42, after all, are simply an exercise

in Fourier transforms. Rather, the proof of equivalence is simply not sufficiently general because the forms of Eqs. 41 and 42 specifically preclude the presence of SC in the pulse. Fourier transforming Eq. 41 with respect to t yields a field in the $x-\omega$ domain of the form:

$$\tilde{E}(x,z,\omega) = E_{xz}(x,z)\,\tilde{E}_{\omega}(\omega)\exp(-\mathrm{i}px\omega) \tag{62}$$

But the presence of SC in the form of spatial dispersion requires an expression in the $x-\omega$ domain of the form:

$$\tilde{E}(x,z,\omega) = E_{xz}(x-\zeta\omega,z)\,\tilde{E}_{\omega}(\omega)\exp(-\mathrm{i}px\omega) \tag{63}$$

that is, some additional coupling of x and ω beyond the simple complex exponential. An example of this coupling is Eq. 43. The presence of SC in the form of frequency gradient requires an expression in the $x-\omega$ domain of the form:

$$\tilde{E}(x,z,\omega) = E_{xz}(x,z)\,\tilde{E}_{\omega}(\omega-\upsilon x)\exp(-\mathrm{i}px\omega) \tag{64}$$

Again, this requires coupling of x and ω beyond the simple complex exponential of Eq. 62. In other words, the derivation of AD/PFT equivalence given in [25] specifically suppresses the presence of spatial chirp, and is therefore nor general.

It is also important to note that these two sources of PFT have subtle physical effects on the pulse, beyond simply tilting the pulse front. AD causes different frequency components to propagate at different angles, resulting in tilt of both the pulse fronts (contours of equal intensity) and the phase fronts (contours of equal phase). On the other hand, simultaneous spatial and temporal chirp tilts the pulse front, while leaving phase fronts of constituent frequencies untilted. This point is very important in the measurement of the two effects. Also, some techniques purport to measure PFT, but in fact measure AD, and vice versa.

4.3 Propagation of ultrashort-pulse beams with angular dispersion and spatial chirp

Eqs. 50 and 51 give the expressions of the electric field in frequency and time domains at a particular longitudinal position z_0. In this section, we propagate the field to an arbitrary

position z, and discuss how the spatial-temporal coupling parameters, including SC and PFT, evolve. To accomplish this, we use the Fresnel-Kirchoff integral formula [37, 12, 78, 76]:

$$E(x,\omega,z)=\frac{\mathrm{i}}{\lambda z}\int_{-\infty}^{\infty}E(x',\omega,z=0)\exp\left[-\frac{\mathrm{i}\pi}{\lambda z}(x-x')^2\right]\mathrm{d}x' \tag{65}$$

We start from an initial field at $z_0=0$,

$$\begin{aligned}E(x,\omega,z=0)&=E(\omega,z=0)\exp\left[-\mathrm{i}\tfrac{k_0(x-\zeta_0\omega)^2}{2q_0}\right]\exp\left(-\mathrm{i}k_0\beta\omega x\right)\\&=E_0\exp\left(-\tfrac{\omega^2\tau_0^2}{4}\right)\exp\left(-\mathrm{i}\tfrac{\varphi_0^{(2)}}{2}\omega^2\right)\exp\left[-\mathrm{i}\tfrac{k_0(x-\zeta_0\omega)^2}{2q_0}\right]\exp\left(-\mathrm{i}k_0\beta\omega x\right)\end{aligned} \tag{66}$$

Substituting Eq. 66 in Eq. 65, we obtain:

$$\begin{aligned}E(x,\omega,z)&=\tfrac{\mathrm{i}k_0}{2\pi z}E_0\exp\left(-\tfrac{\omega^2\tau_0^2}{4}\right)\exp\left(-\mathrm{i}\tfrac{\varphi_0^{(2)}}{2}\omega^2\right)\\&\times\int_{-\infty}^{\infty}\exp\left[-\mathrm{i}\tfrac{k_0(x')^2}{2q(0)}\right]\exp\left[-\mathrm{i}k_0\beta\omega\left(x'+\zeta_0\omega\right)\right]\exp\left[-\tfrac{\mathrm{i}k_0}{2z}\left(x'+\zeta_0\omega-x\right)^2\right]\mathrm{d}x'\\&=\left[\tfrac{\mathrm{i}k_0}{2\pi z}\tfrac{q(0)}{q(z)}\right]^{1/2}E_0\exp\left(-\tfrac{\omega^2\tau_0^2}{4}\right)\exp\left(-\mathrm{i}\tfrac{\varphi_0^{(2)}}{2}\omega^2\right)\\&\times\exp\left\{\mathrm{i}\tfrac{k_0z}{2}\tfrac{q(0)}{q(z)}\left(\tfrac{x-\zeta_0\omega}{z}-\beta\omega\right)^2-\mathrm{i}k_0\left[\beta\zeta_0\omega^2+\tfrac{(x-\zeta_0\omega)^2}{2z}\right]\right\}\end{aligned} \tag{67}$$

For a well collimated beam, we can write:

$$\frac{q(0)}{q(z)}=\frac{d+\mathrm{i}\frac{k_0w^2}{2}}{z+d+\mathrm{i}\frac{k_0w^2}{2}}=1+\mathrm{i}\frac{2z}{k_0w^2} \tag{68}$$

Eq. 67 then simplifies to:

$$\begin{aligned}E(x,\omega,z)=\left(\tfrac{\mathrm{i}k_0}{2\pi z}\right)^{1/2}\left(1+\mathrm{i}\tfrac{2z}{k_0w^2}\right)^{1/2}E_0\exp\left(-\tfrac{\omega^2\tau_0^2}{4}\right)\exp\left[-\tfrac{\mathrm{i}}{2}\left(\varphi_0^{(2)}-k_0\beta^2z\right)\omega^2\right]\\\times\exp\left\{-\tfrac{\left[x-(\zeta_0+\beta z)\omega\right]^2}{w^2}\right\}\exp\left(-\mathrm{i}k_0\beta\omega x\right)\end{aligned} \tag{69}$$

Note that this is exactly in the form of Eq. 47, with the spatial dispersion and group-delay dispersion parameters substituted by the z-evolved values:

$$\zeta(z)=\zeta_0+\beta z \tag{70}$$

$$\varphi^{(2)}(z)=\varphi_0^{(2)}-k_0\beta^2z \tag{71}$$

The physical meanings of these results are obvious. Eq. 70 describes the increase of spatial dispersion with propagation due to AD. As the pulse propagates, different colors in the pulse become increasingly separated from each other. Eq. 71 describes the introduction of negative group-delay dispersion (GDD) due to AD, which is the theoretical basis of

pulse compressors. Using the evolved values of spatial dispersion and GDD, the results in the previous section can applied to obtain the evolution of other spatial-temporal coupling parameters, including frequency gradient and PFT:

$$\upsilon(z) = \frac{\zeta_0 + \beta z}{(\zeta_0 + \beta z)^2 + \frac{w^2 \tau_0^2}{4}} \tag{72}$$

$$p = k_0 \beta + \left(\varphi_0^{(2)} - k_0 \beta^2 z\right) \upsilon(z) \tag{73}$$

The generalized theory of spatio-temporal coupling in ultrashort-pulse beams can also be derived analogously using the matrix formalism introduced by A. G. Kostenbauder [46]. This is described in the last section of this chapter.

4.4 Experiment

In the previous sections, we showed that simultaneous spatial and temporal chirp cause PFT, even in the absence of AD. In this section, we describe an experimental demonstration of these theoretical results. Our experimental setup is shown in Figure 28. We used a prism pair to introduce SC in the beam. Identical Brewster prisms aligned anti-parallel were used to ensure that angular dispersion was eliminated after the second prism (as will be explained later, this does not put a critical alignment condition on our setup. Residual angular dispersion does not affect the result and can easily be detected). The beam then entered an imaging spectrometer with the direction of the spatial chirp along the entrance slit. A CCD camera on the exit plane of the spectrometer measured the spatio-spectral intensity profile of the beam. From this trace, we could either measure the slope of the beam center position vs. frequency, which yields the spatial dispersion ζ, or the slope of the center frequency vs. position, which yields the frequency gradient υ. The same beam was also sent to a Swamp Optics GRENOUILLE [87, 65], which measured both the GDD and the PFT with high sensitivity [4]. (GRENOUILLE also reveals SC as explained in chapter 2 [5], but a spatially resolved high-resolution spectrometer measurement has higher sensitivity for SC.) Other sensitive methods of measuring PFT have also been demonstrated [88, 89] but they in fact measure AD. As a result, they could not be used for our purposes.

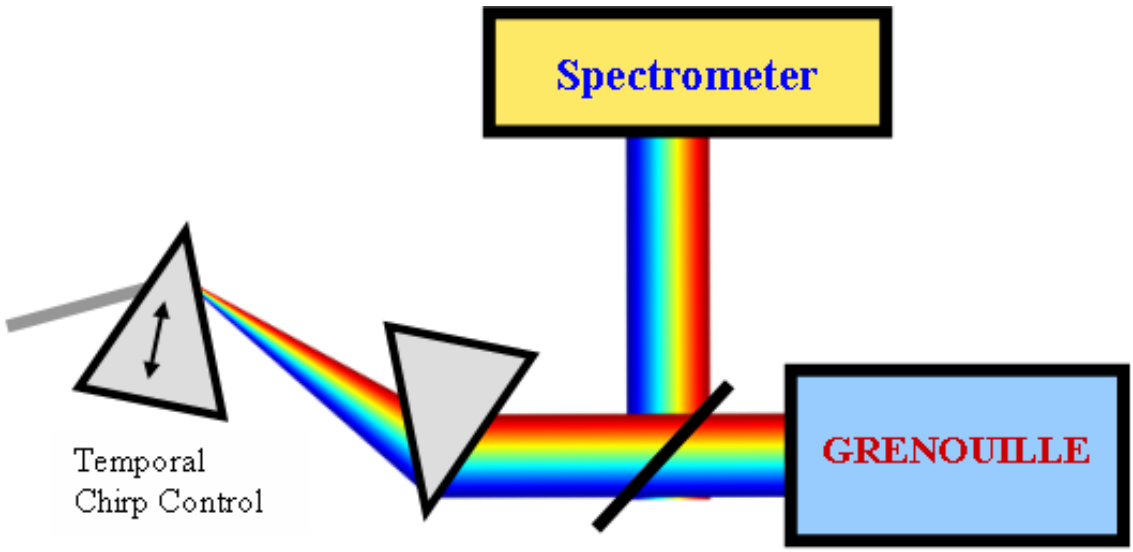

Figure 28: Apparatus to introduce constant spatial chirp, variable temporal chirp and no angular dispersion.

Interferometric techniques can also be used to measure PFT [25, 69] but we did not prefer them due to their experimental complexity.

In short, our setup (see Figure 28) introduced constant SC with no AD. Translating one of the prisms in and out of the beam adjusted the temporal chirp in the usual manner.

GRENOUILLE measures the PFT as a shift of the center of the trace along the delay axis [4]. Therefore, by translating the prism in and out of the beam (adding and removing material and hence adjusting the temporal chirp of the output beam), we expect to see a change in the shift of the center of the trace. Figure 29 shows some of the experimental GRENOUILLE traces for different values of temporal chirp. These traces clearly show that, although no AD is present, the beam possesses a significant amount of PFT that results from spatial and temporal chirp. This qualitatively demonstrates our theory.

More quantitatively, Eq. 55 shows that the slope of PFT p vs. GDD $\varphi^{(2)}$ yields the frequency gradient v. Figure 30 shows such a plot. We measured the slope of this plot to be $8.78 \times 10^{-3}(rad \times fs^{-1})/mm)$. The value of the frequency gradient measured by the spectrometer is $8.87 \times 10^{-3}(rad \times fs^{-1})/mm)$, $(\frac{\mathrm{d}\lambda_0}{\mathrm{d}x} = 3.01nm/mm)$ in excellent agreement with the other measurement.

As we proposed earlier, residual AD does not affect these results. If there is some

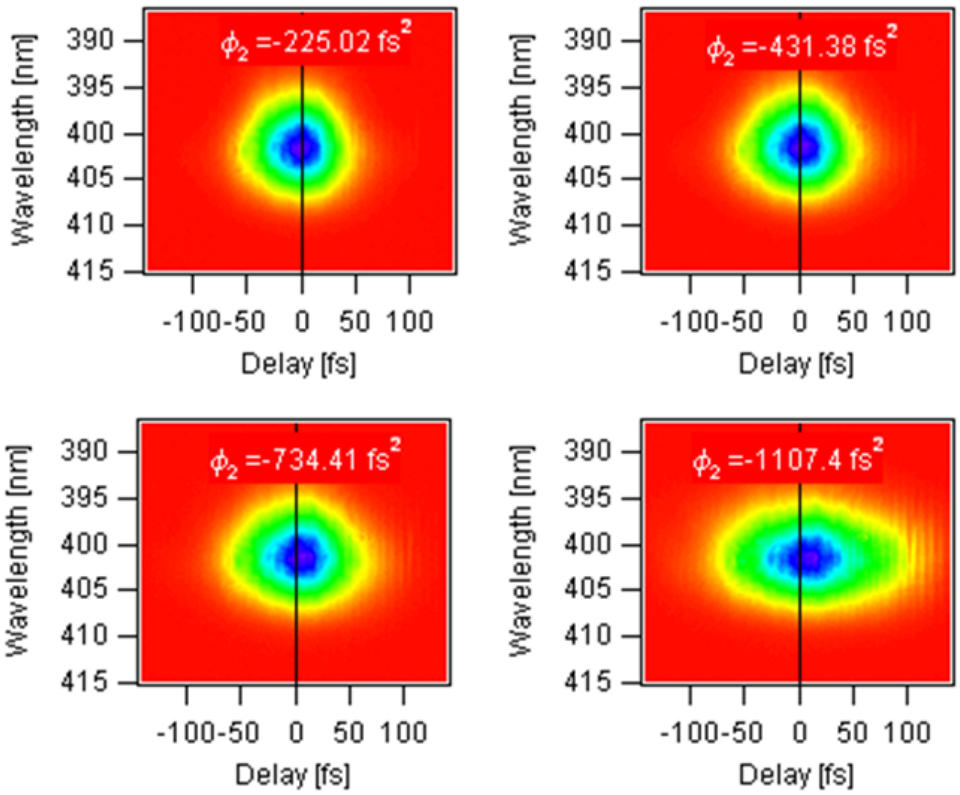

Figure 29: GRENOUILLE traces of a beam that has a constant spatial chirp and variable temporal chirp.

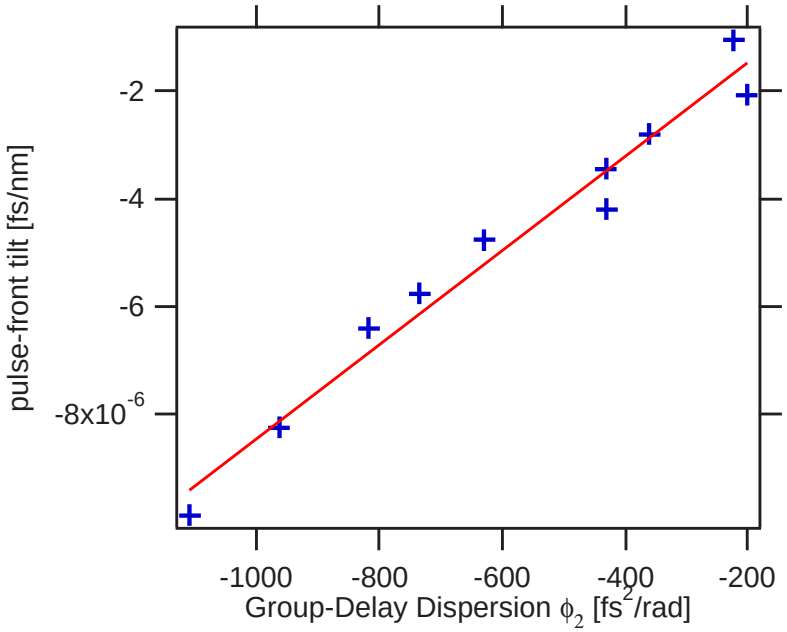

Figure 30: Experimental measurements (plus-sign symbols) of pulse-front tilt for different amounts of GDD. The red line shows the linear fit.

residual AD (from whatever source) in the beam that goes in the GRENOUILLE (Figure 28, then this would cause some additional PFT. However, this contribution to PFT does not vary with temporal chirp. Therefore, the only effect of this will be an offset of zero point PFT in the plot of Figure 30. The slope will not change. The amount of the offset can also be used to evaluate PFT that results from AD.

4.5 Matrix approach to show pulse-front tilt from simultaneous spatial and temporal chirp

We have shown above that simultaneous temporal and spatial chirp causes PFT even in the absence of angular dispersion. Here, we provide an alternative derivation using the matrix formalism introduced by Martinez [55, 56] and extended by Kostenbauder [46].

Even though the wave optical analysis that we used earlier in this chapter is sufficient to prove our results, the matrix method has some advantages over it. The most significant advantage of using matrix approach is that, each element in a complicated setup can be associated to a matrix. The matrix for the whole system will be simply the product of the individual matrices in the correct order. The spatio-temporal distortions can easily be seen form this single matrix.

2×2 matrices (commonly referred as $ABCD$ Matrices) have been used for many years [37] for ray optical analysis of complex optical systems, like laser cavities [78] . These matrices model the variations on the ray position (from the optical axis) and angle (deflection from the optical axis) caused by linear optical elements. To apply this method to femtosecond optics, however, some modifications are needed. Martinez [55] introduced 3×3 matrices to take into account the frequency dependence. Kostenbauder [46] generalized this method further by including the time dependence, resulting in 4×4 matrices for the linear optical elements.

Specifically, an optical system that introduces spatial and temporal chirp can be described in terms of a 4×4 ray-pulse matrix as:

$$K = \begin{bmatrix} A & B & 0 & E \\ C & D & 0 & F \\ G & H & 1 & I \\ 0 & 0 & 0 & 1 \end{bmatrix} = \begin{bmatrix} 1 & L & 0 & 2\pi\zeta \\ 0 & 1 & 0 & 0 \\ 0 & -2\pi\zeta/\lambda_0 & 1 & 2\pi\varphi^{(2)} \\ 0 & 0 & 0 & 1 \end{bmatrix} \tag{74}$$

where ζ is spatial dispersion and $\varphi^{(2)}$ is the GDD.

Matrix K can be obtained either by calculating the system ray-pulse matrix for a two-prism pulse compressor separated by L or for a fictitious system that introduces only spatial chirp followed by a dispersive slab of thickness nL (where $n = n(\omega)$ is the index of refraction). In both cases, GDD is the total GDD due to both the material and angular dispersions. Note that this approach describes only rays or plane waves (which has the form given in Eqs. 41 and 41), so the matrix shows no pulse-front tilt ($K_{31} = \frac{\partial t}{\partial x} = 0$), as we expect.

In order to apply the ray-pulse matrix to a finite-size Gaussian beam, we must use the complex Q matrix, as illustrated by Kostenbauder in Ref. [46]. Using this approach, the spatio-temporal electric field is expressed as:

$$E(x,t) = \exp\left\{-\mathrm{i}\tfrac{\pi}{\lambda_0}\begin{pmatrix} x \\ -t \end{pmatrix}^T Q^{-1} \begin{pmatrix} x \\ t \end{pmatrix}\right\} = \tag{75}$$
$$\exp\left[-\mathrm{i}\tfrac{\pi}{\lambda_0}\left(\left(Q^{-1}\right)_{11} x^2 + \left(Q^{-1}\right)_{12} xt - \left(Q^{-1}\right)_{21} xt - \left(Q^{-1}\right)_{22} t^2\right)\right]$$

The off-diagonal elements of the matrix Q^{-1} indicate spatial-temporal coupling. If we write the magnitude of electric field in terms of the local pulse length and the pulse-front tilt as:

$$|E(x,t)| \propto \exp\left[-\frac{(t-px)^2}{\tau^2}\right] \tag{76}$$

Equating the magnitude of equations 75 and 76 yields

$$\tau = \left[\frac{\pi}{\lambda_0}\mathrm{Im}\left\{\left(Q^{-1}\right)_{22}\right\}\right]^{-\frac{1}{2}} \tag{77}$$

$$p = \frac{\pi\tau^2}{2\lambda_0}\mathrm{Im}\left\{\left(Q^{-1}\right)_{12} - \left(Q^{-1}\right)_{21}\right\} = \frac{\mathrm{Im}\left\{\left(Q^{-1}\right)_{12} - \left(Q^{-1}\right)_{21}\right\}}{2\mathrm{Im}\left\{\left(Q^{-1}\right)_{22}\right\}} \tag{78}$$

For an input pulse with no spatio-temporal distortions and flat phase, we have

$$\left(Q_{\text{in}}^{-1}\right)_{11} = \frac{1}{q} \tag{79}$$

$$\left(Q_{\text{in}}^{-1}\right)_{22} = \mathrm{i}\frac{\lambda_0}{\pi\tau_0^2} \tag{80}$$

Then the input Q matrix is:

$$Q_{\text{in}} = \begin{bmatrix} q & 0 \\ 0 & -\mathrm{i}\frac{\pi\tau_0^2}{\lambda_0} \end{bmatrix} \tag{81}$$

The output Q matrix is found by:

$$Q_{\text{out}} = \left\{ \begin{bmatrix} A & 0 \\ G & 1 \end{bmatrix} Q_{\text{in}} + \begin{bmatrix} B & E/\lambda_0 \\ H & I/\lambda_0 \end{bmatrix} \right\} \cdot \left\{ \begin{bmatrix} C & 0 \\ 0 & 1 \end{bmatrix} Q_{\text{in}} + \begin{bmatrix} D & F/\lambda_0 \\ 0 & 1 \end{bmatrix} \right\}^{-1} \tag{82}$$

Substituting the elements of K from Eq. 74 into 82, we obtain:

$$Q_{\text{out}} = \begin{bmatrix} q+L & \frac{2\pi\zeta}{\lambda_0} \\ -\frac{2\pi\zeta}{\lambda_0} & \frac{2\pi\varphi^{(2)}}{\lambda_0} - \mathrm{i}\frac{\pi\tau_0^2}{\lambda_0} \end{bmatrix} \tag{83}$$

Inverting this matrix yields:

$$Q_{\text{out}}^{-1} = \begin{bmatrix} \frac{\lambda_0\left(\varphi^{(2)} - \frac{\mathrm{i}}{2}\tau_0^2\right)}{\varphi^{(2)}(L+q)\lambda_0 + 2\pi\zeta^2 - \frac{\mathrm{i}}{2}(L+q)\lambda_0\tau_0^2} & -\frac{\lambda_0\zeta}{\varphi^{(2)}(L+q)\lambda_0 + 2\pi\zeta^2 - \frac{\mathrm{i}}{2}(L+q)\lambda_0\tau_0^2} \\ \frac{\lambda_0\zeta}{\varphi^{(2)}(L+q)\lambda_0 + 2\pi\zeta^2 - \frac{\mathrm{i}}{2}(L+q)\lambda_0\tau_0^2} & \frac{1}{2\pi}\frac{(L+q)\lambda_0^2}{\varphi^{(2)}(L+q)\lambda_0 + 2\pi\zeta^2 - \frac{\mathrm{i}}{2}(L+q)\lambda_0\tau_0^2} \end{bmatrix} \tag{84}$$

For a well collimated beam, we can approximate:

$$q\left(L\right) = L + q \approx \mathrm{i}\frac{\pi w^2}{\lambda_0} \tag{85}$$

Therefore,

$$Q_{\text{out}}^{-1} = \begin{bmatrix} \frac{\lambda_0}{\pi}\frac{2\varphi^{(2)} - \mathrm{i}\tau_0^2}{4\zeta^2 + w^2\tau_0^2 + \mathrm{i}2\varphi^{(2)}w^2} & -\frac{2\lambda_0}{\pi}\frac{\zeta}{4\zeta^2 + w^2\tau_0^2 + \mathrm{i}2\varphi^{(2)}w^2} \\ \frac{2\lambda_0}{\pi}\frac{\zeta}{4\zeta^2 + w^2\tau_0^2 + \mathrm{i}2\varphi^{(2)}w^2} & \mathrm{i}\frac{\lambda_0}{\pi}\frac{w^2}{4\zeta^2 + w^2\tau_0^2 + \mathrm{i}2\varphi^{(2)}w^2} \end{bmatrix} \tag{86}$$

Using Eqs. (77) and (78), we find

$$\tau = \left[\tau_0^2 + \frac{4\zeta^2}{w^2} + \frac{4\left(\varphi^{(2)}\right)^2}{\tau_0^2 + \frac{4\zeta^2}{w^2}}\right]^{1/2} \tag{87}$$

$$p = \frac{\varphi^{(2)}\zeta}{\zeta^2 + \frac{1}{4}w^2\tau_0^2} \tag{88}$$

where $p \equiv \frac{\mathrm{d}t_0}{\mathrm{d}x}$ is pulse front tilt. Note that these results are identical to the results we obtained using Fourier transforms.

In conclusion, we have shown that the equivalence of pulse-front tilt and angular dispersion is valid only for beams without spatial chirp. In the presence of spatial chirp, the combination of spatial and temporal chirp also causes pulse-front tilt. We have derived analytical expressions for ultrashort-pulse beams that possess angular dispersion, spatial chirp and temporal chirp. We verified our theoretical results experimentally using GRENOUILLE.

CHAPTER V

EXTREMELY SIMPLE DEVICE FOR MEASURING 20 FS PULSES

This chapter originally appeared as a paper by the author:

Selcuk Akturk, Mark Kimmel, Patrick O'Shea and Rick Trebino, "Extremely simple device for measuring 20-fs pulses", Optics Letters 29, 1025-1027 (2004) [6]

5.1 Introduction

Ultrafast lasers are generating ever shorter [8, 81, 9] pulses, ever more conveniently. Unfortunately, pulse-measurement devices, especially for $\sim$ 20 fs pulses and their large bandwidths, have remained complex, yielding the risk that the device could induce the very distortions it purports to measure. Moreover, the pulse temporal phase information is crucial in generating very short pulses as third and higher order phase seriously effect the shortest pulse width obtainable with a certain bandwidth [45]. Thus, it is very important to develop a simple, accurate, and convenient method for measuring such short pulses.

To date, the simplest device for accurately measuring the intensity and phase of ultrashort pulses is GRENOUILLE (GRating-Eliminated No-nonsense Observation of Ultrafast Incident Laser-Light E-fields)[65], an elegant variant of FROG (Frequency-Resolved Optical Gating)[87]. GRENOUILLE involves two innovations (see Figure 31). First it uses a Fresnel bi-prism to split the beam into two beams crossed in space and time in the crystal. Second it uses a thick crystal that phase-matches a small and different fraction of the pulse bandwidth for each output angle. This allows the crystal to operate, not only as an autocorrelating element, but also as a spectrometer. Thus, the Fresnel biprism replaces FROG's beam splitter and beam-combining optics, and the thick crystal replaces FROG's thin crystal and spectrometer, yielding a very simple, compact FROG device that requires almost no alignment. As worked out in detail in the past three chapters, GRENOUILLE

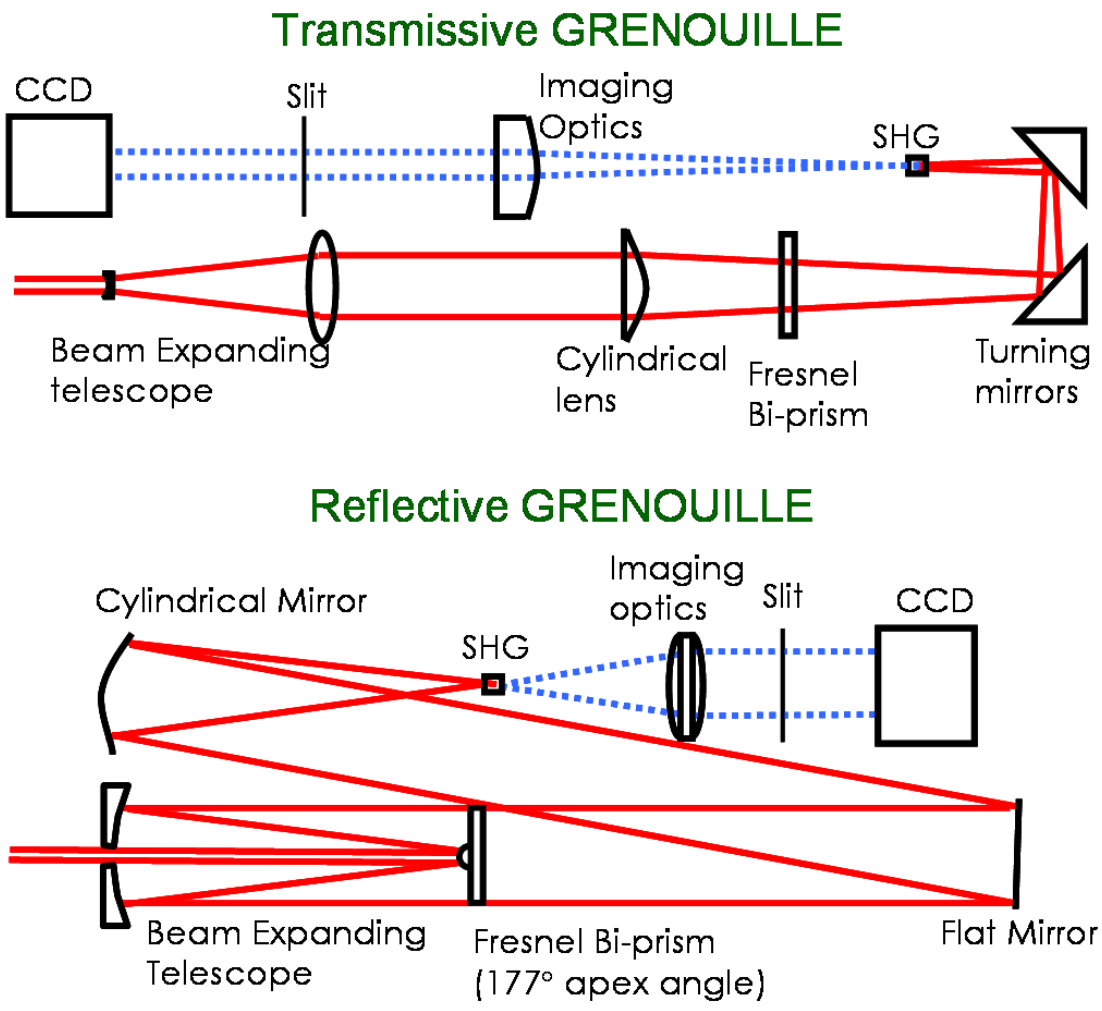

Figure 31: Compact GRENOUILLE geometries. Previous transmissive design for measuring pulses as short as 50 fs (top) and reflective design for measuring $\sim$ 20-fs pulses.

also measures the spatio-temporal distortions, spatial chirp and pulse-front tilt, without modification [5, 4].

However, previously reported implementations of GRENOUILLE could measure pulses only as short as $\sim$ 50 fs. One factor limiting its accurate measurement of shorter pulses is material dispersion in its transmissive optics, including the necessarily thick crystal. Another factor is that, in GRENOUILLE, the entire pulse spectrum must be phase-matched by the crystal for some beam angle. Because GRENOUILLE uses the crystal's phase-matched-wavelength-vs.-angle dependence to measure the pulse spectrum, a larger divergence angle (i.e., tighter focus) in the nonlinear crystal is required for broader-band pulses. The resulting

shorter confocal parameter of the beam then reduces the effective crystal length, reducing spectral resolution. In short, GRENOUILLE design is an over-constrained problem, and it is not clear that a solution exists for a given pulse-measurement problem, especially one involving a very short pulse.

5.2 Extending GRENOUILLE to shorter pulses

Fortunately, these problems can be solved using a tighter focused, nearly-all-reflective GRENOUILLE with a thinner crystal (but still thick by normal autocorrelator or FROG standards). Specifically, we replace all but one optic before the second-harmonic-generation (SHG) crystal with reflective components. The resulting device uses a (reflective) Cassegrain telescope [37], rather than the Keplerian telescope. This avoids dispersion (and chromatic aberrations), but the beam hole could conceivably introduce diffraction effects, biasing the measurement, which involves mapping delay onto position. However, after the Fresnel biprism, these effects occur at the outside edges of the crossed beams at the crystal, where they do minimal harm because the intensity is the least there. Furthermore, the beam is very large in the delay dimension to get a nearly flat region over which the pulse is being measured. These edges that see diffraction effects are usually well outside of the region of measurement.

Our design also uses a cylindrical focusing mirror. It uses only one transmissive optic, the Fresnel biprism, but the short pulses to be measured require only a small range of delays and hence a very small beam crossing angle ($\sim 1.5^0$). Thus, the biprism apex angle is so close to 180^0 (177^0) that it can be made extremely thin (ours is ~ 1.3 mm, but it could be even thinner), with a material that has very small dispersion (e.g. fused silica).

Finally, the "thick" crystal required to spectrally resolve (using small phase-matching bandwidth) a 20-fs pulse is also thinner: only 1.5 mm. As a result, with these modifications, material dispersion is negligible for even a sub-20-fs pulse.

On the other hand, the device must be able to measure pulses with bandwidths of ∼50 nm, so it should have ∼100 nm of bandwidth itself. While we showed previously that the wavelength range of GRENOUILLE can be extended by angle-dithering the input beam at

the crystal [66], this significantly complicates the setup and ceases the single-shot capability.

We find that simply focusing more tightly into the crystal achieves the required 100 nm spectral range. This, however, yields a shorter beam confocal parameter, decreasing the effective interaction length in the crystal and hence reducing the device spectral resolution. Fortunately, due to their broadband nature, shorter pulses require less spectral resolution. With these improvements, a GRENOUILLE can be made that is as simple and as elegant as the transmissive GRENOUILLE previously reported (Figure 31), but capable of accurately measuring much shorter pulses (20 fs).

GRENOUILLE obtains spectral resolution through phase-matching bandwidth, or equivalently through group-velocity mismatch (GVM)[65, 87]: the crystal interaction length (L) times the GVM must exceed the pulse length (τ_p):

$$L \times GVM \gg \tau_p \tag{89}$$

the opposite of the usual GVM (phase-matching) condition for other pulse measurement devices.

On the other hand, the crystal must not be so thick as to have significant group velocity dispersion. Since the shortest temporal component of the pulse is the coherence time (τ_c), we have:

$$L/2 \times GVD \ll \tau_c \tag{90}$$

Note that we have used L/2 here because the pulse contributes signal to the trace throughout the crystal, and L/2 corresponds to the position with the average pulse distortion.

These conditions become more difficult to satisfy as the pulse shortens and the GVD approaches the GVM. In fact, for a single-cycle pulse, for which $\tau_c sim \tau_p$ and GVD approaches the GVM, these conditions cannot be satisfied.

Fortunately, for not too complex 20 fs pulses, they can be satisfied, and, coupled with FROG's ability to see through systematic error (the trace over-determines the pulse[94]), results will be accurate. Figure 32 shows our device's operating range. In that plot, the solid line represents the (upper) limit set by the spectral resolution of the crystal, or GVM.

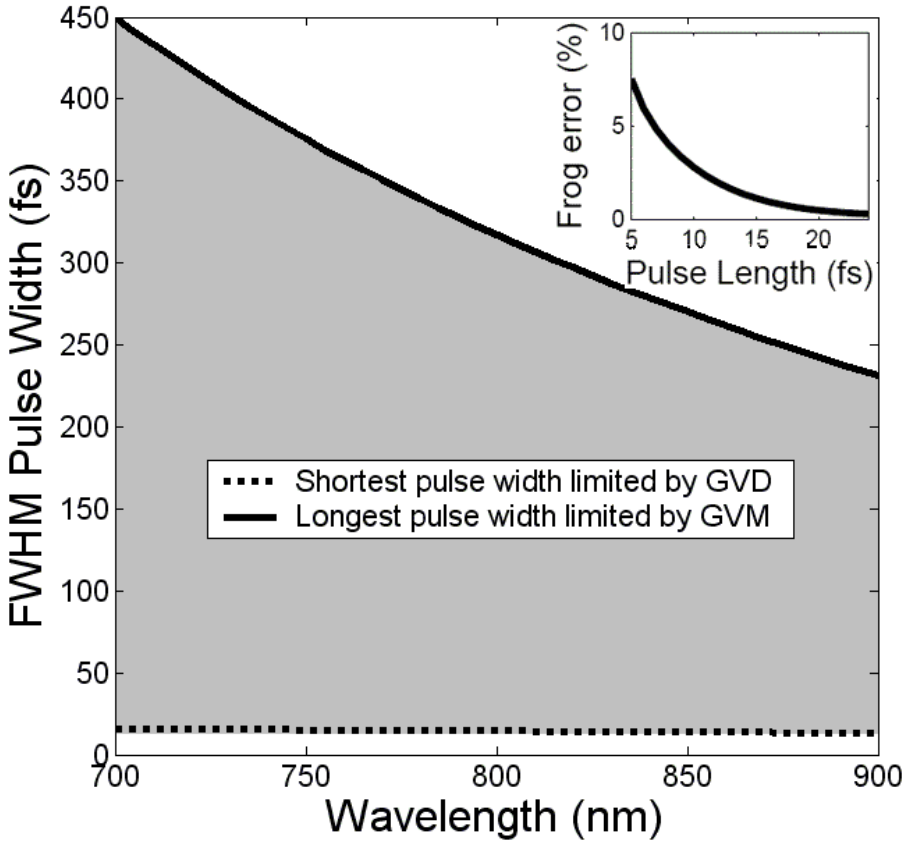

Figure 32: Pulses measurable using a GRENOUILLE with a 1.65 mm BBO crystal.

The dashed line represents the (lower) limit set by GVD induced by the crystal. Therefore, the device is operable in the shaded region only. The inset shows the theoretical FROG error vs. pulse width due to crystal dispersion. Note that the FROG error due to dispersion is negligibly small for $\sim 20fs$ pulses, while it peaks up for shorter ones.

Specifically, for 20-fs (47-nm bandwidth), 800-nm pulses in BBO, $GVM = 3.3 \times 103fs/cm$, and $GVD = 104fs/cm$. A crystal length of 1.65 mm yields $(L/2) \times GVD = 8.5fs$, and $L \times GVM = 539fs$. Since the last two numbers are conveniently away from each other, these values allow pulse measurements without preprocessing or modifications to the FROG algorithm (although this is possible). Our spectral resolution is 3.0 nm, which allows accurate measurement of longer pulses, too (Figure 32). The crystal GVD will broaden a transform-limited 20-fs pulse to at most 26.6 fs after the crystal, but the value at the center of the crystal, 21.7 fs, better assesses the device accuracy. Finally, a full beam divergence

angle of 4.4^0 in the crystal yields 120 nm of spectral range.

5.3 Experiment

A collimated beam entered the device and was expanded by the negative primary (R = 20 mm) (cemented to the back of the biprism) mirror of the Cassegrain telescope. The secondary mirror (R = 200 mm) recollimated the beam, and the biprism (apex angle 177^0) split it into two beamslets. The crossing beams were focused to overlapping line foci using a slightly off-axis cylindrical mirror (R = 200mm).

While a 3.5-mm BBO crystal was used, the focus was at the front of the crystal, and the effective crystal length (the length over which significant second harmonic light is generated) was considerably shorter (due to tight focusing): only $\sim$ 1.65 mm. Since most of the SHG occurred near the focus, the remaining crystal length was unused and irrelevant. It is worth mentioning here the method that we used to determine the effective crystal length; We determined the interaction length by placing in the beam a variable-spacing etalon to create a train of pulses with accompanying spectral fringes. We increased the etalon spacing, decreasing the spectral fringe spacing, until GRENOUILLE could no longer resolve these fringes. This resolution then yields the effective crystal length. Observe that this method is more practical than simply finding the Rayleigh range of the focused Gaussian beam.

The second harmonic then propagated to a 1/2" CCD camera, 100 mm away, using a pair of back-to-back plano-convex 50-mm-focal-length spherical and cylindrical lenses, halfway between the focus and the CCD. The effective focal length of the lens pair was 25 mm for the delay axis, resulting in 1-to-1 imaging in the relative-delay direction and a 1-fs/pixel delay resolution (480 pixels, using a Data Translation DT 3120 capture card). In the wavelength direction, the effective focal length of 50 mm mapped angle (i.e., wavelength) to position in the usual $f - f - f$ geometry [37]. The result was an SHG FROG trace at the camera.

A KM Labs Ti:Sapphire oscillator operating with $\sim$ 60 nm (FWHM) of bandwidth and an external prism pulse compressor yielded $\sim$ 20-fs pulses, which we measured with a conventional multi-shot FROG and with our modified short-pulse GRENOUILLE. The

Femtosoft FROG code retrieved the intensity and phase for both measurements. Figure 33 shows measured and retrieved traces and the retrieved intensity and phase for both measurements, all in excellent agreement. The minor discrepancy is likely due to drift in the pulse between the measurements. The pulse that GRENOUILLE retrieved in these measurements is 19.73 fs FWHM-the shortest pulse ever measured with GRENOUILLE.

In order to test GRENOUILLE's ability to measure complex pulses, we placed a (23.8m) air-spaced etalon in the beam before the GRENOUILLE to create a multiple-pulse, which we measured with GRENOUILLE. Figure 34 shows the measured and retrieved GRENOUILLE traces and retrieved intensity and phase versus time. These measurements clearly show that GRENOUILLE is capable of revealing the fine structure in both frequency and delay. We also used these traces for calibration of both the delay and wavelength axes [100].

In conclusion, we have shown that, despite its simplicity, we can design a GRENOUILLE that can accurately measure pulses as short as 20 fs. We achieve this by eliminating most of the transmissive optics and carefully selecting the focusing and imaging optics. Furthermore, the geometry remains simple and compact and retains GRENOUILLE's ease of alignment, sensitivity, real-time operation, intuitive feedback, and ability to measure spatio-temporal distortions.

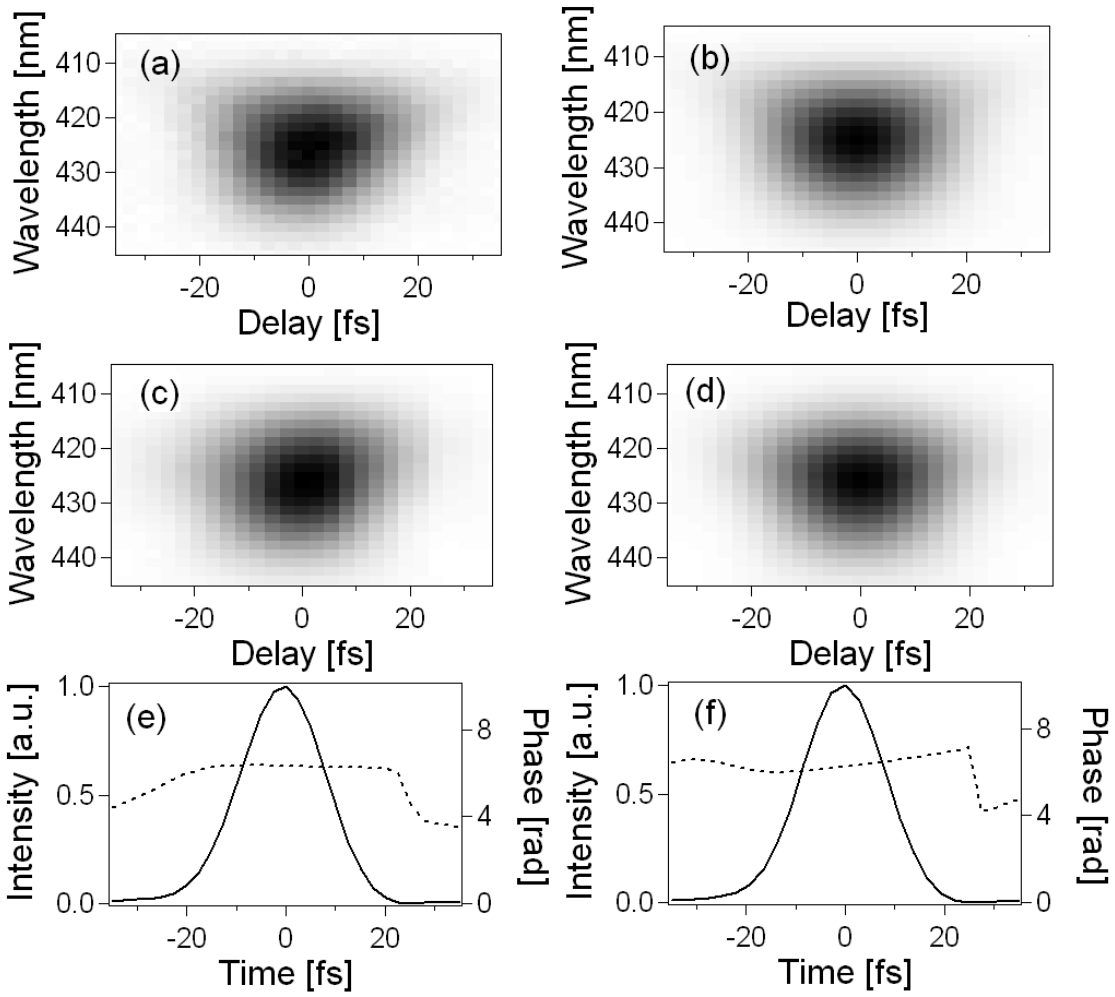

Figure 33: Comparisons of short-pulse GRENOUILLE and multi-shot FROG measurements. (a) measured GRENOUILLE trace; (b) measured multi-shot FROG trace; (c) retrieved GRENOUILLE trace (FROG error:0.00497); (d) retrieved multi-shot FROG trace (FROG error 0.00482); (e) retrieved intensity and phase vs. time for GRENOUILLE measurements (temporal pulse width 19.73 fs FWHM); (f) retrieved intensity and phase vs. time for multi-shot FROG measurements (temporal pulse width 19.41 fs FWHM)

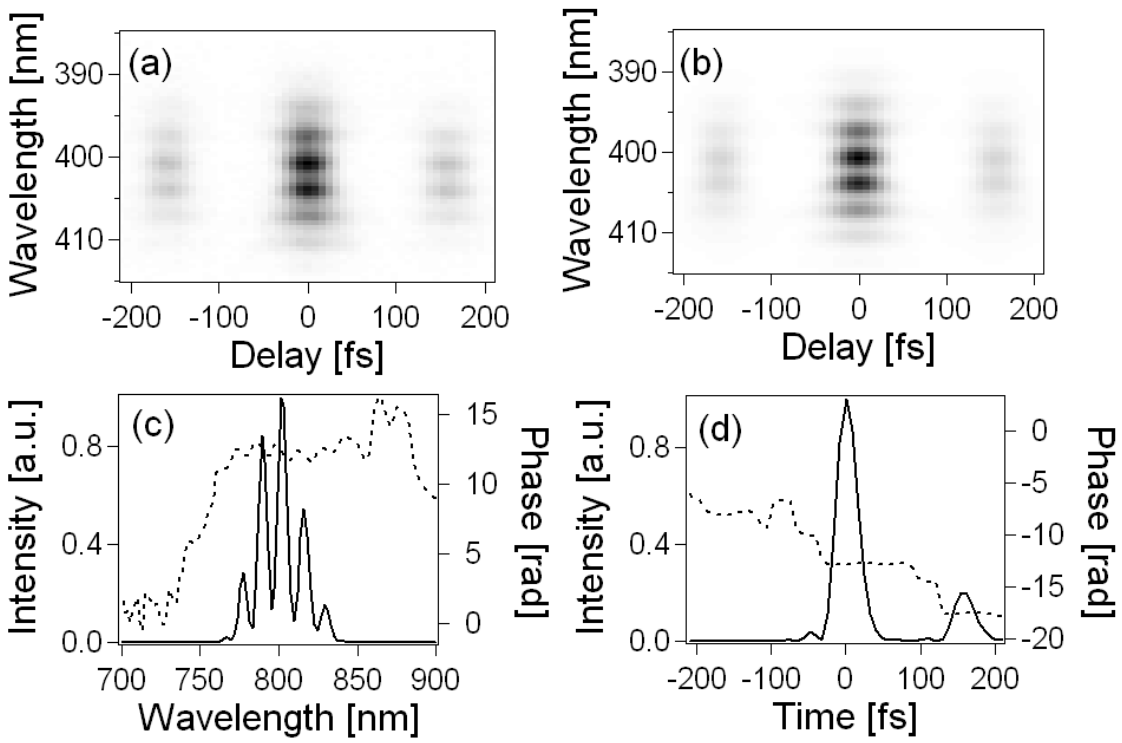

Figure 34: (a) Measured and (b) retrieved GRENOUILLE traces (FROG error 0.00643) for a double pulse. Note the characteristic fringed double-pulse trace. (c) spectrum and spectral phase and (d) intensity and phase versus time for a double pulse.

CHAPTER VI

PRACTICAL DEVICES FOR MEASURING EXTREMELY SHORT AND EXTREMELY LONG PULSES

6.1 Introduction

Devices for measuring ultrashort pulses are usually designed to measure pulses $\sim 100fs$ long. This is partly because $\sim 100fs$ is the most common pulse length in use, but also because serious challenges complicate the measurement of pulses that are much shorter-and also much longer. Recently, very short (few fs) [9] and relatively long (few ps) pulses have become popular for a variety of applications [22, 74], and commercial lasers that emit them are now common. Unfortunately, convenient and powerful pulse diagnostics haven't been available for them.

In general, measuring ultrashort pulses involves splitting the pulse in two, variably delaying one pulse with respect to the other, crossing them in a second-harmonic generation (SHG) crystal, and then measuring the SHG pulse energy or spectrum with respect to delay. Measuring the energy vs. delay is called autocorrelation, and it yields only a rough measure of the pulse length. Measuring the spectrum of the autocorrelation signal is better, yielding the complete pulse intensity and phase vs. time. The latter technique is called frequency-resolved optical gating (FROG) [87]. In this chapter, we present FROG geometries for measuring extremely short and extremely long pulses.

6.2 Measuring extremely short pulses

As with everything ultrafast, the main challenge in measuring extremely short pulses stems from bandwidth issues. First of all, the SHG process must have sufficient phase-matching bandwidth to generate the second harmonic for the entire bandwidth of the pulse to be measured. Unfortunately, in SHG, different wavelengths require different crystal phase-matching angles, but the pulse enters at only one angle. As a result, only one wavelength

achieves this ideal condition perfectly; others do so only approximately. The resulting SHG phase-matching bandwidth scales inversely with the crystal length, so SHG phase-matching bandwidth considerations necessitate extremely thin nonlinear crystals ($10\mu m$ is typical!) for very short pulses. Such thin crystals are difficult to manufacture and work with, and worse, they yield very poor device sensitivity because the SHG efficiency scales as the square of the crystal length.

Another issue that makes measuring extremely short pulses very difficult is group-velocity dispersion (GVD), the difference in material group velocities for wavelengths within the pulse. GVD broadens pulses and is present in every transmissive component of the device. Therefore, avoiding GVD means minimizing the amount of material the pulse passes through before and including the nonlinear crystal, which can be difficult when, for example, pulses must be split by a beam splitter (which is usually a glass substrate coated with dielectric layers) and focused.

Finally, the relative delay is usually varied by translating a mirror, and when the pulses are relatively large and crossed at an angle, the relative delay between the pulses can also vary transversely across the crystal or along it, causing a range of delays to be sampled, rather than just one at a time. This effect is called "geometrical smearing," and it causes the measured pulse length to be larger than the actual pulse length. Its effects are considerably more detrimental for very short pulses. It can usually be minimized by using a very small beam angle. But it is particularly deleterious when using a large beam and a large beam crossing angle, which, unfortunately, are both requirements of a convenient, easy-to-align device [87].

Additional inconvenient features have also complicated pulse-measurement devices. These include the need for collinear beams, which involves no less than five extremely sensitive alignment degrees of freedom, and high resolution translation stages that scan the delay over many pulses with their resulting slow data acquisition.

To measure extremely short pulses with sufficient bandwidth, rather than using extremely thin crystals, we actually deliberately use relatively thick crystals. This is because we discovered recently that the well-known, very restrictive SHG bandwidth condition,

which requires very thin crystals and which has been accepted without question for many years, can actually be relaxed. It is in fact not necessary to achieve sufficient SHG bandwidth on every pulse in the measurement; instead it's only necessary to do so when integrated over the entire measurement. In this regard, while our thick crystal has considerably less bandwidth than that of the pulse, we achieve sufficient bandwidth for the measurement, by angle-dithering it [64]. This achieves a bandwidth determined not by the crystal thickness, but by the dither-angle range, and as a result, we can use relatively thick, efficient, and convenient crystals. For example, with angle-dithering, a much thicker, $100 - \mu m$ thick, BBO crystal can easily be used to measure pulses as short as $10 fs$.

In addition, because the GVD condition is not as strict as the old overly restrictive phase-matching bandwidth condition, the relatively thick crystal does not introduce significant GVD. Indeed, to minimize GVD, mirrors can replace most reflective optics, and the beam splitter can be replaced with a split mirror, which introduces no GVD and allows a very simple and elegant setup.

To avoid geometrical smearing effects, we use very large (unfocused) beams, and we deliberately cross them at a large angle. This causes the relative delay to vary across the crystal by considerably more than the pulse length! But we take advantage of this effect, as the delay is now already varied, and there is now no need to translate a mirror. We then image the crystal onto a camera, where delay is now automatically mapped onto transverse position for every pulse. This was already implemented in single-shot FROG [43] (In this case, although the delay generation allows single shot operation, due to angle dithering, the overall measurement has to be averaged over many pulses). More importantly, because the variation in delay across the crystal is now spatially resolved, it no longer smears delay and hence yields zero transverse geometrical effects. Indeed, it can be shown that other potential geometrical smearing effects are also zero for such a geometry [87].

There are other convenient aspects to this short-pulse FROG. We have recently shown that the above single-shot FROG beam set up also measures the two most important pulse spatio-temporal distortions, spatial chirp and pulse-front tilt [5, 4]. In addition, it involves large beams crossing at a large angle and so is very simple and convenient. And because

the delay need not be scanned, a single camera trace yields the entire measurement, so real-time pulse measurements are straightforward.

Finally, the large spectral bandwidth of few-fs pulses allows us to build a very short-path-length spectrometer, which provides relatively low, but more than sufficient, spectral resolution.

With these approaches, we have built a simple real-time FROG device to measure pulses as short as $10fs$. As shown in Figure 35, the device is very simple, compact, and easy to use, with a trivial alignment procedure.

The experimental parameters were as follows (see Figure 35): A Cylindrical Cassegrain telescope ($10\times$ magnification) is used to expand the beam in one (delay) dimension. The large beam is then reflected off the bi-mirror, to split into two beamlets that cross at an angle on the SHG crystal. Very small ($\sim 1^0$) crossing angle is needed to achieve enough temporal resolution. Therefore, a long path-length is needed between the bi-mirror and the crystal. The beamlets are focused cylindrically (in the wavelength dimension) with a $R = 200mm$ mirror. We used $100\mu m$ thick BBO crystal, mounted on a EOPC SC-21 resonant scanner operating at $\sim 200Hz$ frequency and $\sim 10^0$ amplitude. The resulting second harmonic is then collimated with a lens (note that the material dispersion does not matter after the second harmonic signal is already generated) and sent to the spectrometer stage. In the specrometer stage, we used a $600grooves/mm$ grating. The stage is made even more compact by using some folding mirrors. Finally, the spectrally resolved signal is imaged to the CCD.

To test and calibrate the device, we use an air spaced etalon (the spacing is $23.8\mu m$), which generates structure in the pulse in both frequency and time. Figure 36 shows the measured and retrieved FROG traces and the pulse spectral and temporal intensity and phase. The measured and retrieved traces matches very well. Note that the spectrum covers over 100 nm bandwidth, as desired.

These measurements show that by angle dithering the SHG crystal and eliminating transmissive optics, a FROG device can be built to measure pulse that are as short as ~10 fs. The resulting device is not only accurate but also compact, robust and convenient.

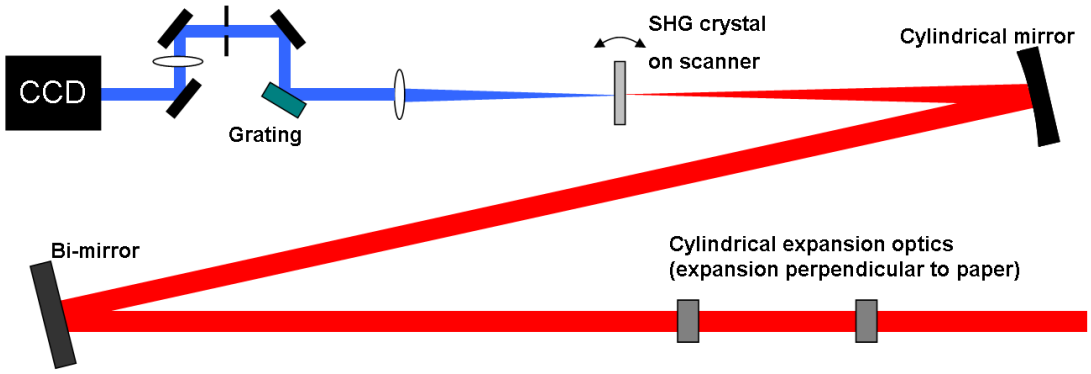

Figure 35: Simplified FROG setup for measuring ∼10 fs pulses. Notice that no dispersive element is used before the crystal. The compact spectrometer stage provides high enough resolution for broadband pulses. The long path length between the bi-mirror and crystal is needed to accommodate very small beam crossing angle.

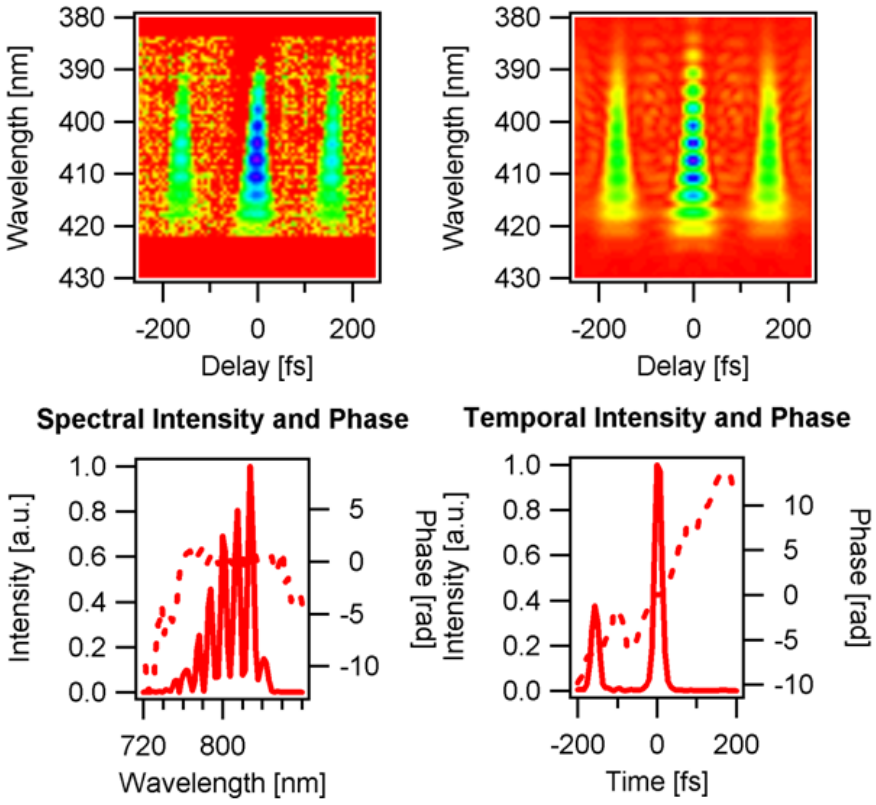

Figure 36: Measurements of a fairly challenging pair of ∼10-fs pulses by our short-pulse FROG.

6.3 Measuring extremely long pulses

For extremely long (several ps) pulses, the main challenge is the need for high spectral resolution to resolve the narrow bandwidth involved. Although this is possible by using a very long path spectrometer, we would like to avoid this and make the device compact. Another challenge is the very large delay range required. Below, we propose and test two long-pulse measurement schemes: one for measuring $\sim 2ps$ another for measuring even longer $\sim 5ps$ pulses. Before going into the details, we would like to clarify that, throughout this chapter, by "long pulses", we mean pulses close to being Fourier transform limited, therefore essentially narrow-band long pulses. We omit the measurements of broadband pulses chirped to long pulse lengths, as their measurements do not possess most of the challenges that the narrowband pulses do.

6.3.1 Pushing GRENOUILLE to its long-pulse limits

In the previous chapter, we worked on pushing the extremely simple GRENOUILLE device to its short-pulse limits. We showed that, GVD was the limiting factor for short-pulse measurements and $\sim 20fs$ is the short-pulse limit for GRENOUILLE's operation. Here we are interested in pushing GRENOUILLE to the other extreme: the measurement of long pulses.

GRENOUILLE uses the thick SHG crystals narrow phase-matching bandwidth (high GVM) to spectrally resolve the nonlinear signal (generated by the same crystal, which also acts as an autocorrelator). The phase-matching bandwidth or, equivalently, spectral resolution of the crystal is proportional to crystal length used [13]. Normally, in GRENOUILLE design, the crystal length is chosen to be the thickest possible without introducing much GVD, otherwise the pulse-to-be-measured is going to be distorted by the device. However, for very long pulses, GVD is not and issue due to narrow bandwidth involved. It is rather the GVM that limits the longest pulse measurable with GRENOUILLE. This is illustrated in the measurable pulse width range plot shown in Figure 37.

It may seem straightforward to achieve very high spectral resolution by using arbitrarily thick nonlinear crystal. Unfortunately this is not true due to several concerns. First of

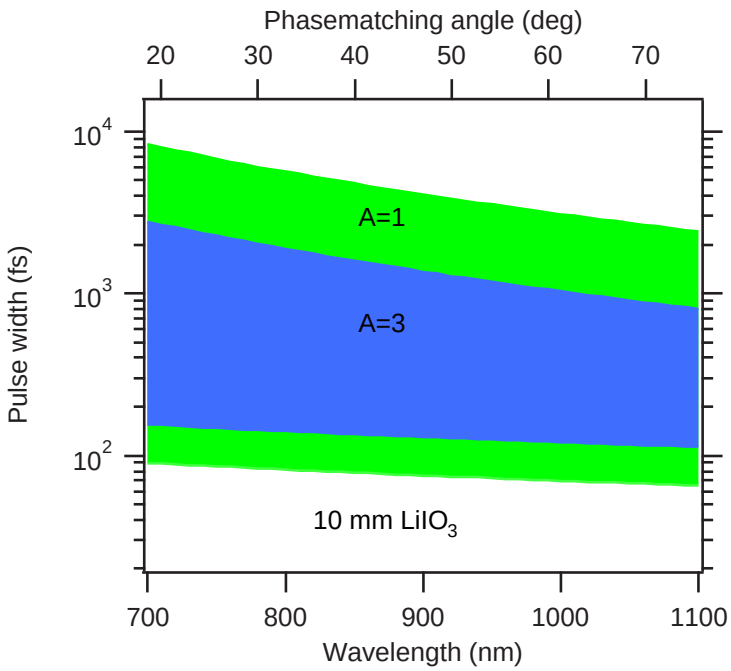

Figure 37: Pulse length range measurable by GRENOUILLE with $10mmLiIO_3$. In this plot, $A = 1$ is the tight edge, whereas $A = 3$ defines a more practical range of operation.

all, in order to have high enough conversion efficiency in the nonlinear crystal, the input beam needs to be focused to a small spot, where the electric field becomes very high. However, it is known very well that focused Gaussian beams diverge very fast (inversely proportional to focused spot size)[76, 78]. The beam stays intense over the range where it is "collimated". For quick evaluations, this range can be taken to be the "confocal parameter" of the Gaussian beam (twice the Rayleigh range). As a result, no matter how thick of a crystal is used, the effective length of the crystal used in the nonlinear interaction will always be limited by the focusing.

The effective crystal length considerations dictates that loose focusing is required. Unfavorably, there are other factors that are also dependent on focusing. First, the range of angles incident on the crystal should be large enough so that the entire pulse spectrum is phase matched over these angles. Long focal lengths, however, cause smaller, therefore insufficient divergence angle. Secondly, Making the focus too loose means a very long path-length of the beam, which is unfavorable since it tends to make the device inconveniently long.

All of these issues require doing an optimization on the focusing. Table 1 nicely illustrates the dependencies of various parameters on the focal length of the cylindrical lens (to be used to focus the beam into the crystal) f. We use the principles summarized in this table to find an optimized scheme to measure few-ps-long pulses.

Table 1: Dependencies of various parameter on focusing.

Parameter	Formula	Dependance on f
focused spot size	$w_f = \frac{\lambda f}{\pi w_{input}}$	f
Rayleigh range	$z_R = \frac{\pi w_f^2}{\lambda}$	f^2
Effective crystal length	$2 \times z_R$	f^2
Divergence angle	$\theta_{1/e} = \frac{\lambda}{\pi w_f}$	f^{-1}
Length of the device	$f + const.$	f

6.3.2 Experiment

In detail, we designed a GRENOUILLE for measuring few-ps-long pulses as follows: The input beam is first expanded with a 10× cylindrical Cassegrain telescope in the delay dimension. Then, a Keplerian [37] telescope (due to narrowband pulses involved, transmission through this much material does not cause any significant distortion) is used to expand the beam 2× in the wavelength dimension. The beam is then focused down into the SHG crystal with a $400mm$ focal length cylindrical lens. For SHG crystal here, we preferred to use $LiIO_3$ instead of BBO since $LiIO_3$ has more dispersion, so more spectral resolution at $800nm$ wavelength [23]. The beam splitting and crossing is accomplished using a "quad-mirror" assembly, the details of which are to be discussed in the following section. The nonlinear signal is then imaged onto the CCD in $2f - 2f$ (one-to-one imaging) manner in the delay dimension, and $f - f - f$ (mapping angle to position) manner in the wavelength dimension.

With this configuration, the confocal parameter inside the crystal is $9mm$. This returns a theoretical spectral resolution of $0.2nm$, which is sufficient to spectrally resolve the spectra of pulses that are a few ps long.

Figure 38 shows the test results for this long pulse GRENOUILLE. To simulate a

picosecond pulse with our femtosecond source, we used an air spaced etalon to generate a train of pulses. This corresponds to coarsely separated fringes in frequency, which will be used to test the resolution of the device. The first thing to note from Figure 38 is the achievement of very large delay range needed. In fact, the traces in the Figures are zoomed in and the actual delay range is even longer: $13ps$. Secondly, very finely spaced frequency fringes can easily be resolved, as expected. We were able to resolve spectral fringes separated by $0.17nm$ in the second harmonic. This resolution is quite noticeable since we did not use any external spectral resolving device, we solely used nonlinear optics. These results nicely matches our requirements.

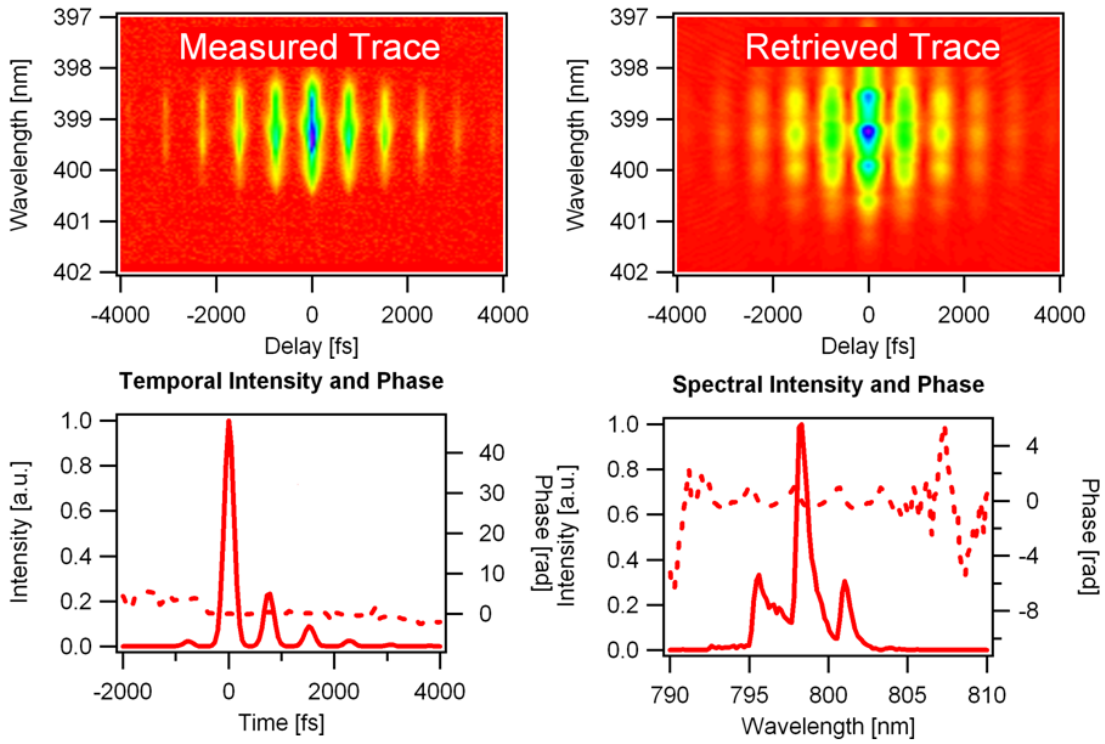

Figure 38: Measurements of the output of an etalon with the long-pulse GRENOUILLE.

Here, we would like to note parenthetically that, in the measurements shown in Figure 38, we used a source that has more bandwidth than the device can measure. Therefore, the retrieved FROG trace shows the "missing bandwidth", causing higher than normal FROG error. This, however, does not have any reflections on the conclusions that we draw here.

As a results, we show that by employing a $10mm LiIO_3$ crystal and a quad-mirror crossing scheme, we were able to push GRENOUILLE to its long pulse limit. We show that, this device can measure pulses that are as long as a few picoseconds.

6.3.3 Practical device for measuring several ps long pulses

In the previous section, we show that GRENOUILLE can be designed to measure a few (~ 2) ps pulses. Measuring even longer pulse with GRENOUILLE is not possible for some fundamental reasons as explained above. Therefore, for measuring longer pulses (our target is pulses that are $\sim 5ps$ long), we should return to the original FROG geometry, which has a spectrometer to spectrally resolve the nonlinear signal. Measuring such long/narrowband pulses are still difficult concerning the high spectral resolution required.

High spectral resolution can be managed with a long pathlength (typically $1m$) spectrometers. This would cause the device to be cumbersome. We instead exploit a high-groove-density grating at a grazing-incidence angle (to illuminate all of its grooves). This configuration provides very high spectral resolution without the need for long path length.

To see how this works, let's take a closer look at how a diffraction grating spectrometer works. Figure 39 shows a basic layout of such a spectoemeter. Basically, the grating disperses different colors to different angles and the lens images angles to position at its focal plane. With the illustration of the figure, we can assume that the two colors are spectrally resolved when their waist are completely separated at the focal plane of the lens.

The grating angular dispersion is given by [37]:

$$\frac{d\theta_m}{d\lambda} = \frac{m}{a\cos(\theta_m)} \tag{91}$$

where m is the diffraction orger and θ_m is the diffraction angle. After the lens, two nearby wavelengths will be separated by:

$$f\,\delta\theta_m = f\frac{m}{a\cos(\theta_m)}\delta\lambda \tag{92}$$

Setting this distance equal to the focused-spot diameter:

$$\frac{m\,f}{a\cos(\theta_m)}\delta\lambda = \frac{2w_1}{\cos(\theta_m)} = 2\frac{\lambda f}{\pi w_0\cos(\theta_m)} \tag{93}$$

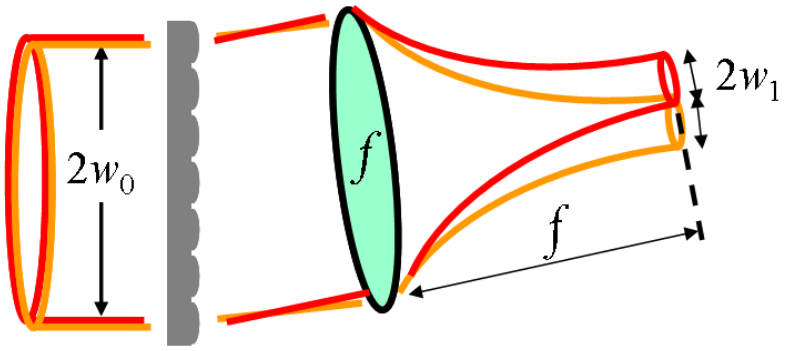

Figure 39: Derivation of spectral resolution of a grating spectrometer.

Solving for $\delta\lambda$, we obtain the resolution of the spectrometer:

$$\delta\lambda = \frac{4\lambda}{m\pi N} \tag{94}$$

where N is the number of grating lines illuminated ($N = 2w_0 \div a$).

This proves that the resolution of a diffraction grating spectrometer is directly proportional to the number of grating lines illuminated. Therefore, a small size beam can be diffracted off a grating at grazing angle incidence (essentially illuminating all of its lines) to achieve very high spectral resolution without needing a long path. By exploiting this fact, we experimentally demonstrated that, a 50-mm-long, 2400-line/mm grating resolves spectral structure as small as 0.08 nm (Figure 40). This spectral resolution is sufficient to resolve spectra of pulses several ps long, in a very compact device.

Another issue for long-pulse measurements is the required long delay range. Using a translation stage requires a long travel and inconvenient data acquisition time. It also does not allow for single-shot operation. While the simple pulse splitting and recombining optic, the Fresnel biprism [65] would be a good solution, the required delay range sets unpractical prism apex angles. We instead used a "quad-mirror" assembly (see Figure 41 to split the beam into two halves and cross them at a large angle. The only condition on the crossing angle is mandated by the phasematching in the crystal. We calculated that for $LiIO_3$, the largest beam crossing angle can be 64 degrees.

Using our quad-mirror design, we achieved a ~20 ps delay range in a single-shot geometry

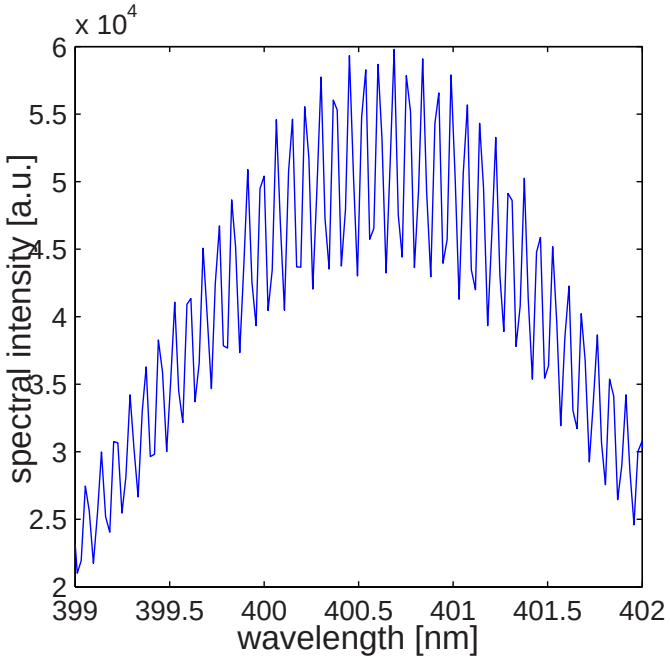

Figure 40: A spectrum obtained with grazing angle incidence grating.

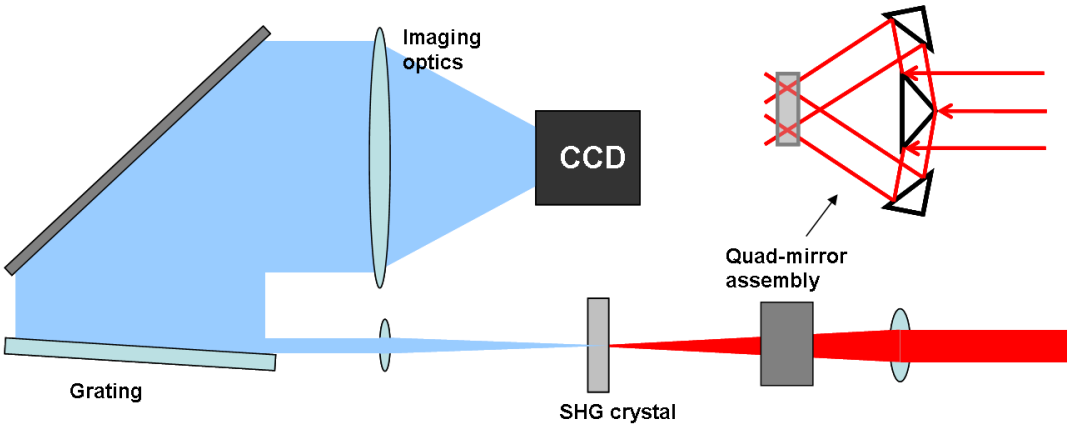

Figure 41: Setup for measuring several-ps-long pulses. The narrowband second-harmonic pulse is spectrally resolved using a grazing-incidence grating. The insert shows a quadruple mirror design that conveniently splits the beam in two halves and cross them at very large angle, yielding a large relative delay.

by crossing two large line-focused beams at a very large (50^0) angle, which allows phase-matching in the crystal (Figure 41). Combined with the hign resolution provided by the grazing-angle-grating spectrometer, our compact and simple FROG can easily measure pulses as long as $\sim 5ps$.

To summarize this chapter, we presented simple and reliable pulse measurement devices for measuring extremely short and extremely long pulses. These devices are considerably simpler and easier to work with. Even better, they also measure the complete pulse intensity and phase vs. time and frequency, as well as the two most important spatio-temporal distortions, spatial chirp and pulse-front tilt. They measure single pulses or high-rep-rate trains of pulses in real time, and they do so very accurately. Coupled with recent massive increases in the speed of the FROG pulse retrieval algorithm [41], which now retrieves pulses at a rate of $\sim$20 pulses per second on most computers, all of these devices are ideal for measuring most ultrashort pulses in use today.

CHAPTER VII

MEASURING SEVERAL-CYCLE 1.5-μm PULSES USING FREQUENCY-RESOLVED OPTICAL GATING

This chapter originally appeared as a paper by the author:

Selcuk Akturk, Mark Kimmel, Rick Trebino, Sergey Naumov, Evgeni Sorokin and Irina Sorokina, "Measuring several-cycle $1.5-\mu m$ pulses using frequency-resolved optical gating", Optics Express 11, 3461-3466 (2003) [3]

7.1 Introduction

Extremely broadband several-optical-cycle pulses near telecommunication wavelengths ($\sim 1.5\mu m$), are in high demand for telecommunications, optical coherence tomography and numerous other applications. Recently, a number of publications have considered the possibility of several-cycle-pulse generation [72, 73, 60, 59]. The techniques included Kerr-Lens-mode-locking (KLM) [72, 73], as well as "semiconductor saturable absorber mirror" or SESAM-based mode-locking [60, 59]. Both prismless [72, 60] and direct diode-pumping [59] have been implemented (see Figure 42. Direct diode-pumping opens the way for broad usage of affordable compact low-power oscillators.

Reliably generating near-infrared pulses requires reliable, accurate, and robust measurement techniques. While it is possible to build an autocorrelator with a proper choice of crystal, especially for shorter pulses, it yields only rough pulse-length information and no pulse phase information and no information about the pulse temporal shape. And at such short pulse lengths, spectral and temporal phase information becomes vital [87]. While another method proposed for IR pulse measurements, free-space electro-optic sampling [99] could provide this information, this method requires a shorter probe pulse, and it also has group velocity mismatch issues.

With the most commonly used intensity-and-phase ultrashort-pulse-measurement

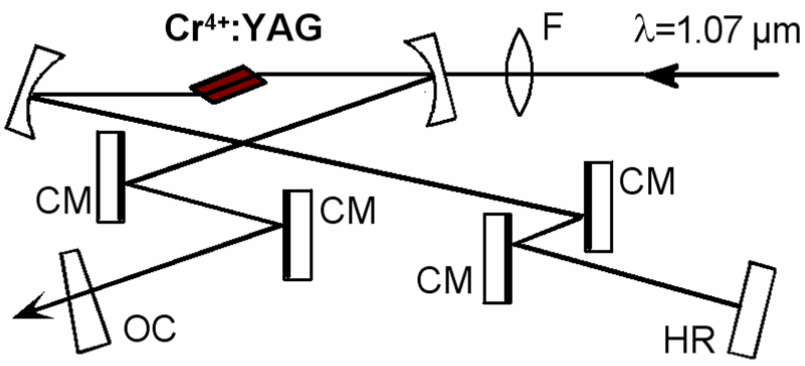

Figure 42: The $Cr4^+ : YAG$ laser setup. The mode-locking is achieved by a KLM mechanism with a prismless dispersion compensation. CM: chirped mirrors. One particular advantage of $Cr4^+ : YAG$ as a gain medium is that its absorption band covers very convenient diode laser wavelengths. Diode laser pumping reduces the size and cost of the device significantly.

method, frequency-resolved optical gating, (FROG) [42], it is now possible to measure pulses on a single shot [87]; over a wide range of wavelengths [87, 71], pulse lengths [8, 49], and complexities [35]; and to do so in a manner that is general, robust, accurate, and rigorous. FROG also routinely allows convenient real-time monitoring of ultrashort-pulse intensity and phase. However, FROG has never been tried for such short IR pulses and also with low input power. Thus, in this paper, we engineer a FROG device for this purpose and which combines several recent innovations.

7.2 1.55-micron Pulse Measurements

All pulse-measurement techniques require the use of a nonlinear-optical process, whose phase-matching bandwidth is inversely proportional to the crystal thickness. For very short pulses, very thin second-harmonic-generation (SHG) crystals are usually required. However, we have recently shown that angle-dithering a SHG crystal that is otherwise too narrowband (that is, too thick) yields a significantly increased effective phase-matching bandwidth in FROG measurements for a given crystal thickness [64]. This is possible because the device

phase-matching bandwidth need only exceed that of the pulse over the course of the measurement and not necessarily on every pulse. Because the SHG efficiency scales as the square of the crystal thickness, angle-dithering also yields significantly greater signal strength. This is very important since the nonlinearity of most crystals decreases significantly at IR, where the use of a thicker crystal can compensate for the relatively low nonlinearity. Indeed, this approach works so well that we are able to use a line focus, rather than a point focus, and still achieve sufficient intensity to measure the train of pulses.

While angle-dithering avoids the phase-matching requirement, or equivalently the group-velocity mismatch (GVM) requirement, the SHG crystal cannot, however, be arbitrarily thick in these measurements. The crystal must still have negligible group-velocity dispersion (GVD) to avoid distorting the pulse. This issue is rarely mentioned in pulse-measurement problems because it is automatically satisfied when GVM is made negligible. It becomes an issue when angle-dithering is used due to the removal of the GVM constraint and the relatively thick crystal (here $\sim$1 mm). And it is an issue here, even at the low-dispersion wavelength of $1.5\mu m$, due to the shortness of the pulse and the resulting large breadth of the spectrum. Fortunately, we find that $1-mmLiNbO_3$ and $LiIO_3$ crystals yield negligible GVD for pulses as short as a several optical cycles (Figure 43). The rest of our setup is also designed to minimize material dispersion.

Recall that all FROG devices involve splitting the beam into two identical beamlets, which must then overlap in space and time in a nonlinear crystal whose SHG signal is then spectrally resolved vs. relative beamlet delay. Our setup also exploits the simplicity of single-shot FROG [87]. As single-shot FROG maps delay onto transverse position, two beamlets must overlap in time and in space at a line focus, rather than a point focus. We used a reflective telescope to first expand the beam for larger delay range. We also used a Fresnel biprism for beam splitting and crossing, which was first introduced in the GRENOUILLE [65] technique. The Fresnel biprism eliminates the beam splitter and beam-recombining optics and automatically ensures the temporal and spatial overlap between the two beamlets. To obtain the line focus on the nonlinear crystal, we used a cylindrical mirror. The SHG crystal is mounted on a resonant scanner for angle dithering. The nonlinear signal

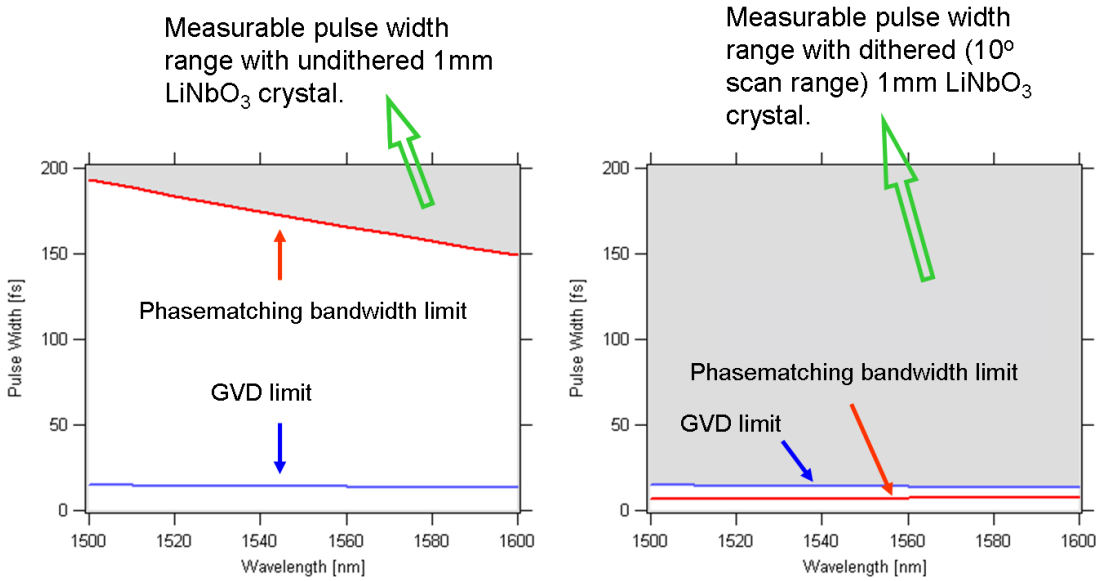

Figure 43: The effect of angle dithering on the measurable pulse range. The shaded area denotes the measurable pulse width range. Note that angle dithering relaxes the phase-matching bandwidth constraint, allowing accurate measurement of much shorter pulses.

is then mapped onto the slit of a spectrometer, with a CCD camera at its output plane. The whole setup has only one transmissive element, the relatively thin Fresnel biprism (only 1.3 mm of fused silica), before the nonlinear crystal (dispersion after the crystal is irrelevant).

An additional advantage of this setup is that, since it maps delay onto position, like all other single-shot FROG devices, it also measures spatial chirp [5]. And since it uses a Fresnel biprism to do so, it also measures pulse-front tilt [4].

7.3 Experiment

We used a KLM Cr4+:YAG laser (Figure 42) yielding pulses with approximately 110 nm of bandwidth near $1.55\mu m$ [60], producing pulses with 50 mW of average power at a 100 MHz repetition rate. We also used chirped mirrors in the cavity for dispersion compensation, suppressing the third-order dispersion [60]. The output pulses were measured with the angle-dithered SHG FROG (Figure 44). In our FROG setup, we used a $1 - mmLiIO_3$ crystal, mounted on an EOPC SC40 type scanner, oscillating at 30 Hz with an amplitude of about 10^0. The pulses were split and combined using a 177^0 apex angle Fresnel biprism,

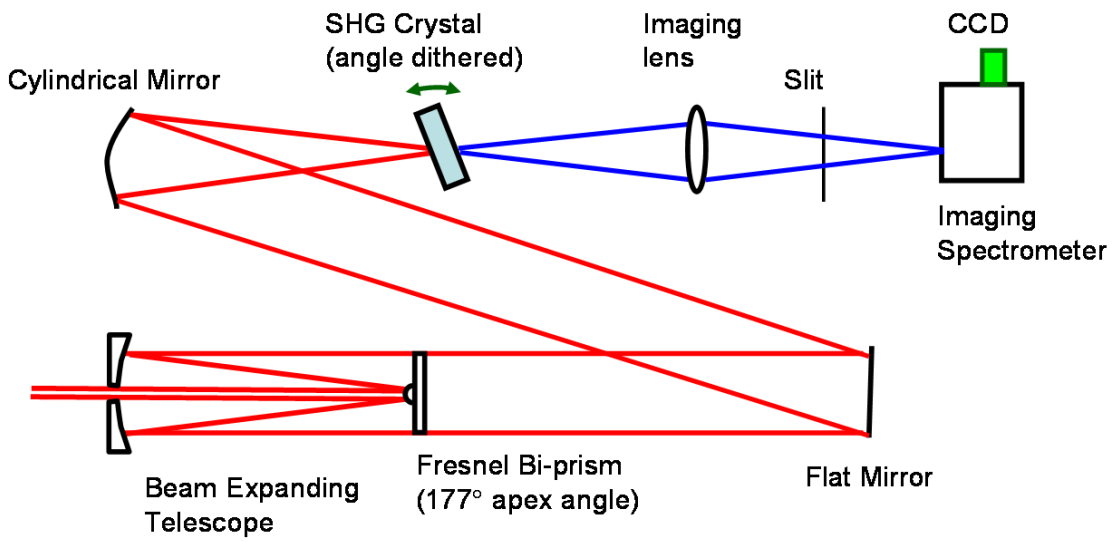

Figure 44: Angle-dithered SHG FROG geometry. Note that this setup employs all reflective optics except for the Fresnel biprism (1.3 mm of fused silica) before the nonlinear crystal, minimizing the material dispersion. This diagram shows a Cassegrain telescope for beam expansion; but we have also used a simple slightly off-axis reflective telescope (without the hole).

which ensured both spatial and temporal overlap, without any additional alignment. A 10-mm cylindrical mirror was used to obtain a line focus along the delay axis, as per the usual single-shot FROG geometry [43]. Here, "single-shot" refers to the mapping of delay onto position by crossing at a line focus, allowing the potential measurement of a single pulse. However, our measurement here is "multi-shot" in the sense that it is not of a single pulse, but averaged over a number of identical pulses. The resulting SHG signal was imaged onto the slit of Acton SpectraPro150 spectrometer. The spectrometer output was recorded by a Sony XC-ES50 CCD camera and Spiricon SP-LTA video capture card, and the intensity and phase retrieved from the resulting FROG traces using the Femtosoft SHG FROG code.

The total group-delay dispersion of our device was only $1.6as/nm$, so that a $37-fs$ $1.55-\mu m$ flat-phase Gaussian pulse would increase to $37.2-fs$ by the time it reached the center of the crystal. And, although the crystal phase-matching bandwidth was $39-nm$, the range of phase-matched wavelengths was 500 nm with the crystal angle-dithering.

Figure 45 shows the measured and retrieved FROG traces, as well as the retrieved and independently measured spectra, all of which are in very good agreement with each other.

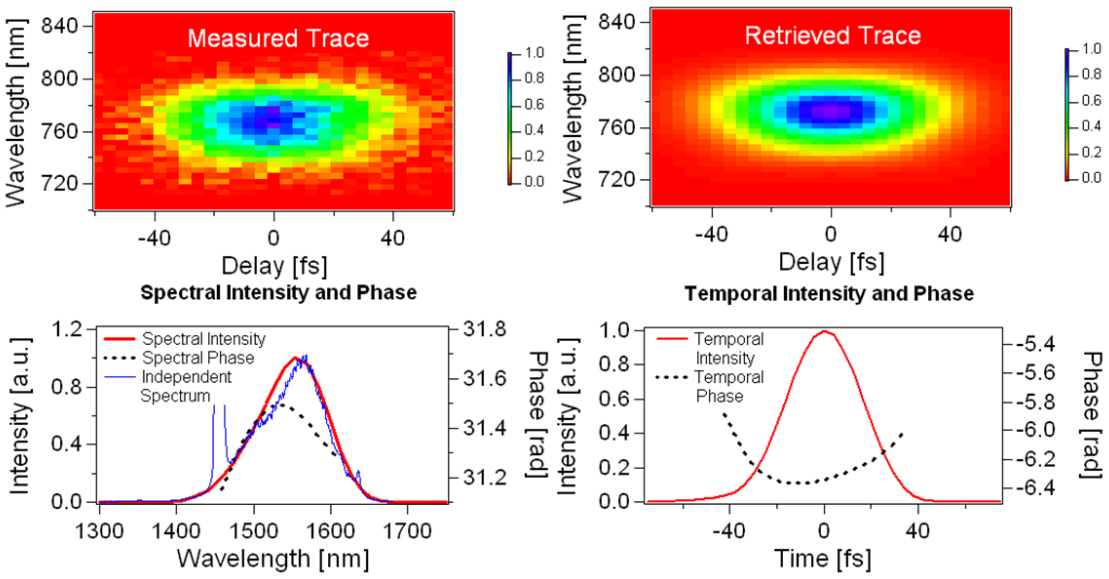

Figure 45: FROG measurements of full intensity and phase of Cr4+:YAG laser. The retrieved pulse width is 37.1 fs (FWHM). The spike in the independently measured spectrum is the continuous-wave (CW) component oscillating in a higher transverse mode. FROG is designed not to see this spike due to its ultrafast gating and small range of delays.

The measured pulses are 37.1 fs long (FWHM) and have nearly Gaussian intensity envelope with only a few tenths of a radian of phase distortion. Our measurements thus show that the chirped mirrors sufficiently compensate for the cubic phase and do not introduce significant higher-order phase distortions into the pulse.

We performed another set of measurements, this time with the laser slightly modified. Specifically, we used fused-silica prisms in the cavity for dispersion compensation, in combination with the chirped mirrors. In this case, the intracavity dispersion had a significant positive third-order component, due to the material dispersion of both YAG and fused silica. Then we measured the output pulses with our FROG. Figure 46 shows the measured and retrieved FROG traces, as well as retrieved and independently measured spectrum, again, all of which are in very good agreement with each other. The measured pulse width was about 25*percent* longer, 46.6 fs (FWHM). However, unlike the chirped mirror case, these pulses had also visible third- and higher-order phase distortions. In addition, side-bands appear in the spectrum, as expected in systems with large higher-order dispersion [50]. These spectral spikes do not appear in the FROG measurement because they correspond

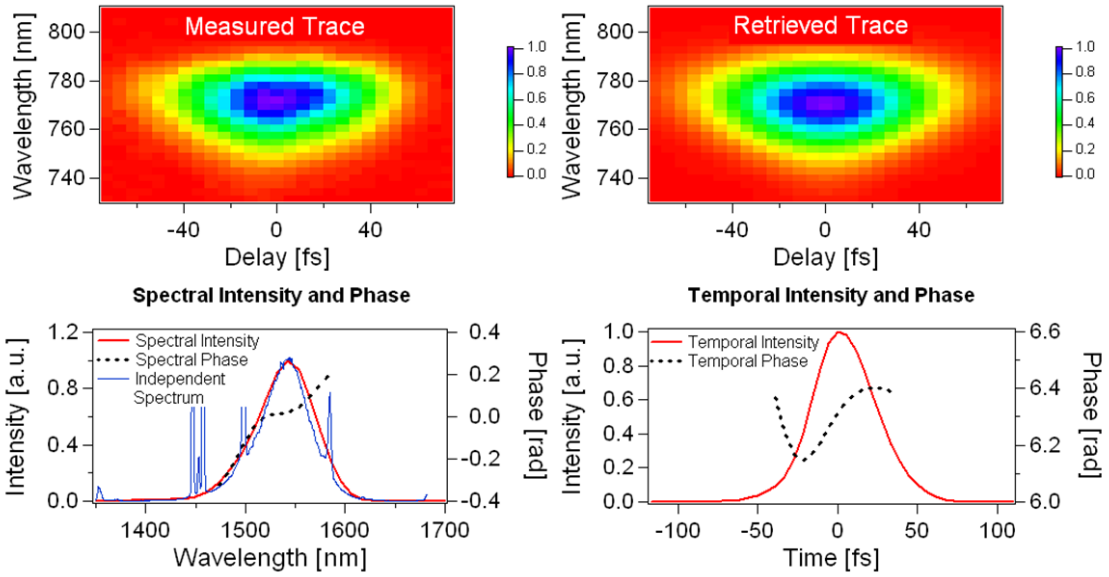

Figure 46: FROG measurements of the intensity and phase of Cr4+:YAG laser output pulses. The retrieved pulse width is 46.6fs (FWHM). The narrow spikes in the independently measured spectrum are the cw component and sidebands originating from the higher-order dispersion inside the cavity.

to very slow and weak components and persist for much longer times than the delay range scanned.

The above measurements were performed using a relatively powerful 50 mW of average power. In order to find the applicability of our FROG system for monitoring very low-power oscillators, we used neutral density filters to attenuate the beam. We were able to measure pulses as weak as 5 mW (average power), at the repetition rate of 100 MHz. If even lower-power operation is desired, the experimentally simple Fresnel biprism/cylindrical lens/line focus that we used could be replaced a more traditional (somewhat more complex) beam-splitter and spherical focus to increase the intensity at the SHG crystal. We estimate that this approach could measure a 100 MHz pulse train of several-cycle IR pulses of as little as a few tens of μW. Our estimations also show that our low-dispersion device could measure $1.55-\mu m$ pulses as short as 20 fs without introducing significant pulse distortion. This corresponds to a $1.55-\mu m$ pulse only four cycles long. For shorter pulses, a thinner crystal and a "Fresnel bi-mirror" would further decrease the dispersion, allowing the accurate measurement of few-cycle pulses.

In conclusion, we have measured the full intensity and phase of $\sim 40-fs$, $1.55\mu m$ pulses from a $Cr4^{+}:YAG$ laser using an angle-dithered SHG FROG. Our measurements show that, by using a relatively thick crystal and angle dithering, FROG can be extended well into the infrared even for several-cycle pulse measurements, and can be used as a convenient monitoring tool with very low-input power.

CHAPTER VIII

EXTREMELY SIMPLE DEVICE FOR MEASURING 1.5-μm ULTRASHORT LASER PULSES

This chapter originally appeared as a paper by the author:

Selcuk Akturk, Mark Kimmel and Rick Trebino, "Extremely simple device for measuring $1.5-\mu m$ ultrashort laser pulses", Optics Express 12, 4483-4489 (2004) [7]

8.1 Introduction

Sources of $1.5-\mu m$ ultrashort laser pulses are becoming ever more important and prevalent. Mode-locked fiber lasers [61, 1], for example, are typically experimentally simple, robust, and single spatial mode. Moreover, they generate moderately intense ultrashort pulses, $\sim$100 fs to $\sim$1 ps long, making them useful, not only for telecommunications, but also for nonlinear-optical applications. At present, several commercial fiber lasers are available with various pulse characteristics. Another important source of ultrashort pulses in this spectral region is optical parametric oscillators (OPO's) and amplifiers (OPA's) [13], which yield pulses of about the same length, but which can achieve considerably higher energies. Several commercial OPO's and OPA's are also available.

The temporal intensity-and-phase behavior of fiber-laser, OPO, and OPA pulses can be quite complicated. Worse, OPO and OPA pulses are frequently contaminated with the spatio-temporal distortions, spatial chirp and pulse-front tilt. Unfortunately, the device often used to measure them, the autocorrelator, yields only very limited temporal-intensity information and, of course, no pulse-phase information. And extracting quantitative information regarding spatio-temporal distortions from an autocorrelation is difficult. More powerful methods, such as frequency-resolved optical gating (FROG)[87], which is a spectrally resolved autocorrelation, yield this information, but they are experimentally more complex than autocorrelation. Alternative methods to FROG are even more complex.

An ultrasimple and elegant variation on FROG, called GRENOUILLE (GRating-Eliminated No-nonsense Observation of Ultrafast Incident Laser-Light E-fields) [6, 65], was recently introduced and demonstrated for measuring Ti:Sapphire laser pulses (that is, from 700 to 1000 nm) over the pulse-length range of $< 20fs$ to $\sim 1ps$. GRENOUILLE can also measure spatial chirp and pulse-front tilt easily and without modification to its apparatus, as detailed in the earlier chapters.

Extension of the GRENOUILLE idea to $1.5 - \mu m$ wavelengths is not straightforward, however. GRENOUILLE uses a thick second-harmonic-generation (SHG) crystal to spectrally resolve the autocorrelator signal pulse, and commonly used SHG crystals have insufficient dispersion to do so at $1.5 - \mu m$, a wavelength range where the dispersion of most materials is very low. In this letter, we show, however, that an all-but-forgotten SHG crystal, Proustite, has sufficient dispersion and yields an ideal GRENOUILLE device for this wavelength range. We then use it to measure fiber-laser pulses and $1.5 - \mu m$ pulses with pulse-front tilt.

8.2 GRENOUILLE and its extension to $1.5 - \mu m$ *pulses*

GRENOUILLE operates by using a simple Fresnel bi-prism to split the beam into two beams automatically crossed in space and time in the crystal with relative delay mapped onto transverse position. It also uses a thick crystal that phase-matches a small and different fraction of the pulse bandwidth for each output angle, allowing the crystal to operate, not only as an autocorrelating element, but also as a spectrometer. This yields a very simple, compact FROG device that requires almost no alignment. GRENOUILLE also measures the spatio-temporal distortions, spatial chirp and pulse-front tilt, without modification [4, 5]. Spatial chirp shears, and pulse-front tilt displaces, the otherwise symmetrical trace.

The challenge in designing a GRENOUILLE for the $1.5 - \mu m$ wavelength region, and fiber lasers in particular, is the relatively small bandwidths (usually $<\sim 40nm$) of pulses for the relatively long pulses relative to Ti:Sapphire lasers. At first glance, this simplifies the problem: longer pulses suffer less from group-velocity dispersion (GVD) in the optics and, especially, the thick crystal. On closer examination, however, the crystal must also be

dispersive enough that its finite phase-matching bandwidth is able to resolve the spectrum of the second-harmonic signal. Equivalently, it should have a relatively large group-velocity mismatch (GVM), which is a challenge in the relatively nondispersive $1.5-\mu m$ wavelength range. Therefore, in order to build a GRENOUILLE to measure pulses with narrow spectra, we require a crystal with relatively high dispersion. We find, however, that the common (low-dispersion) nonlinear crystals used in the visible and near-infrared ranges are effective for measuring only considerably shorter $1.5-\mu m$ pulses [3] (where there are few currently available sources, and other, more fundamental, challenges must be met before a relevant GRENOUILLE can be designed). Worse, the nonlinearities of standard crystals also drop in this wavelength range, reducing the device sensitivity. Therefore, the problem of measuring fiber-laser, OPO, and OPA pulses with GRENOUILLE is not trivial, and it relies on the existence of a suitable nonlinear crystal (The detailed procedure on crystal selection for GRENOUILLE can be found in [63]).

For this purpose, we investigated numerous nonlinear crystals. BBO and $LiNbO_3$ are common crystals that phase-match at $1.5-\mu m$ [23], but they both have very small GVM in this region, preventing their use as a GRENOUILLE crystal. $LiIO_3$ has a relatively large GVM, but it still does not yield sufficient spectral resolution for our purposes. Of less common crystals, $GaSe$ has suitable GVM but, due to its mechanical properties, it is not possible to cut it at a particular angle. New crystals, such as $AgGaGeS_4$, and cannot yet be grown thick enough. And older crystals, which appear promising from properties reported many years ago, such as Cinnabar, are no longer available.

Fortunately, we have found that a nearly forgotten, crystal, Proustite (Ag_3AsS_3), has a larger phase-matching dispersion (10 times that of $LiIO_3$) and a stronger nonlinear-optical coefficient (15 times that of $LiIO_3$) [23] and matches GRENOUILLE's requirements for this range very well (see Figure 47).

More quantitatively, GRENOUILLE uses the large GVM in the thick crystal to spectrally resolve the signal pulse. This condition can be expressed as [87, 65]:

$$\mathrm{L} \times \mathrm{GVM} \gg \tau_{\mathrm{p}} \tag{95}$$

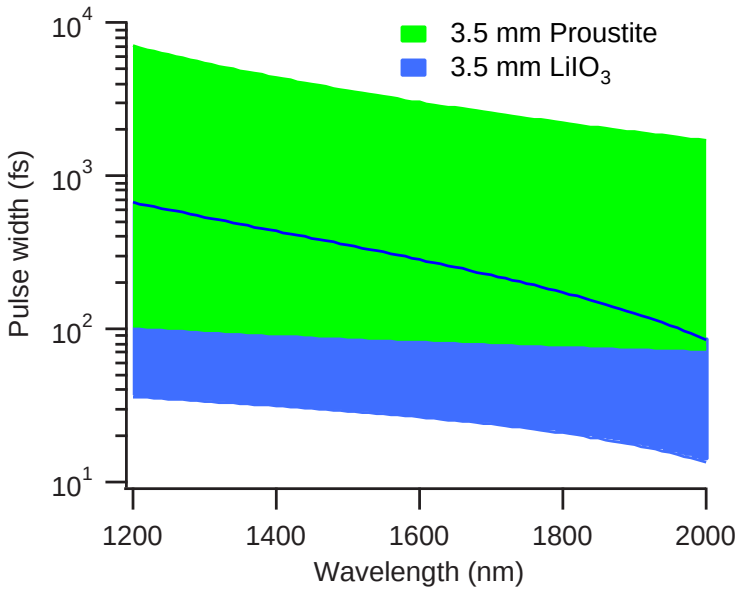

Figure 47: Pulse-width range measurable using a GRENOUILLE with a $3.5 - mm$ Proustite crystal (green region) or alternatively a $3.5 - mm$ $LiIO_3$ crystal (blue region). The upper limit of each region represents the limit set by the spectral resolution of the crystal ($L \times GVM = \tau_p$). The lower limit of each region represents the limit set by GVD induced by the crystal ($L \times GVD = \tau_c$). The green curve in the blue region shows the lower limit of the area of the region of pulses measurable using Proustite.

where L is the crystal interaction length, and τ_p is pulse length. The condition to have negligible GVD is:

$$\mathrm{L} \times \mathrm{GVD} \ll \tau_\mathrm{c} \tag{96}$$

where τ_c is coherence time.

Applying these conditions to 200-fs (16.5-nm bandwidth), $1.5 - \mu m$ pulses in Proustite, we find: $GVM = 1.71 \times 104 fs/cm$, and $GVD = 93.9 fs/cm$. A crystal length of 3.5 mm yields $L \times GVD = 32.8 fs$, and $L \times GVM = 6 ps$. These values are comfortably far from each other, thus satisfying both of the above two constraints, allowing accurate pulse measurements. A 3.5-mm Proustite yields 0.92 nm spectral resolution at $1.5 - \mu m$, which allows accurate measurement of pulses as long as several ps. The crystal GVD will broaden a transform-limited 100-fs pulse to only 109 fs (using half the crystal length). Finally, a full beam divergence angle of 4.0^0 in the crystal yields 85 nm of spectral range.

8.3 Experiment

We measured pulses from a Menlo Systems TC-1550-B fiber laser, operating near 1570 nm with an output power of 20.5 mW (25 MHz repetition rate). The design parameters of our Proustite GRENOUILLE were as follows: the fiber output was collimated with a fiber collimator (beam diameter 2.9 mm) and then expanded with a 5× refractive telescope. A 75-mm-focal-length cylindrical lens then focused the beam. A biprism (apex angle 160^0) split the beam into two and crossed them inside the 3.5 mm Proustite crystal. A pair of back-to-back plano-convex 50-mm-focal-length spherical and cylindrical lenses then mapped the GRENOUILLE trace onto a 1/2" CCD camera, 100 mm away from the crystal. The image was then captured using a Spiricon SP-LTA video capture card, and the intensity and phase retrieved from the resulting FROG traces using the Femtosoft SHG FROG code.

Figure 48 shows the measured and retrieved GRENOUILLE traces. For comparison, we also measured the same pulses using a conventional multi-shot FROG (see Figure 48). All these measurements are in excellent agreement with each other, verifying the accuracy of the GRENOUILLE.

In order to test the device's ability to measure complicated pulses as well as at other near-IR wavelengths, we performed another set of measurements, this time using the IMRA Femtolite Series tunable fiber laser operating near 1700 nm. At the output we used an air-spaced etalon ($125 - \mu m$ separation), which generated multiple pulses in time and fringes in frequency. We measured the resulting complex output with GRENOUILLE and obtained an excellent measurement of the pulse train (Figure 49). These results show that the device is capable of resolving the fine structure in frequency due to the high spectral resolution of Proustite. The same traces can also used for calibration purposes (knowledge of the etalon spacing determines both the separation of the various regions in the traces in both delay and frequency).

As mentioned earlier, GRENOUILLE also measures pulse-front tilt very sensitively [4]. Specifically, pulses with pulse-front tilt have GRENOUILLE traces with a shift in delay relative to the otherwise symmetrical GRENOUILLE trace (which is otherwise centered at zero delay). While fiber lasers are generally free from pulse-front tilt, OPO and OPA

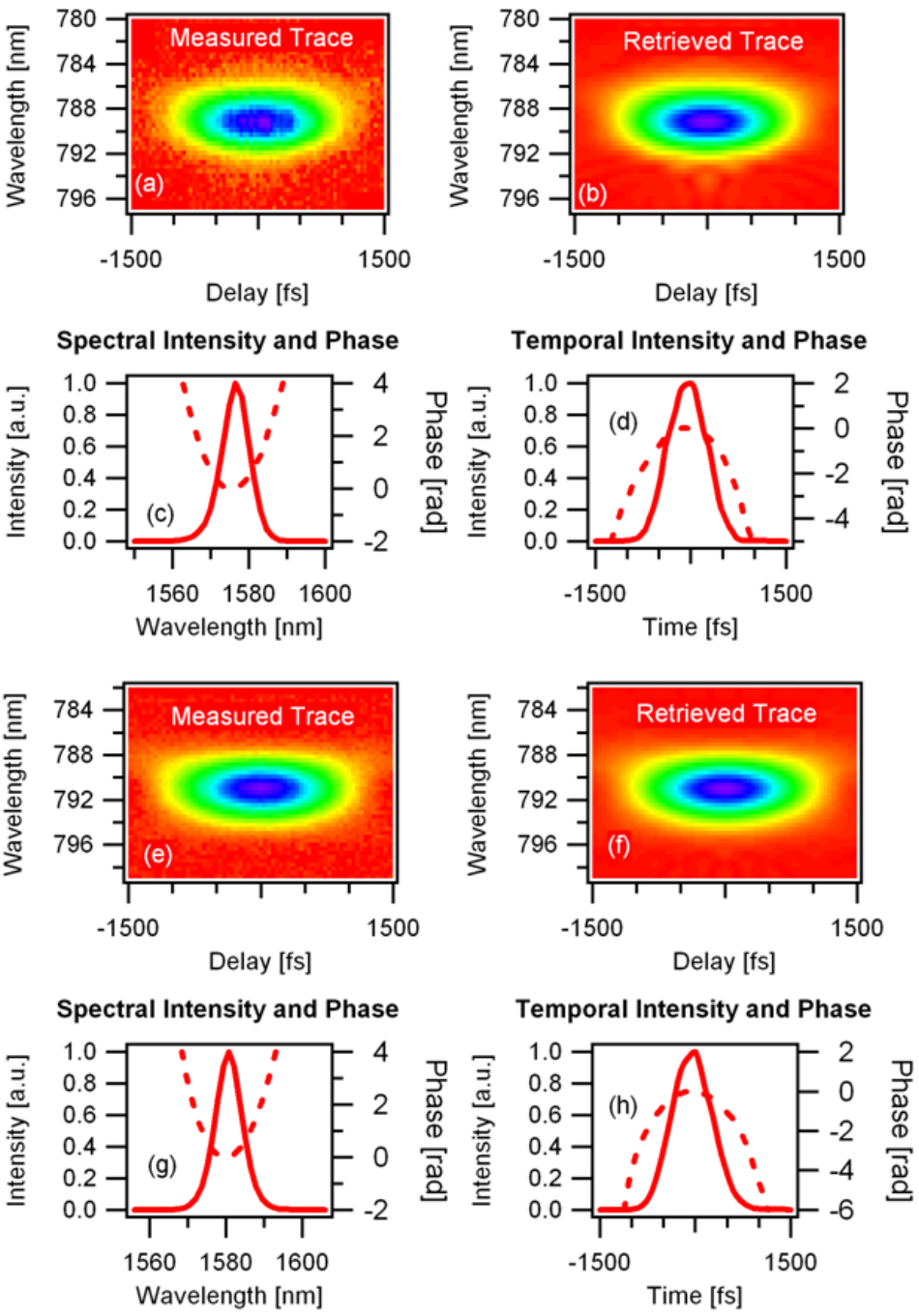

Figure 48: Tests of our $1.5-\mu m$ GRENOUILLE: (a) measured GRENOUILLE trace; (b) retrieved GRENOUILLE trace (FROG error:0.0055); (c-d) retrieved temporal and spectral intensity and phase (the retrieved pulse width is 779 fs and the bandwidth is 8.2 nm); (e) measured multi-shot FROG trace; (f) retrieved multi-shot FROG trace (FROG error:0.0023); (g-h) retrieved temporal and spectral intensity and phase (the retrieved pulse width is 765 fs and the bandwidth is 8.1 nm).

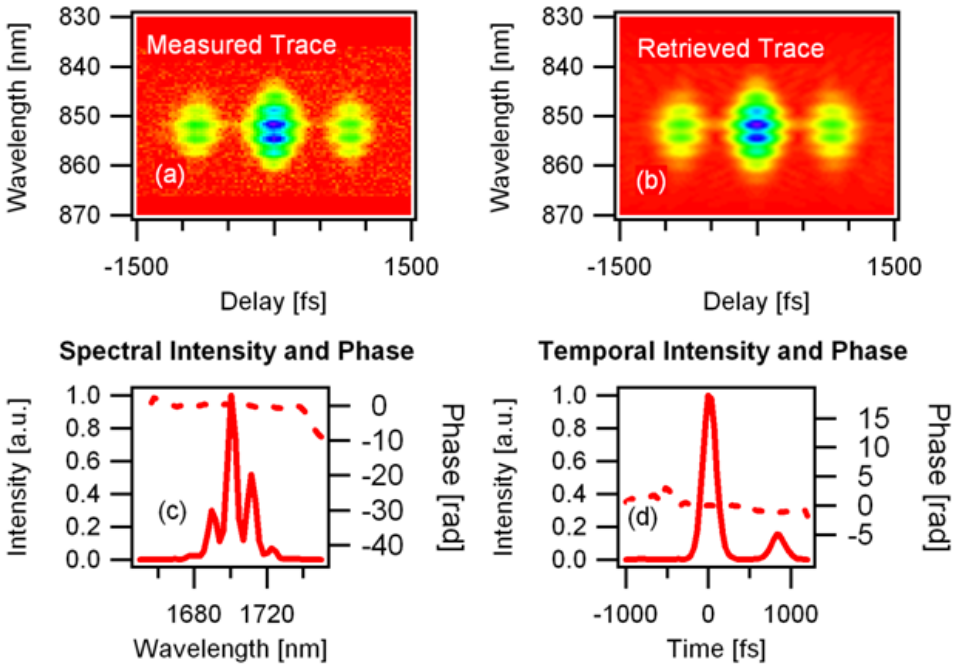

Figure 49: Tests of our $1.5-\mu m$ GRENOUILLE with more complicated pulses: (a) Measured and (b) retrieved GRENOUILLE traces (FROG error 0.0055) for a double pulse; (c-d) retrieved spectral and temporal intensity and phase.

pulses are very likely to be contaminated with pulse-front tilt (and other spatio-temporal distortions). Therefore, it is important to be able to monitor this effect, and it would be convenient to be able to do so using the same device that is used for intensity and phase measurements.

To demonstrate pulse-front tilt measurements with GRENOUILLE we introduced pulse-front tilt by introducing both spatial and temporal chirp [2]. We used a prism pair to generate spatial chirp, and by pushing one prism in and out of the beam, we varied the pulse-front tilt. Figure 50 shows two GRENOUILLE traces with different amounts of pulse-front tilt (the spatial chirp in the beam was too small to measure using GRENOUILLE).

Extending GRENOUILLE to wavelengths beyond $2\mu m$ will require yet another unusual crystal. Proustite's phase-matching curve reaches a minimum between 3 and $3.5\mu m$, so its phase-matching dispersion becomes too small for application to GRENOUILLE in that region. However, Proustite is ideal for GRENOUILLE devices for measuring pulses between 1.2 and $2\mu m$, and a thicker (thinner) Proustite crystal could in principle measure longer

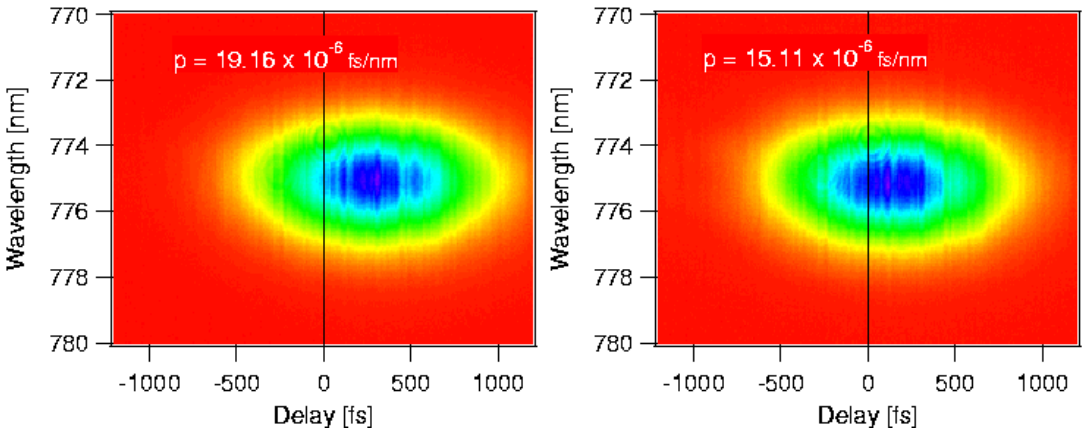

Figure 50: GRENOUILLE traces for pulses with different amount of pulse-front tilt. The shift of the trace reveals and measures the pulse-front tilt. Note that these traces are not centered at zero delay, and the trace with greater pulse-front tilt has greater displacement from zero delay, as expected.

(shorter) pulses at these wavelengths.

In conclusion, we have shown that, by using the nonlinear-optical crystal, Proustite, a GRENOUILLE can be designed to measure $100 - fs$ to few-ps pulses near $1.5\mu m$ generated by fiber lasers, OPO's and OPA's. Due to the high spectral resolution that Proustite provides, the device can measure pulses with spectra as narrow as 1 nanometer. Moreover, the design remains as simple and as compact as previously developed Ti:Sapphire GRENOUILLEs, providing easy alignment, high sensitivity, spatio-temporal-distortion measurement, and real-time operation.

CHAPTER IX

MEASURING ULTRASHORT PULSES IN THE VISIBLE

9.1 Introduction

In the previous two chapters, we concentrated on extending the ultrashort pulse measurements to longer wavelengths, specifically to pulses that are centered at around wavelength of $1.55\mu m$. We established pulse measurement techniques for two distinct pulse-length regimes at that wavelength. This chapter will be dedicated to pulse measurements for ultrashort pulses centered at shorter wavelengths: ultrashort pulses in the visible region of the spectrum, covering 500 nm to 700 nm.

As in all other pulse measurement studies, one of the most compelling motivation for extending ultrashort pulse measurements to visible is the broad range of applications in these wavelengths. Ultrashort pulses in the visible are very commonly used in many applications. For example, "time resolved photoluminescence" is one of the workhorse methods used in semiconductor physics to determine the band structures of semiconductors and tunable ultrashort sources in the visible are used very often [80, 52]. Other applications of visible ultrashort lasers include material characterization, micro-machining and ultrafast spectroscopy [83]

Due to lack of available materials, direct generation of ultrashort pulses in the visible has not been flourished. Researchers use, instead, nonlinear conversion methods like optical parametric amplification/oscillation (OPA/OPO) to generate ultrashort pulses at the desired wavelength. OPA/OPOs can use, as an input, amplified Ti:Saphire outputs, which are very well established and robust to date. Typically, in the OPA/OPOs, first a broadband light (so called continuum) is generated using self phase modulation. Then, the continuum is mixed with the pump, in a nonlinear medium, in which amplification occurs [13]. Depending on the phasematching considerations, such an amplification can cover a very large range of wavelengths and very short pulses can be generated. Generation of $sub-8-fs$

pulses was demonstrated by Cerullo et.al. [14].

Developing reliable, robust and convenient pulse measurement techniques for these extremely short-visible pulses will promote both the application and generation of them. Unfortunately, pulse measurement methods are currently not extended to these wavelengths. In this work, we propose and test Frequency Resolved Optical Gate (FROG) [42] to measure extremely short pulses in the visible.

9.2 Extending frequency resolved optical gating to ultrashort pulse measurements in the visible

There are a few reasons why measuring extremely short pulses in the visible is very difficult. First, due to their broad bandwidth, these pulses are very vulnerable to group velocity dispersion (GVD). In fact, this is a more serious problem in the visible then at Ti:Saphire wavelengths ($\sim 800nm$) since the dispersion of normal materials increase rapidly as the wavelength gets close to the UV. Secondly, broadband pulse also suffer from group velocity mismatch (GVM) in the nonlinear crystal, requiring the use of extremely thin crystals. The third reason is, second harmonic of these pulses (generated to measure them) falls in the UV, where the response of most detectors drop significantly. Single-shot FROG, for example, requires a CCD, and silicon based CCDs respond poorly in the UV. Even though UV enhanced CCDs are available, their responses are so nonlinear that, over the pulse spectrum (as large as 100 nm), this causes a significant weighting.

Favorably, the GVD and geometrical smearing issues associated with the broad bandwidth, or short pulse width in the visible are analogous to the same issues encountered in Ti:Saphire wavelengths. Therefore, we can adopt the same strategy that we used in chapter 6, where solutions were presented to measure extremely short pulses at $\sim 800nm$. Namely, an all reflective design, with a small crossing angle eliminates both GVD and geometrical smearing effect. Moreover, angle dithering the nonlinear crystal relaxes the GVM constraint, letting us use a much thicker nonlinear crystal [64]. In this case, the crystal thickness is limited by the GVD and for our purposes, we can use $100\mu m$ thick BBO, without causing any significant GVD in the input pulse. Being able to use a thicker crystal is even more

advantageous in the visible, since the low CCD response decreases the sensitivity, and more nonlinear signal from the thicker crystal can compensate for this.

Therefore, provided that the crystal cut angle is adjusted for the visible, the extremely short pulse measurement setup as demonstrated in chapter 6 can be used in visible, as well. However, the characteristics of several elements in the device are strongly wavelength dependent. This causes significant weighting problems, especially for pulses that cover $\sim 100nm$ spectra. These elements include the diffraction grating in the spectrometer (the grating efficiency depends on the wavelength), the lenses, and most importantly, the CCD. All of these elements reflect, transmit or respond poorly for shorter wavelengths. Worse, the actual response functions are very complicated, far beyond linear. As a result, at the output, the spectrum of the second harmonic will be severely distorted. The FROG algorithm will retrieve results based on this distorted trace, which will be incorrect.

To solve this problem, we took the approach of experimentally calculating the spectral response of the elements in the spectrometer stage (including the CCD) of the FROG device. In order to do that, we used a blackbody radiation source (Oriel QTH), which emits continuous blackbody radiation in a very broad range, spanning from UV to IR. Since the theory of blakbody radiation is very well established, the spectrum of the source can be precalculated very accurately and.

We measured the blackbody spectrum using the isolated spectrometer stage of the FROG device. We placed a narrow slit at the position where the nonlinear crystal would normally be. We placed the blackbody lamp far away ($\sim 40cm$) away from the slit. Then we detected the spectrum with the CCD. The spectrum that we measure is, of course, significantly different than the precalculated one. As a result, comparison of measured and calculated spectra gives us what we call "calibration factor" for each wavelength. This factor, when multiplied with spectra for each delay of FROG traces, corrects for the nonlinear spectral response of the device. The resulting FROG traces can then be used in the FROG retrieval algorithm. In order to use this method of spectral correction, we also need to know the exact wavelength that each unit corresponds in the CCD. To do that, we used standard spectral lamp calibration. Particularly, we used Hg lamp, since Hg has

strong atomic transition lines for very short wavelengths. Figure 51 shows the experimental calibration factor that we obtained using Oriel QTH blackbody lamp.

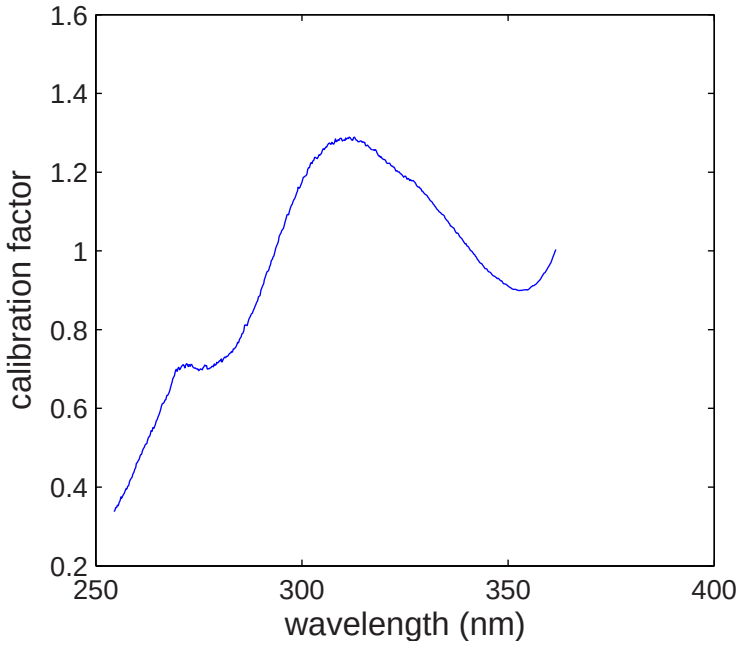

Figure 51: Calibration of the spectral response of the spectrometer stage. We have a nominal center wavelength of $300 - nm$ for the device, therefore the calibration factor at that wavelength is 1

9.3 Experiment

The FROG setup that we used for testing is very similar to the one demonstrated in chapter 6, section 1, with the adjustment of crystal cut angle and spectral response calibration of the spectrometer stage. In order to test the FROG device in the visible, we used an OPA system by Light Conversion (TOPAS white), which can be tuned throughout the visible, with pulse width as short as $10fs$. The repetition rate of the laser was $1 - kHz$ and the average power was $\sim 20mW$ (average power varies depending on the center wavelength).

We acquired several sets of data. We fist measured relatively narrowband ($10nm$) pulses, so as not to require spectral response correction. The center wavelength was tuned to $630 - nm$ Figure 52 shows FROG measurement of these pulses. The measured and retrieved traces match very nicely, as well as independently measured and FROG retrieved spectra.

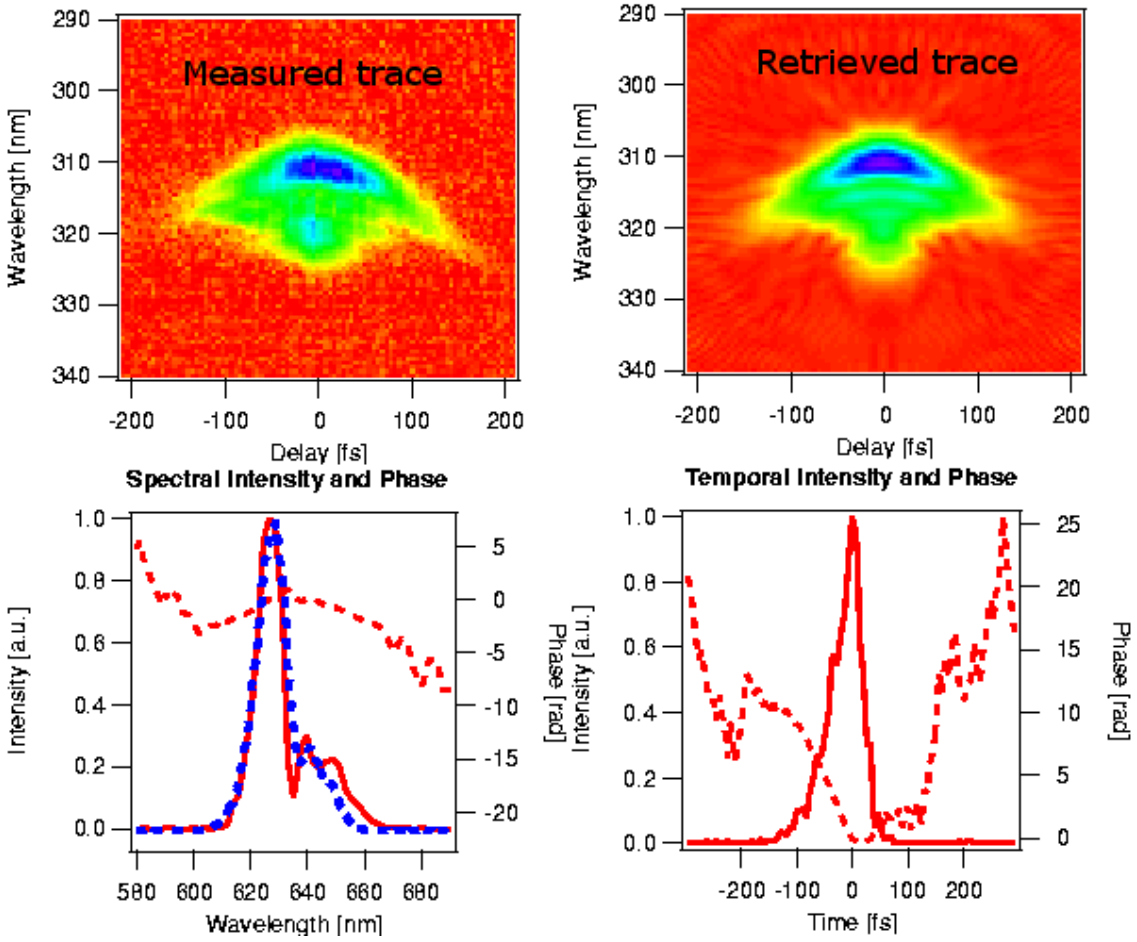

Figure 52: Testing FROG in the visible with $10-nm$ input pulse bandwidth. In the spectral intensity and phase plot, red curve is FROG retrieved and blue curve is independently measured spectra. The temporal pulse width is $60-fs$ FWHM.

To test the effect of nonlinear spectral response of the device elements, we tuned the laser to a much higher bandwidth, so that the pulse spectrum cover about $100-nm$ of bandwidth. Figure 53 shows FROG measurements of these broadband pulses (after spectral response correction), with an accurate retrieval (low FROG error).

Figure 54 shows the independently measured spectrum and FROG retrieved spectra with and without spectral response correction. It is clearly seen that, without the correction, the spectrum is narrower, causing a high FROG error, making the answer incorrect.

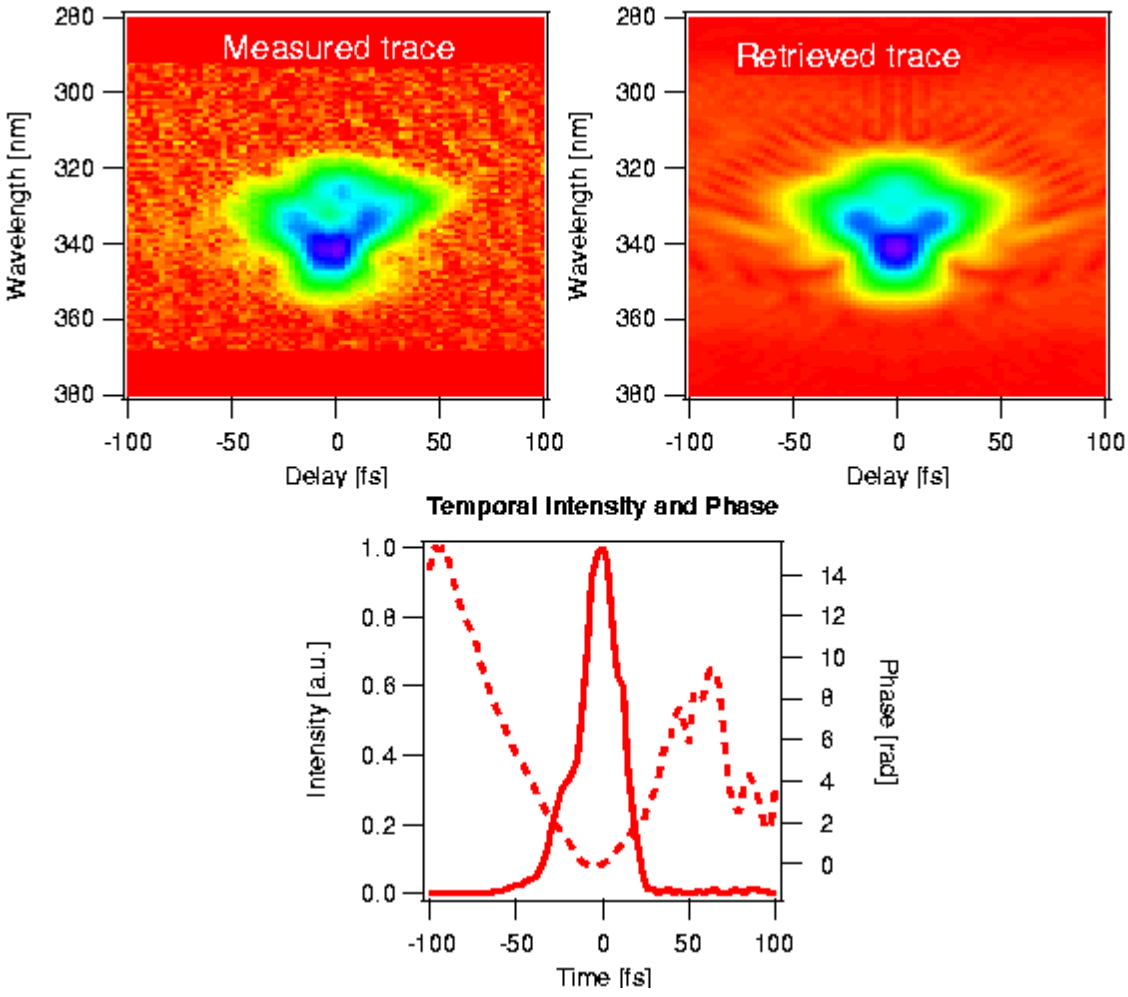

Figure 53: Testing FROG in the visible with $60-nm$ input pulse bandwidth.

In conclusion, we show that, single shot FROG geometry can be extended to measurement of pulses in the visible. In order to do that, we needed to adopt a reflective design to

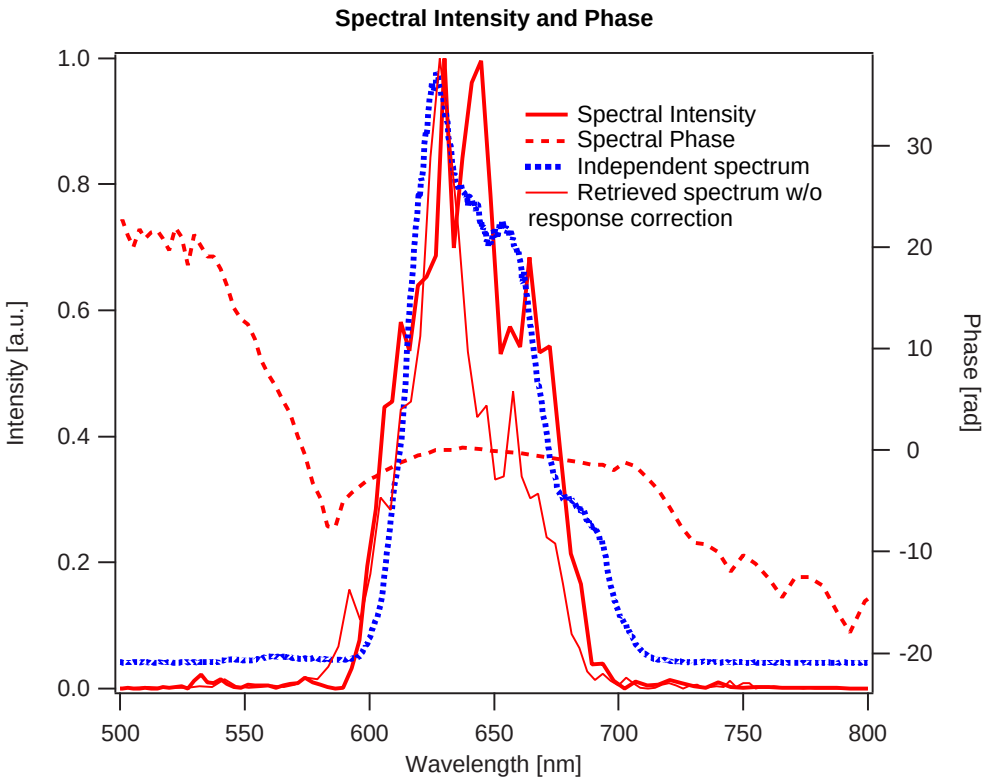

Figure 54: Effect of spectral response correction on retrieved pulse spectrum.

eliminate GVD. We used angle dithering to relax GVM constraint in the nonlinear crystal. We also needed to measure the spectral response of the device and correct the measured traces accordingly. Our experimental results match the expectations very well.

CHAPTER X

CONCLUSIONS AND FUTURE DIRECTIONS

In this thesis work, I proposed and demonstrated solutions to several problems encountered in Ultrafats Optics. These solutions shed light onto previously vague arguments in the field. Additionally, the work that I presented in this thesis also opens up new subjects of interest that can be, will be or is being studied by several other researchers.

The fist part (Chapters 2, 3 and 4) of this thesis was concentrated on the subject of spatio-temporal couplings in ultrashort pulses. As explained in detail in those chapters, theses couplings used to be very much "overseen" by the researchers in the past years. This was mostly because of lack of available tools to monitor them. With ever-continuing improvements in the pulse generation field, it is becoming more and more common and easier to get very short and very broadband pulses. This broadband nature makes it almost impossible to disregard spatio-temporal effects. This fact is causing and increasing number of researchers, to focus more attention on these effects. This thesis showed some of the fruits of this attention. We clarified some previously vague and even misinterpreted thoughts about ultrashort pulses. Furthermore, we developed convenient measurement techniques for them. And in this chapter, dedicated to "conclusions and future directions", I will talk about my projection on more fruits of these efforts that are likely to be collected in the near future.

The assumption that the electric field of the pulse evolves independent of spatial coordinates in time or in frequency, fails with the presence of spatio-temporal distortions. We presented pulse model and measurement techniques for for the most common ones of these distortions, namely spatial chirp, angular dispersion and pulse front tilt. Our findings shows how severe these distortions can be. This makes us believe that, the dependence of pulse's electric field on spatial coordinates deserves a much greater attention. A method that can fully characterize a pulse in four dimensions (time and three space coordinates)

would be ideal. Gabolde et.al. already launched their research in this direction [28], where they propose holographic methods to fully characterize a pulse. Their results looks very promising and enlightening for the future of field of pulse measurements [29].

The measurement techniques that we used are Frequency Resolved Optical Gating (FROG) and its relatives (especially GRENOUILLE). We saw that GRENOUILLE measures an ultrashort pulses full intensity and phase as a function of time (or frequency). Thanks to recent improvements in the FROG algorithm, GRENOUILLE can retrieve the pulse field in "real time", essentially becoming an "ultrafast oscilloscope". The current retrieval code, however, still only concentrates on the temporal behavior, and only reveals, or corrects for spatio-temporal distortions, spatial chirp and pulse-front tilt. Therefore, the retrieved result is only a "best estimate" for what the pulse would be without these distortions. A more informative approach in this direction would be to get an answer with the spatio-temporal distortions, which shows the space-time couplings explicitly.

This requires incorporating these distortions into the core of the FROG algorithm, so that it solves not only for pulse intensity and phase as a function of time or frequency, but also for spatio-temporal distortions. This will result in a retrieval that tells to the user of the device a lot more about the pulse than before. More importantly, this additional information will also be very useful in getting more effective use of ultrashort laser pulses. Some research in this regard has already started. Wang et.al. designed a new algorithm that takes spatio-temporal distortions into account [93, 92], and their algorithm worked very nicely on theory generated pulses. The test of the algorithm on experimental pulses, pulses with more complexity and speeding the new algorithm are upcoming developments. Figure 55 shows one of the very promising results that Wang et.al. demonstrated with their new FROG pulse retrieval algorithm. They started with a (theoretical) pulse with a fairly complicated temporal structure. They then added spatial chirp to this pulse, obtaining a distorted GRENOUILLE trace. In the end, they ran their new retrieval algorithm on this distorted trace. As a result, the retrieved trace matched perfectly with the original (distorted) trace. The retrieved value of spatial chirp (which the new algorithm gives) also matched perfectly with the input value.

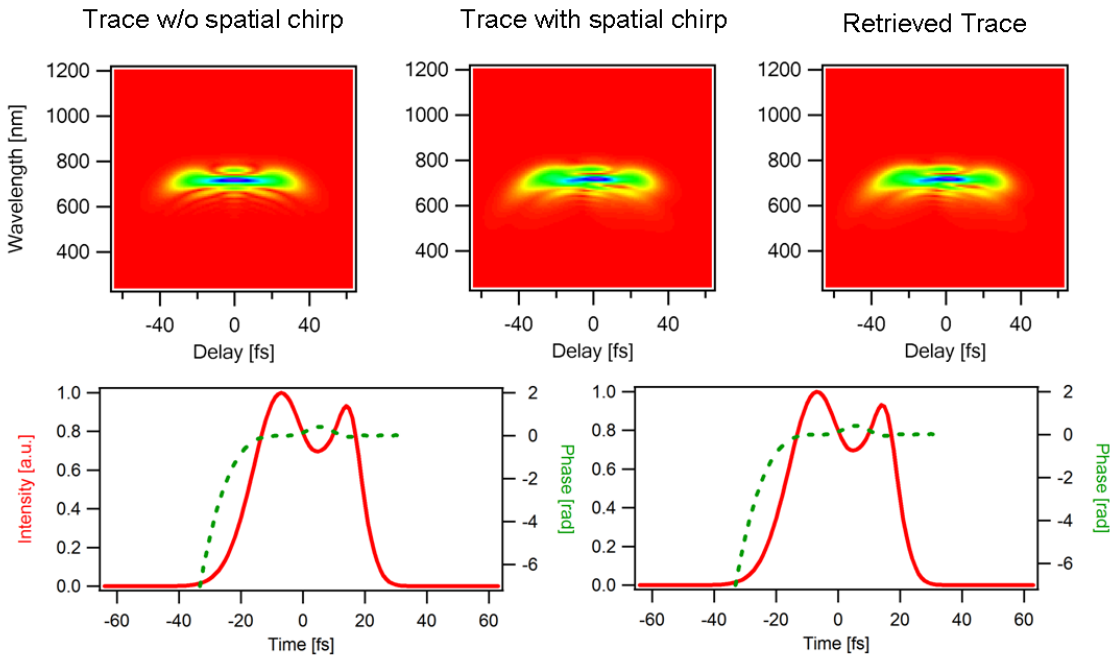

Figure 55: A test of FROG algorithm that retrieves spatio-temporal distortions.

These researches and several others on pulse characterization methods extended to spatial coordinates continuously improve our knowledge about ultrashort pulses, and allows us to not only better understand the physics behind these pulse but also to make a much effective use of them.

In chapters 5 and 6, I worked on extending pulse measurement techniques to extremely short and extremely long pulses. On the extremely short pulse measurement side, we first improved GRENOUILLE to work at its short pulse-limits, which was shown to be $\sim 20-fs$ at $800-nm$. We then demonstrated convenient methods for measuring pulses that are as short as $10fs$. A $10fs$ pulse is already phenomenal as it contains only about 4 optical cycles. However, as we researchers always ask for more, the efforts on getting shorter and shorter pulses is never ending. In fact, there has been recently a demonstration of a "single cycle optical pulse" first time in the history [90]. Unfortunately, while the demonstration is impressive to all ultrashort scientists, and it is widely accepted that they had the tool to generate such a pulse, the measurement method was controversial, especially since there was no proof of its uniqueness. This and several other high profile works on (almost) single cycle

pulse generation would certainly benefit extensively form a convenient pulse measurement technique, especially if it can give "unique" answers. This is one obvious next step that can/will be taken in the near future of ultrashort pulse measurement.

Another cutting edge development in the field of ultrashort pulse phenomena is generation of attosecond pulses in the [16, 38]. These pulses are generated by focusing high power, near-single-cycle optical pulses to a gas jet. The method utilizes the coherent properties of the high harmonics produced in the interaction of laser light with the gas atoms. Provided that they are well characterized, they can be very useful in time gating phenomena occurring in attosecond time scale. Consequently, attosecond pulses are of great interest to a variety of scientific areas including solid state and plasma physics and material science. The challenging problem is to find a measurement technique that characterize such short pulse. The challenge arises from the fact that, in contrast to femtosecond pulses, the attosecond pulses are necessarily in the UV-XUV spectral range, they are orders of magnitude weaker and spectrally much broader. Optical elements required in pulse measurements, including nonlinear media, are not readily available at those extreme wavelengths, where even beam splitting optics is non-trivial. Therefore, the field of attosecond pulse generation opens up broad research areas. And these research areas will benefit extensively from pushing pulse measurement techniques to these pulse lengths and frequencies.

Measurement of ultrashort pulses will always help promote the generation and application of ultrafast phenomena. And it is the nature of research to always bring up new unsolved problems. In this document, I presented solutions to several previously unsolved problems and questions in ultrashort pulse measurement. I anticipate that our answers to these questions will stand as a base for new researches to solve further problems.

REFERENCES

[1] Agrawal, G., *Nonlinear Fiber Optics*. Boston: Academic Press, 1995.

[2] Akturk, S., Gu, X., Zeek, E., and Trebino, R., "Pulse-front tilt caused by spatial and temporal chirp," *Optics Express*, vol. 12, no. 19, pp. 4399–4410, 2004.

[3] Akturk, S., Kimmel, M., O'Shea, P., Tebino, R., Naumov, S., Sorokin, E., and Sorokina, I., "Measuring several-cycle 1.5-m pulses using frequency-resolved optical gating," *Optics Express*, vol. 11, no. 25, pp. 3461–3466, 2003.

[4] Akturk, S., Kimmel, M., O'Shea, P., and Trebino, R., "Measuring pulse-front tilt in ultrashort pulses using grenouille," *Optics Express*, vol. 11, pp. 491–501, 2003.

[5] Akturk, S., Kimmel, M., O'Shea, P., and Trebino, R., "Measuring spatial chirp in ultrashort pulses using single-shot frequency-resolved optical gating," *Optics Express*, vol. 11, pp. 68–78, 2003.

[6] Akturk, S., Kimmel, M., O'Shea, P., and Trebino, R., "Extremely simple device for measuring 20 fs pulses," *Optics Letters*, vol. 29, no. 9, pp. 1025–1027, 2004.

[7] Akturk, S., Kimmel, M., and Trebino, R., "Extremely simple device for measuring 1.5-m ultrashort laser pulses," *Optics Express*, vol. 12, no. 19, pp. 4483–4489, 2004.

[8] Baltuska, A., Pshenichnikov, M., and Wiersma, D., "Amplitude and phase characterization of 4.5 fs pulses by frequency-resolved optical gating," *Optics Letters*, vol. 23, no. 18, pp. 1474–6, 1998.

[9] Baltuska, A., Pshenichnikov, M., and Wiersma, D., "Second-harmonic generation frequency-resolved optical gating in the single-cycle regime," *IEEE J. Quant. Electron.*, vol. 35, no. 4, pp. 459–478, 1999.

[10] Bor, Z. and Racz, B., "Group velocity dispersion in prisms and its application to pulse compression and travelling-wave excitation," *OC*, vol. 54, no. 3, pp. 165–170, 1985.

[11] Bor, Z., Racz, B., Szabo, G., Hilbert, M., and Hazim, H., "Femtosecond pulse front tilt caused by angular dispersion," *Opt. Engineering*, vol. 32, no. 10, pp. 2501–2503, 1993.

[12] Born, M. and Wolf, E., *Principles of Optics: Electromagnetic Theory of Propagation, Interference and Diffraction of Light*. Cambridge Univ Pr, 1999.

[13] Boyd, R., *Nonlinear Optics*. Academic Press, 2003.

[14] Cerullo, G., Nisoli, M., Stagira, S., and De Silvestri, S., "Sub-8-fs pulses from an ultrabroadband optical parametric amplifier in the visible," *Optics Letters*, vol. 23, no. 16, pp. 1283–1285, 1998.

[15] Christov, I., Michailov, N., and Danailov, M., "Mode locking with spatial dispersion in the gain medium," *Applied Physics B-Lasers and Optics*, vol. B53, no. 2, pp. 115–118, 1991.

[16] Christov, I., Murnane, M., and Kapteyn, H., "High-harmonic generation of attosecond pulses in the "single-cycle" regime," *Physical Review Letters*, vol. 78, no. 7, pp. 1251–1254, 1997.

[17] DeLong, K., Fittinghoff, D., and Trebino, R., "Practical issues in ultrashort-laser-pulse measurement using frequency-resolved optical gating," *IEEE J. Quant. Electron.*, vol. 32, no. 7, pp. 1253–1264, 1996.

[18] DeLong, K., Fittinghoff, D., Trebino, R., Sullivan, A., Hunter, J., White, W., and Kane, D., "Frequency-resolved optical gating: Measuring the intensity and phase of an ultrashort laser pulse," in *Ultrafast Phenomena IX* (Barbara, P., Knox, W., Mourou, G., and Zewail, A., eds.), Springer Series in Chemical Physics, pp. 127–131, Berlin: Springer-Verlag, 1994.

[19] DeLong, K. and Trebino, R., "Improved ultrashort pulse-retrieval algorithm for frequency-resolved optical gating," *J. Opt. Soc. Am. A*, vol. 11, no. 9, pp. 2429–2437, 1994.

[20] DeLong, K. and Trebino, R., "Measuring the intensity and phase of two ultrashort pulses on a single shot," in *Generation, Amplification, and Measurement of Ultrashort Laser Pulses* (Trebino, R. and Walmsley, I., eds.), vol. 2116, pp. 268–274, Bellingham, WA: Society of Photo-Optical Instrumentation Engineers, 1994.

[21] DeLong, K., Trebino, R., Hunter, J., and White, W., "Frequency-resolved optical gating with the use of second-harmonic generation," *J. Opt. Soc. Amer. B*, vol. 11, no. 11, pp. 2206–2215, 1994.

[22] Diels, J. and Rudolph, W., *Ultrashort Laser Pulse Phenomena*. San Diego: Academic Press, 1996.

[23] Dmitriyev, V., Gurzadian, G., and NikogosianD.N., *Handbook of Nonlinear Optical Crystals*. Springer Verlag, 1999.

[24] Dorrer, C., Kosik, E., and Walmsley, I. A., "Direct space-time characterization of the electric fields of ultrashort optical pulses," *Optics Letters*, vol. 27, no. 7, pp. 548–550, 2002.

[25] Dorrer, C., Kosik, E., and Walmsley, I. A., "Spatio-temporal characterization of ultrashort optical pulses using two-dimensional shearing interferometry," *Applied Physics B-Lasers and Optics*, vol. 74 [suppl.], pp. 209–219, 2002.

[26] Efimov, A., Schaffer, C., and Reitze, D., "Programmable shaping of ultrabroad-bandwidth pulses from a ti:sapphire laser," *J. Opt. Soc. Am. B*, vol. 12, no. 10, pp. 1968–1980, 1995.

[27] Fork, R., Martinez, O., and Gordon, J., "Negative dispersion using pair of prisms," *Optics Letters*, vol. 9, no. 5, pp. 150–152, 1984.

[28] Gabolde, P., Akturk, S., and Trebino, R., "Self-referenced measurement of the complete electric field of ultrashort pulses in time and space," in *Ultrafast Phenomena*, (Niigata, Japan), 2004.

[29] Gabolde, P. and Trebino, R., "Self-referenced measurement of the complete electric field of ultrashort pulses," *Optics Express*, vol. 12, no. 19, pp. 4423–4429, 2004.

[30] Gallmann, L., Steinmeyter, G., Sutter, D., Rupp, T., Iaconis, C., Walmsley, I. A., and Keller, U., "Spatially resolved amplitude and phase characterization of femtosecond optical pulses," *Optics Letters*, vol. 26, no. 2, pp. 96–98, 2001.

[31] Gordon, J. and Fork, R., "Optical resonator with negative dispersion," *Optics Letters*, vol. 9, no. 5, pp. 153–155, 1984.

[32] Gu, X., *Measuring Ultracomplex Supercontinuum Pulses and Spatio-Temporal Distortions*. PhD thesis, Georgia Institute of Technology, 2004.

[33] Gu, X., Akturk, S., and Trebino, R., "Spatial chirp in ultrafast optics," *Opt. Comm.*, vol. 242, pp. 599–604, 2004.

[34] Gu, X., Kimmel, M., Zeek, E., Shreenath, A., and Trebino, R., "Single-shot spectral measurements of the ultrabroadband continuum from microstructure fiber," in *OSA Annual Meeting*, (Orlando, Florida), 2002.

[35] Gu, X., Xu, L., Kimmel, M., Zeek, E., O'Shea, P., Shreenath, A. P., Trebino, R., and Windeler, R. S., "Frequency-resolved optical gating and single-shot spectral measurements reveal fine structure in microstructure-fiber continuum," *Optics Letters*, vol. 27, no. 13, pp. 1174–1176, 2002.

[36] Hebling, J., "Derivation of pulse-front tilt casued by angular dispersion," *Optical and Quantum Engineering*, vol. 28, pp. 1759–1763, 1996.

[37] Hecht, E., *Optics*. Addison Wesley Longman, Inc, 3 ed., 1998.

[38] Hentschel, M., Keinberger, R., Speilmann, C., Reider, G., Milosevic, N., Brabec, T., Corkum, P., Heinzmann, U., Drescher, M., and Krausz, F., "Attosecond metrology," *Nature*, vol. 414, pp. 509–513, 2001.

[39] Heritage, J., Weiner, A., and Thurston, R., "Picosecond pulse shaping by spectral phase and amplitude manipulation," *Optics Letters*, vol. 10, no. 12, pp. 609–611, 1985.

[40] Iaconis, C. and Walmsley, I., "Self-referencing spectral interferometry for measuring ultrashort optical pulses," *IEEE J. Quant. Electron.*, vol. 35, no. 4, pp. 501–509, 1999.

[41] Kane, D., "Real-time measurement of ultrashort laser pulses using principal-components generalized projections," *J. Special Topics Quant. Electron.*, vol. 4, no. 2, pp. 278–284, 1998.

[42] Kane, D. and Trebino, R., "Characterization of arbitrary femtosecond pulses using frequency resolved optical gating," *IEEE J. Quant. Electron.*, vol. 29, no. 2, pp. 571–579, 1993.

[43] Kane, D. and Trebino, R., "Single-shot measurement of the intensity and phase of an arbitrary ultrashort pulse by using frequency-resolved optical gating," *Optics Letters*, vol. 18, no. 10, pp. 823–825, 1993.

[44] Klebniczki, J., Bor, Z., and Szabo, G., "Theory of travelling wave amplified spontaneous emission," *Applied Physics B-Lasers and Optics*, vol. 46, pp. 151–155, 1988.

[45] Kohler, B., Yakovlev, V., Wilson, K., Squier, J., DeLong, K., and Trebino, R., "Phase and intensity characterization of femtosecond pulses from a chirped-pulse amplifier by frequency-resolved optical gating," *Optics Letters*, vol. 20, no. 5, pp. 483–485, 1995.

[46] Kostenbauder, A., "Ray-pulse matrices: A rational treatment for dispersive optical systems," *IEEE J. Quant. Electron.*, vol. 26, no. 6, pp. 1148–1157, 1990.

[47] Kovacs, A., Varju, K., Kurdi, G., Osvay, K., Heiner, Z., Klebniczki, J., and Csatari, M., "Experimental investigation of angular dispersion in ultrashort pulses having gaussian spatial profile," in *Ultrafast Optics IV*, (Vienna, Austria), 2003.

[48] Kozma, I., Almasi, G., and Hebling, J., "Geometrical optical modeling of femtosecond setups having angular dispersion," *Applied Physics B-Lasers and Optics*, vol. B76, no. 3, pp. 257–261, 2003.

[49] Lacourt, P., Dudley, J., Merolla, J., Porte, H., Goedgebuer, J., and Rhodes, W., "Milliwatt-peak-power pulse characterization at 1.55 m by wavelength conversion frequency-resolved optical gating," *Optics Letters*, vol. 27, pp. 863–865, 2002.

[50] Lin, Q. and Sorokina, I., "High-order dispersion effects in solitary mode-locked lasers: side-band generation," *Opt. Comm.*, vol. 153, pp. 285–288, 1998.

[51] Maier, M. and Kaiser, W., "Intense light bursts in the stimulated raman effect," *Physical Review Letters*, vol. 17, no. 26, pp. 1275–1277, 1966.

[52] Mair, R., Lin, J., Jiang, H., Jones, E., Allerman, A., and Kurtz, S., "Time-resolved photoluminescence studies of inxga1?xas1?yny," *Applied Physics Letters*, vol. 76, no. 2, pp. 188–190, 2000.

[53] Martinez, O., "Grating and prism compressors in the case of finite beam size," *J. Opt. Soc. Am. B*, vol. 3, no. 7, pp. 929–934, 1986.

[54] Martinez, O., "Pulse distortions in tilted pulse schemes for ultrashort pulses," *Opt. Comm.*, vol. 59, no. 3, pp. 229–232, 1986.

[55] Martinez, O., "Matrix formalism for pulse compressors," *IEEE J. Quant. Electron.*, vol. 24, no. 12, pp. 2530–2536, 1988.

[56] Martinez, O., "Matrix formalism for dispersive laser cavities," *IEEE J. Quant. Electron.*, vol. 25, pp. 296–300, 1989.

[57] Martinez, O., Gordon, J., and Fork, R., "Negative group-velocity dispersion using refraction," *J. Opt. Soc. Am. B*, vol. 1, no. 10, pp. 1003–1006, 1984.

[58] Michailov, N., "Passively mode-locked dye laser with spatial dispersion in the gain medium," *J. Opt. Soc. Am. B*, vol. 9, no. 8, pp. 1369–1373, 1991.

[59] Naumov, S., Sorokin, E., Kalashnikov, V., Tempea, G., and Sorokina, I., "Directly diode-pumped femtosecond cr4+:yag laser," in *Advanced Solid-State Photonics*, vol. 68, pp. 144–146, OSA TOPS, 2003.

[60] Naumov, S., Sorokin, E., Kalashnikov, V., Tempea, G., and Sorokina, I., "Self-starting five optical cycle pulse generation in cr4+:yag laser," *Applied Physics B-Lasers and Optics*, vol. 76, pp. 1–11, 2003.

[61] Nelson, L., Jones, D., Tamura, K., Haus, H., and Ippen, E., "Ultrashort-pulse fiber ring lasers," *Applied Physics B-Lasers and Optics*, vol. 65, pp. 277–294, 1997.

[62] Ohmae, G., Yagi, T., Nanri, K., and Fujioka, T., "Spatial spectrum chirp characteristic of a martinez-type multipass pulse stretcher," *Jpn. J. Appl. Phys.*, vol. 39, pp. 5864–5869, 2000.

[63] O'Shea, P., Akturk, S., Kimmel, M., and Trebino, R., "Practical issues in ultrashot-pulse measurements with 'grenouille'," *Applied Physics B-Lasers and Optics*, vol. 79, pp. 683–691, 2004.

[64] O'Shea, P., Gu, X., Kimmel, M., and Trebino, R., "Increased bandwidth in ultrashort-pulse measurement using an angle-dithered nonlinear-optical crystal," *Optics Express*, vol. 7, no. 10, pp. 342–349, 2001.

[65] O'Shea, P., Kimmel, M., Gu, X., and Trebino, R., "Highly simplified device for ultrashort-pulse measurement," *Optics Letters*, vol. 26, no. 12, pp. 932–934, 2001. English Article OPTICS LETTERS.

[66] O'Shea, P., Kimmel, M., and Trebino, R., "Increased phase-matching bandwidth in simple ultrashort-laser- pulse measurements," *Journal of Optics B-Quantum and Semiclassical Optics*, vol. 4, no. 1, pp. 44–48, 2002.

[67] Paye, J. and Migus, A., "Space-time wigner functions and their application to the analysis of a pulse shaper," *J. Opt. Soc. Am. B*, vol. 12, no. 8, pp. 1480–1490, 1995.

[68] Pessot, M., Squier, J., Mourou, G., and Harter, D., "Chirped-pulse amplification of 100-fsec pulses," *Optics Letters*, vol. 14, no. 15, pp. 797–799, 1989.

[69] Prade, B., Schins, J., Nibbering, E., Franco, M., and Mysyrowickz, A., "A simple method for the determination of the intensity and phase of ultrashort optical pulses," *Opt. Comm.*, vol. 113, no. 1, pp. 79–84, 1995. Using SPM, two spectra, and an iterative algorithm to measure ultrashort pulses.

[70] Raghuramaiah, M., Sharma, A., Naik, P., and Gupta, P., "Simultaneous measurement of pulse-front tilt and pulse duration of a femtosecond laser beam," *Opt. Comm.*, vol. 223, pp. 163–168, 2003.

[71] Richman, B., Krumbgel, M., and Trebino, R., "Temporal characterization of mid-ir free-electron-laser pulses by frequency-resolved optical gating," *Optics Letters*, vol. 22, no. 10, pp. 721–723, 1997.

[72] Ripin, D., Chudoba, C., Gopinath, J., Fujimoto, J., Ippen, E., Morgner, U., Kartner, F., Scheuer, V., Angelov, G., and Tschudi, T., "Generation of 20-fs pulses by a prismless cr4+:yag laser," *Optics Letters*, vol. 27, pp. 61–61, 2002.

[73] Ripin, D., Gopinath, J., Shen, H., Erchak, A., Petrich, G., Kolodziejski, L., Kartner, F., and Ippen, E., "Oxidized gaas/alas mirror with a quantum-well saturable absorber for ultrashort-pulse cr4+:yag laser," *Opt. Comm.*, vol. 214, p. 285, 2002.

[74] Rulliere, C., ed., *Femtosecond Laser Pulses: Principles and Experiments*. Heidelberg: Springer, 1998.

[75] Sacks, Z., Mourou, G., and Danielius, R., "Adjusting pulse-front tilt and pulse duration by use of a single-shot autocorrelator," *Optics Letters*, vol. 26, pp. 462–464, 2001.

[76] Saleh, B. and Teich, M., *Fundamentals of Photonics*. John Wiley and Sons Inc, 1991.

[77] Seas, A., Petricevic, V., and Alfano, R., "Generation of sub-100-fs pulses from a cw mode-locked chromium-doped forsterite laser," *Optics Letters*, vol. 17, no. 13, pp. 937–939, 1992.

[78] Siegman, A., *Lasers*. Univ Science Books, 1986.

[79] Smith, A., "Group-velocity-matched three-wave mixing in birefringent crystals," *Optics Letters*, vol. 26, no. 10, pp. 719–721, 2001.

[80] Smith, M., Chen, G., Lin, J., Jiang, H., Khan, M., and Chen, Q., "Time-resolved photoluminescence studies of ingan epilayers," *Applied Physics Letters*, vol. 69, no. 19, pp. 2837–2839, 1996.

[81] Stingl, A., Lenzner, M., Speilmann, C., Krausz, F., and Szipocs, R., "Sub-10-fs mirror-dispersion-controlled ti:sapphire laser," *Optics Letters*, vol. 20, pp. 602–604, 1995.

[82] Szatmari, S., Kunhle, G., and Simon, P., "Pulse compression and traveling wave excitation scheme usind a single dispersive element," *Applied Optics*, vol. 29, no. 36, pp. 5372–5379, 1990.

[83] Tan, H., Warren, W., and Schreiber, E., "Generation and amplification of ultrashort shaped pulses in the visible by a two-stage noncollinear optical parametric process," *Optics Letters*, vol. 26, no. 2, pp. 1812–1814, 2001.

[84] Tanabe, T., Tanabe, H., Teramura, Y., and Kannari, F., "Spatiotemporal measurements based on spatial spectral interferometry for ultrashort optical pulses shaped by a fourier pulse shaper," *J. Opt. Soc. Am. B*, vol. 19, no. 11, pp. 2795–2802, 2002.

[85] Thurston, R., Heritage, J., Weiner, A., and Tomlinson, W., "Analysis of picosecond pulse shape synthesis by spectral masking in a grating pulse compressor," *IEEE J. Quant. Electron.*, vol. 22, no. 5, pp. 682–696, 1986.

[86] Trebino, R., DeLong, K., Fittinghoff, D., Sweetser, J., Bowie, J., and Krumbgel, M., "Practical advances in ultrashort pulse measurement using frequency-resolved optical gating," in *Generation, Amplification, and Measurement of Ultrashort Laser Pulses III* (White, W. and Reitze, D., eds.), Bellingham: Society of Photo-Optical Instrumentation Engineers, 1996.

[87] Trebino, R., *Frequency-Resolved Optical Gating*. Boston: Kluwer Academic Publishers, 2002.

[88] Varju, K., Kovacs, A., Kurdi, G., and Osvay, K., "High-precision measurement of angular dispersion in a cpa laser," *Applied Physics B-Lasers and Optics*, vol. B74[Suppl], pp. 259–263, 2002.

[89] Varju, K., Kovacs, A., and Osvay, K., "Angular dispersion of femtosecond pulses in a gaussian beam," *Optics Letters*, vol. 27, no. 22, pp. 2034–2036, 2002.

[90] Walker, D., Shverdin, M., Yavuz, D., Yin, G., and Harris, S., "Generation of a single-cycle optical pulse," in *Ultrafast Phenomena*, (Niigata, Japan), Springer, 2004.

[91] Walmsley, I. A. and Wong, V., "Characterization of the electrical field of ultrashort optical pulses," *J. Opt. Soc. Am. B*, vol. 13, no. 11, pp. 2453–2463, 1996. Ian's definitive theory of pulse-measurement techniques. In this analysis, FROG is the best-known variant of a Type I (amplitude time-nonstationary–amplitude stationary) device.

[92] Wang, Z., *Next Generation Ultrashort-Pulse Retrieval Algorithm for Frequency-Resolved Optical Gating*. PhD thesis, Georgia Institute of Technology, 2005.

[93] Wang, Z., Gu, X., Akturk, S., and Trebino, R., "Retrieving spatio-temporal distortions in ultrashort pulses from frog traces," *(To be published)*.

[94] Wang, Z., Zeek, E., Kvam, P., and Trebino, R., "Determining error bars in measurements of ultrashort laser pulses," *J. Opt. Soc. Am. B*, vol. 20, no. 11, pp. 2400–2405, 2003.

[95] Weber, H., "Generation and measurement of ultrashort light pulses," *Journal of Applied Physics*, vol. 39, no. 13, pp. 6041–6044, 1968.

[96] Wefers, M. and Nelson, K., "Analysis of programmable ultrashort waveform generation using liquid-crystal spatial light modulators," *J. Opt. Soc. Am. B*, vol. 12, no. 7, pp. 1343–1362, 1995.

[97] Wefers, M. and Nelson, K., "Space-time profiles of shaped ultrafast optical waveforms," *IEEE J. Quant. Electron.*, vol. 32, no. 1, pp. 162–172, 1996.

[98] Weiner, A., Heritage, J., and Kirschner, E., "High-resolution femtosecond pulse shaping," *J. Opt. Soc. Am. B*, vol. 5, no. 8, pp. 1563–1572, 1988.

[99] Wu, Q. and Zhang, X., "Free-space electro-optics sampling of mid-infrared pulses," *Applied Physics Letters*, vol. 71, no. 10, pp. 1285–1286, 1997.

[100] Zeek, E., Shreenath, A. P., O'Shea, P., Kimmel, M., and Trebino, R., "Simultaneous automatic calibration and direction-of-time removal frequency-resolved optical gating," *Applied Physics B-Lasers and Optics*, vol. 74, pp. S265–S271, 2002.

[101] Zeek, E., Wang, Z., and Trebino, R., "Error bars in frequency-resolved-optical-gating measurements of ultrafast laser pulses," in *LEOS Annual Meeting*, (Glasgow, Scotland), 2002.

VITA

Selçuk Aktürk was born in Trabzon, Turkey, on April 1^{st} 1980. He graduated from Bilkent University, Ankara, Turkey, with a degree of BS in Physics. He is pursuing his PhD studies in the field of Ultrafast Optics, in the research group of Rick Trebino at School of Physics, Georgia Institute of Technology.